2007

Quantum phases in frustrated strongly correlated 2-D systems

Jun Liu
Iowa State University

Quantum phases in frustrated strongly correlated 2-D systems

by

Jun Liu

A dissertation submitted to the graduate faculty

in partial fulfillment of the requirements for the degree of

DOCTOR OF PHILOSOPHY

Major: Condensed Matter Physics

Program of Study Committee:
Jörg Schmalian, Major Professor
Paul Canfield
Vladimir Kogan
Kerry Whisnant
Michael Smiley

Iowa State University

Ames, Iowa

2007

UMI Number: 3274848

UMI Microform 3274848

ProQuest Information and Learning Company
300 North Zeeb Road
P.O. Box 1346
Ann Arbor, MI 48106-1346

...to Uncle Zhaohuan Zeng

TABLE OF CONTENTS

LIST OF FIGURES

ACKNOWLEDGEMENTS

I would like to express my hearty appreciation to Prof. Joerg Schmalian, my Ph.D thesis advisor, for his stimulating and insightful guidance in helping me finish the whole research work. I am inspired very much by his broad knowledge and interests in different physical areas, his humble character, and his excellent skills in communicating with people. I am very grateful to his unlimited patience and tolerance he showed to me during our collaboration for these years. I learned from him not only science, but the way to express myself and behave professionally. I am sure I will benefit my whole life from my experience with him. I would also like to thank my wife, lily, for her full support and bitter sacrifices she has endured during these several years. I am so happy that I have had an understanding, supportive, gentle and delicate wife to be with me. I also would like to thank Prof. Nandini Trivedi for her generous offering of the core code on calculation of energy expectation, ODLRO and low frequency Drude weight. I also would like to acknowledge Ming Li and Sknepnek Rastko for their helpful discussions and timely help, especially Rastko's help on finalizing the thesis draft. Meanwhile, I would like to thank computing facilities from Ames Lab, DOE.

ABSTRACT

The strong Coulomb repulsion between charge carriers in a system with one electron per site can lead to a full localization of the electrons. The resulting state is called a Mott insulating state. The interplay between the physics of Mott insulators and of unconventional superconductors has been a focus in condensed matter physics for a long time. Although it has frequently been argued that the proximity to a Mott insulating phase is responsible for the emergence of unconventional superconductivity, little progress has been made in obtaining a convincing microscopic theory. Due to the strong electron-electron (e-e) interaction involved in Mott insulators, mean field theory is not a reliable tool. Thus other nonperturbative methods, including the Resonating Valence Bond (RVB) variational theory, have been developed. Recently experimental results showing that a spin liquid state, which is a Mott insulator without long range magnetic order, can undergo a pressure induced transition into an unconventional superconducting state has helped to sharpen this question. This experimental observation demonstrates that the onset of unconventional superconductivity doesn't require magnetic ordering. The RVB picture serves perfectly in this context since it starts with a nonmagnetic state. The major goal of this thesis is to investigate the unconventional electronic and magnetic properties of a superconductor close to a Mott insulating phase. Particular emphasis is given to frustrated systems where the role of quantum frustration is known to be strong and where the Mott insulator is not magnetically ordered. Specifically we study models relevant to two frustrated quantum spin systems.

One material of interest is $\kappa - (\mathrm{ET})_2 Cu_2 (CN)_3$, an organic superconductor. Its spin-liquid ground state can be tuned by pressure into an unconventional superconducting state. We propose a new variational wavefunction by introducing nonlocal correlation effects into

the usual partially projected Gutzwiller wavefunction. We successfully find a superconducting state of d-wave pairing symmetry sandwiched between a metallic state and a spin liquid state around some critical onsite repulsion U. We also find strong "Fermi surface" renormalization when superconductivity starts to emerge.

The other material of interest is $SrCu_2\left(BO_3\right)_2$ whose ground state is known to be a singlet dimer state. We derive a multiband BCS wavefunction and apply onto it the full Gutzwiller projection. We show that the obtained trial wavefunction can give the exact ground state energy to the undoped system. We then find that the physical properties are dramatically different for the electron and hole doped cases. We find, for the hole doped case, a plaquette d-wave pairing pattern and enhanced superconductivity due to this pairing inhomogeneity; while for the electron doped case, we find a strange metallic state.

CHAPTER 1. Introduction

Strong electron-electron (e-e) interaction, i.e. the physics of strong correlation among charge carriers, is believed to be responsible for many interesting phenomena shared by a number of different materials. High T_c cuprates (1), organic superconductors (2) and heavy fermion systems (3) are important examples. A Mott insulating phase, unconventional superconductivity, pseudogap behavior, quantum criticality and bad metal behavior are among the properties caused by the strong e-e interaction. The mechanism of unconventional superconductivity has attracted the attention of physicists for a long time. The physics of a Mott transition, from an insulating to a metallic state caused by localization due to strong Coulomb repulsion, is believed to be important for this purpose since unconventional superconductivity and the Mott insulating state appear together in two distinct classes of materials: cuprates and organic superconductors. The role of magnetic fluctuations is especially stressed since magnetic ordering seems to always exist in the Mott insulating phase. But this notion has recently been challenged with the discovery of the organic superconductor $\kappa-(\mathrm{ET})_2\,Cu_2\,(CN)_3$ which can be tuned from a magnetically disordered spin liquid state to an unconventional superconducting state under pressure (4). In this thesis, I would like to investigate how this special Mott transition can be addressed by a Resonating Valence Bond (RVB) picture to be detailed shortly. We will use this formulism to investigate the unconventional electronic and magnetic properties of a superconductor close to a Mott insulating phase. We will put particular emphasis on frustrated systems, where the role of quantum frustration is known to be strong and where the Mott insulator is not magnetically ordered. We then will analyze what this picture implies for another magnetically fully frustrated material, $SrCu_2\,(BO_3)_2$.

1.1 Mott insulator vs. band insulator

Materials that are insulating are rather common in everyday life. The insulating nature of these systems can usually be interpreted as being caused by a fully filled valence band, shown in the panel (a) of Fig. 1.1, so that electronic motion is fully counteracted by its Bragg reflection on the Brillioun zone boundary. Examples are many Si-based systems, diamond, etc. This interpretation is based on the band theory where electrons are assumed not to interact or if only weakly between each other so that the movement of one electron hardly affects other electrons (5). Such behavior is called band insulating.

A band insulator is not the only possible explanation on how an insulator can be formed. One possibility is the localization of electrons in disordered systems. However, there are also non-disordered clean materials whose valence electrons only half fill an energy band yet they are insulating. This is contradictory to what the band theory predicts and thus implies that the e-e interaction comes into play. The insulating behavior caused by this interaction is called Mott insulating (6).

In a Mott insulator, an energy band is split into two subbands due to the strong e-e interaction. How large the separation in energy is depends on how strengthy the e-e interaction is between two electrons staying in the same site. The subbands distinguish themselves from the usual band in the way how each momentum state, $\mathbf{k}$, is occupied. In the usual band each $\mathbf{k}$ contains a maximum of two electrons of opposite spins, but in a subband only one electron is allowed. When the material becomes a Mott insulator, the lower subband becomes fully filled. This is shown in panel (b) of Fig. 1.1.

The distinction between a band and a Mott insulator can also be clearly illustrated in real space pictures. For a band insulator, a fully filled band is equivalent to a fully filled lattice in real space, where each site contains two electrons with opposite spins. This is illustrated in panel (c). A half-filled band corresponds to a real space picture with electrons randomly sitting on each lattice site. When the e-e interaction becomes strong, electrons repel each other to reduce their mutual onsite-repulsion and only a single electron is allowed on each site. The Mott insulator then corresponds to a lattice with each site singly occupied, as shown in the

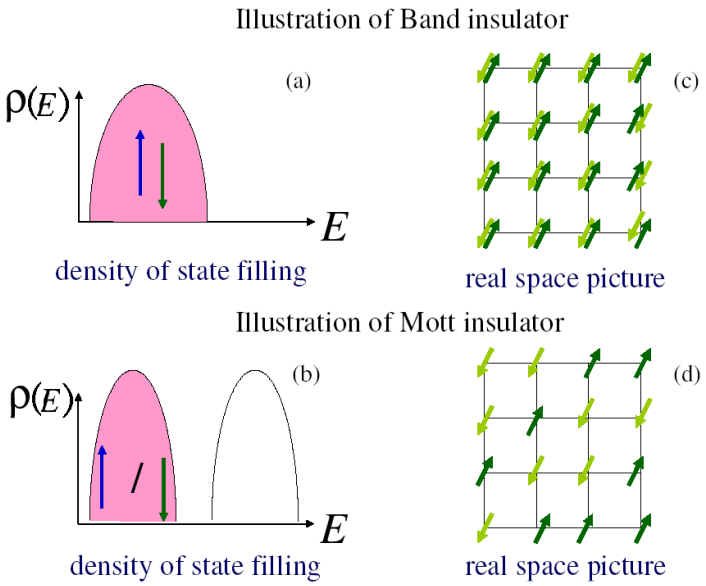

Figure 1.1 Illustration of both a band insulator and a Mott insulator in terms of energy band filling and its corresponding real space picture. The upper two plots describe a band insulator. It has a fully-filled band illustrated in graph (a), or equivalently, fully–filled sites with each site occupied by electrons of opposite spins as shown in graph (c). The lower two plots are relevant to a Mott insulator. The split of the energy band into two subbands due to strong e-e interaction is illustrated in graph (b) with the lower one fully filled. The corresponding real space occupation is shown in graph (d) where each site is singly occupied.

panel (d). Thus, no electron is allowed to move around due to both the strong e-e interaction and the Pauli exclusion principle.

1.2 Spin liquid state

In a spin liquid state, spins are bound into spin singlets between each other with opposite spins. Thus, the magnetization at each site has vanishing expectation value and no long range magnetic correlation exists on the lattice. A spin liquid state is a special type of paramagnetic states with the existence of a possibly momentum-dependent spin gap.

To understand this better, the spin liquid state can be contrasted to the standard textbook

example, a collection of weakly interacting local magnetic moments. In this example, the magnetizations are very similar to that of a spin liquid state at a finite temperature. However, there are important differences in the short distance magnetic correlations, most significantly, as temperature is reduced towards $T = 0$. The spin liquid state still maintains very similar properties as those at finite temperatures because of the existence of a spin gap. But the weak interaction existing in magnetic local moments would cause them to develop finite local magnetization, as is enforced by vanishing entropy at zero temperature.

In a strongly interacting magnetic system, the zero temperature state is usually magnetically ordered in order to reduce the entropy associated with the spin degree's freedom. This is not necessarily the case if there exists a strong geometrical frustration, which would reduce magnetic ordering and might totally change the system into a spin liquid state, where the spin degree's freedom is frozen in the singlet channel. It is also useful to contrast the spin liquid behavior discussed here with the nonmagnetic ground state in the Kondo lattice system (7), so-called heavy fermion materials. In the latter, the entropy is reduced and the magnetization is screened via the interaction between localized spins and conduction electrons. In the spin liquid materials discussed in this thesis, the interaction is between the strongly correlated electrons only.

1.3 Conventional vs. unconventional superconductivity

Since the discovery of the first superconducting material, Hg, in 1911 by H. K. Onnes (8), extensive experimental and theoretical studies have been carried out and reported in the literature. Several experimental discoveries contributed greatly to the progress in developing an appropriate theory to explain this fascinating phenomenon, including the Meissner effect, the isotope effect and flux quantization. These drove the theoretic studies to focus on the phonon-based interaction to mediate electron-electron attraction. Finally in 1957, Bardeen, Cooper, and Schrieffer came up with the microscopic theory, BCS theory, to correctly account for the superconducting phenomenon found till then (9).

The BCS theory might be most easily explained using an effective Hamiltonian involving a

weakly attractive e-e interaction, which includes both the phonon mediated e-e attraction and the screened e-e Coulomb repulsion, and can be written as

$$\hat{H} = \sum_{\mathbf{k},\sigma} \epsilon_{\mathbf{k}} c^{\dagger}_{\mathbf{k},\sigma} c_{\mathbf{k},\sigma} + \sum_{\mathbf{k},\mathbf{k}'} V_{\mathbf{k},\mathbf{k}'} c^{\dagger}_{\mathbf{k},\uparrow} c^{\dagger}_{-\mathbf{k},\downarrow} c_{\mathbf{k}',\uparrow} c_{-\mathbf{k}',\downarrow} \tag{1.1}$$

with $\epsilon_{\mathbf{k}}$ the dispersion for free electrons measured from Fermi energy,

$$V_{\mathbf{k},\mathbf{k}'} = \begin{cases} V < 0 & \text{for } |\epsilon_{\mathbf{k}}| \text{ and } |\epsilon_{\mathbf{k}'}| < \omega_c \\ 0 & \text{otherwise} \end{cases}$$

and ω_c the Debye frequency. By introducing the mean field pairing

$$\Delta_{\mathbf{k}} = \langle c_{\mathbf{k},\uparrow} c_{-\mathbf{k},\downarrow} \rangle \tag{1.2}$$

between two electrons with opposite momenta and spins, called a Cooper pair, the mean-field decoupled Hamiltonian can be shown to have a ground state

$$|\Phi_{BCS}\rangle \propto e^{-\sum_{\mathbf{k}} \phi_{\mathbf{k}} c^{\dagger}_{\mathbf{k},\uparrow} c^{\dagger}_{-\mathbf{k},\downarrow}} |0\rangle \,, \tag{1.3}$$

where $|0\rangle$ is the electron vacuum state, $\phi_{\mathbf{k}}$ describes the pairing amplitude at given momentum $\mathbf{k}$ and has an expression as

$$\phi_{\mathbf{k}} = \frac{\Delta_{\mathbf{k}}}{E_{\mathbf{k}} + \epsilon_{\mathbf{k}}}. \tag{1.4}$$

Here $E_{\mathbf{k}}$ is the dispersion relationship for quasiparticles involved in the Hamiltonian and is

$$E_{\mathbf{k}} = \sqrt{\epsilon^2_{\mathbf{k}} + \Delta^2_{\mathbf{k}}}. \tag{1.5}$$

The pairing in Eq. 1.2 can be homogeneous in momentum space, or equivalently $\Delta_{\mathbf{k}} = \Delta$, because of the specific interaction, V, chosen for the problem. This is called an s-wave pairing. In the BCS theory, Δ is at the same time the order parameter for the superconducting phase. From the quasiparticle dispersion relationship, Eq. 1.5, it can be seen that the dispersion develops a finite energy gap 2Δ on the Fermi surface due to the existence of effective attraction among electrons. This is a conclusion rooted in the weak interaction theory. Physically this means the formation of a Cooper pair is energetically favored over a pair of noninteracting electrons under weakly attractive interaction. These Cooper pairs move around phase coherently to give rise to superconductivity.

During the past few decades, new superconductors with unconventional properties have been discovered. They include some cuprates with high transitional temperature T_c (10), organic superconductors whose T_c are usually pretty low (11), and several heavy fermion compounds (12). We distinguish them from conventional superconductors by telling whether they are explainable within the BCS theory of phonon based mechanisms and the Fermi liquid theory in the normal state. Unconventional superconductivity is often featured by the existence of a non-s-wave pairing, whose pairing wavefunction between two electrons has a different spacial symmetry from that of the original lattice. For example, it can be a spacial $d_{x^2-y^2}$ -type symmetry where the wavefunction changes its sign when the material is rotated by $\pi/2$ in real or momentum space. This non-s-wave nature likely indicates that the mediation for the pairing is non-phononic. This is also reflected by the phases in the vicinity of the superconducting phase in the phase diagram of the material. Often they display physical features which cannot be simply explained by the Fermi liquid theory. For example in some organic superconductors, the superconducting state can be found to be sandwiched between a metallic and an insulating state by tuning other controlling parameters, for example, pressure. The fact that the insulating state is usually a Mott insulating state reveals the strong e-e interacting nature in these materials.

1.4 Introduction to the RVB mechanism

As mentioned above, the pairing wavefunction in unconventional superconductors is no longer isotropic, but differs in different spacial directions. This strongly supports a new pairing mechanism. For example, the fluctuation exchange (FLEX) theory (13) suggests that phonons are replaced by short ranged antiferromagnetic spin-fluctuation to mediate pairing. However, the nature of this theory is still weak coupling and is thus, in principle, unable to explain the systems involved in strong e-e interaction.

In contrast, P.W. Anderson took a different perspective (14). He avoided addressing what kind of bosonic quasiparticles might be responsible for the pairing of two electrons in the unconventional superconductors, but proposed that singlets pre-exist and resonate with each

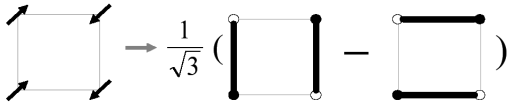

Figure 1.2 The ground state of the Heisenberg Hamiltonian (see the next section) involving 4 sites gives the simplest RVB state. The plot to the left of the arrow shows four spins on a square lattice whose spin orientations are not fixed as shown, the plot to the right illustrates a RVB state as the ground state of this Hamiltonian. It is made up of two products of two singlets (denoted by thick black lines) which resonate horizontally and vertically on the four sites.

other. By resonating it means that the same site participates in different singlets at the same time. The singlets become mobile under appropriate conditions and then the material would become superconducting if coherency emerges among these singlets. This is called the Resonating Valence Bond (RVB) picture, and is in close relation to the concept of a spin liquid state. The idea is illustrated in Fig. 1.2.

The RVB wavefunction originally proposed was

$$|\Psi_{RVB}\rangle = \hat{P}\,|\Phi_{BCS}\rangle\,, \tag{1.6}$$

where $\hat{P}$ is a projection operator to fully project out electronic configurations containing doubly occupied sites. These configurations usually have very high energy due to the strong e-e repulsion and are thus unlikely to appear. The possible weights for all possible electronic configurations are defined through $|\Phi_{BCS}\rangle$, called the underlying wavefunction in this thesis. Nowadays more general forms of this wavefunction have been introduced (15)(16). The advantage of the RVB picture is that it incorporates unconventional pairing, pseudogap phenomenon and in special cases, superconductivity in a natural way. Recent numerical work shows that this picture could satisfactorily explain different phenomena for the cuprates (17). Besides this success, it naturally assumes that superconductivity must be controlled by the existence of a pseudogap (1)(18). This might act as a test on the validity of this picture for the unconventional superconductivity. Shortcomings of the RVB theory include its difficulty

in being treated analytically due to the superimposed projection operator as well as difficulties in dealing with possible excited states. The Gutzwiller approximation may act as a partial solution to the first concern (19).

1.5 Generic models for strong electron-electron interaction

Hubbard Hamiltonian The relevant model used in this research to describe the strong e-e interaction is the Hubbard Hamiltonian (20)(21)(22)

$$\hat{H} = \sum_{\langle i,j \rangle} t_{ij} \left(c^{\dagger}_{i,\sigma} c_{j,\sigma} + h.c. \right) + U \sum_{i} n_{i,\uparrow} n_{i,\downarrow} \tag{1.7}$$

or its generalization

$$\hat{H} = \sum_{\langle i,j \rangle} t_{ij} \left(c^{\dagger}_{i,\sigma} c_{j,\sigma} + h.c. \right) + U \sum_{i} n_{i,\uparrow} n_{i,\downarrow} + \sum_{\langle i,j \rangle,\sigma,\sigma'} V_{ij} n_{i,\sigma} n_{j,\sigma'} + ... \tag{1.8}$$

where $\langle i,j \rangle$ denotes nearest neighboring lattice sites and

$$t_{ij} = \int d\mathbf{r} \phi^{*}_{i}(\mathbf{r}) \left[-\frac{\hbar^2}{2m} \nabla^2_{\mathbf{r}} + V(\mathbf{r}) \right] \phi_j(\mathbf{r}) \tag{1.9}$$

$$U = \int d\mathbf{r}_1 d\mathbf{r}_2 \left| \phi_i(\mathbf{r}_1) \right|^2 \frac{e^2}{|\mathbf{r}_1 - \mathbf{r}_2|} \left| \phi_i(\mathbf{r}_2) \right|^2 \tag{1.10}$$

$$V_{ij} = \int d\mathbf{r}_1 d\mathbf{r}_2 \left| \phi_i(\mathbf{r}_1) \right|^2 \frac{e^2}{|\mathbf{r}_1 - \mathbf{r}_2|} \left| \phi_j(\mathbf{r}_2) \right|^2 . \tag{1.11}$$

They are based on two fundamental assumptions: i) an adequate description of the physics is possible by including a limited number of local orbits; ii) the shape of the atomic orbit is independent of the electronic occupation (23).

The underlying basis set for the above Hamiltonian is composed of the Wannier states defined in case of a single band as

$$\phi_i(\mathbf{r}) = \frac{1}{\sqrt{N}} \sum_{\mathbf{k}} e^{-i\mathbf{k}\cdot\mathbf{R}_i} \varphi_{\mathbf{k}}(\mathbf{r}) . \tag{1.12}$$

Here N is the total number of lattice sites, $\varphi_{\mathbf{k}}(\mathbf{r})$ is the Bloch state for an electron at momentum $\mathbf{k}$ confined to the first Brillioun zone and $\mathbf{R}_i$ denotes a specific lattice site. The Wannier states are specifically designed to be mutually orthonormal,

$$\langle \phi_i | \phi_j \rangle = \delta_{i,j}. \tag{1.13}$$

It is worth mentioning that ϕ_i differs from the local atomic orbit implicitly contained in φ in Eq. 1.12 by having an oscillatory tail to maintain orthogonality to other Wannier states. The physical parameter t_{ij} is related to the kinetic energy for an electron to hop between nearby sites; U, V_{ij} etc. denote the Coulomb repulsions for two electrons to occupy the same or neighboring sites respectively.

That the e-e interaction is strong interaction is based on the fact that

$$U \gg t_{ij},$$

which implys that the width of the energy band is relatively narrow for materials with strong e-e interaction. This fact can be interpreted using a more physical perspective. Narrow bands require a small overlap of atomic orbits on nearby sites and are treated with the tight binding approximation (5). Considering that an atomic orbit has the largest probability around a lattice site, the small overlap in the wavefunction doesn't change this fact but enables the same electron to appear equally likely at each lattice site. When another electron is introduced, the same scenario also applies to it. This means the two electrons would have a larger probability to meet with each other at the same lattice site if their wavefunction overlap is less. This in general leads to a stronger e-e interaction between two electrons.

The Hubbard model contains the essence to describe a Mott-Hubbard transition. For $U \to 0$, it reduces to an independent electron problem and a half-filled band gives metallic behavior; for $U \to \infty$, electrons are fully localized at each site and are thus unable to move around if each site is occupied by a single electron, or termed half-filling.

$t-J$ Hamiltonian When U is large, the Hubbard Hamiltonian can be expressed as the $t-J$ Hamiltonian using a canonical transformation (17)(24). Practically, this transformation projects the Hubbard Hamiltonian into a subspace where each site is singly occupied. The double occupancy only appears as a virtual process to enable electron and spin to be exchanged. This is a reasonable approximation to start with if other typical energy scales in the problem are much smaller than the onsite repulsion U.

Up to the second order in t_{ij}/U, the $t-J$ Hamiltonian can be expressed as

$$\hat{H}^{t-J} = \hat{H}_k + \hat{H}_J \tag{1.14}$$

with

$$\hat{H}_k = -\sum_{\langle i,j\rangle} t_{ij} \left(n_{i,\bar{\sigma}} c^\dagger_{i,\sigma} c_{j,\sigma} n_{j,\bar{\sigma}} + h_{i,\bar{\sigma}} c^\dagger_{i,\sigma} c_{j,\sigma} h_{j,\bar{\sigma}} \right) \tag{1.15}$$

$$\hat{H}_J = -\sum_{i,j,k;\sigma,\sigma'} \frac{t_{ij} t_{jk}}{U} \left(h_{i,\bar{\sigma}} c^\dagger_{i,\sigma} c_{j,\sigma} n_{j,\bar{\sigma}} c^\dagger_{j,\sigma'} c_{k,\sigma'} h_{k,\bar{\sigma}'} \right) \tag{1.16}$$

where $h_{i,\sigma} = 1 - n_{i,\sigma}$, $n_{i,\sigma} = c^\dagger_{i,\sigma} c_{i,\sigma}$. Physically $\hat{H}_k$ describes the direct hopping process for an electron to reach its empty neighbors. $\hat{H}_J$ describes a virtual hopping process for an electron to reach its occupied neighbors to form an instant doubly occupied site (doublon); and then its partner either hops back if $i = k \neq j$, so-called the virtual exchange process, or hops to a third empty site if $i \neq j \neq k$, as is called the three-site hopping process.

In case of half-filling, the $t-J$ Hamiltonian reduces, up to a constant energy shift, to the Heisenberg Hamiltonian

$$\hat{H}_h = \sum_{\langle i,j\rangle} J_{ij} \hat{\mathbf{S}}_i \cdot \hat{\mathbf{S}}_j \tag{1.17}$$

where

$$J_{ij} = \frac{4t_{ij}^2}{U} \tag{1.18}$$

$$\hat{\mathbf{S}}_i = \frac{1}{2} \sum_{\sigma,\sigma'} \tilde{c}^\dagger_{i,\sigma} \tau_{\sigma,\sigma'} \tilde{c}_{i,\sigma'} \tag{1.19}$$

with $\tilde{c}_{i,\sigma} = c_{i,\sigma} \left(1 - n_{i,\bar{\sigma}}\right)$ and τ denoting the vector composed of the 3 Pauli matrices.

A brief summary on theoretical treatments to these models The usual practice treats a Hamiltonian through perturbations if the interaction is weak. But this is not possible for the Hubbard Hamiltonian with $t_{ij} \approx U$ when e-e interaction becomes strong. On the other hand, the treatment on the $t-J$ Hamiltonian is also complicated by the intrinsic restriction to require each site to be singly occupied.

To make some theoretical progress, different approaches have been proposed and are briefly mentioned below. For the Heisenberg Hamiltonian, besides the usual spin wave expansion (5),

spin coherent-state representation has been introduced to allow a field theoretical treatment (25). To analyze the $t-J$ or Hubbard Hamiltonian, slave-boson representation is introduced, where the charge and spin properties of a dressed electron are assumed to be decomposable,

$$\tilde{c}_{i,\sigma} = f_{i,\sigma} b_i^\dagger$$

with

$$\sum_\sigma f_{i,\sigma}^\dagger f_{i,\sigma} + b_i^\dagger b_i = 1$$

for the $t-J$ Hamiltonian and

$$\sum_\sigma f_{i,\sigma}^\dagger f_{i,\sigma} + b_i^\dagger b_i \leq 2$$

for the Hubbard Hamiltonian. Here $\tilde{c}_{i,\sigma} = c_{i,\sigma}\,(1 - n_{i,\bar{\sigma}})$, $f_{i,\sigma}$ satisfies a fermionic anticommutation relationship to represent spin degree's freedom while b_i satisfies a bosonic one to represent charge degree's freedom. After applying a mean field decoupling, some theoretical progress can be made with this approach (26). Other approaches include: Dynamical Mean Field theory(DMFT) (27) and Dynamical Cluster approximation(DCA) (28) to go beyond a mean field treatment. Alternatively the Exact Diagonalization(ED) is restricted to a small lattice size. Different types of Quantum Monte Carlo(QMC) methods are able to treat these Hamiltonians appropriately for all temperature range, but the sign problem (29) and heavy numerical complexities are involved. Another simple yet physically meaningful method is the variational Monte Carlo(VMC) simulation (30). It allows for clear physical insights into the problem if one properly guesses its ground state wavefunction. Yet it is restricted to zero temperature and is very hard to get information for excited states.

1.6 Introduction to organic superconductors

General description of organic charge transfer salt Organic superconductors belong to the class of material called organic charge transfer salt where electrons are transferred not between single atoms but between big organic molecules. In these molecules, the atomic orbits hybridize to share electrons among all the relevant atoms there. The hybridization alters the ionization energy or electron affinity of valence electrons of the whole molecule. Thus it

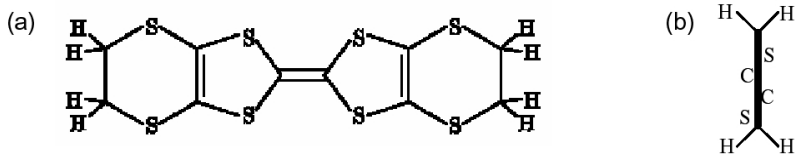

Figure 1.3 The bis(ethylenedithio)tetrathiafulvalene molecule. The planar view is shown in (a) (31) and the side view in (b).

leads to rather different bond types from what would naively be expected based on individual atoms. The word "organic" stresses the fact that mobile carriers come from organic molecules which act as the donor or cation, while a second type molecule acts as the anion to accept electrons. Organic superconductors have so far been under intensive study and many review articles have been published. In this thesis, most of the references are cited from (31)(32)(33) and references contained within.

The organic molecule of interest in this work is bis(ethylenedithio)tetrathiafulvalene $[C_{10}S_8H_8]$ (abbreviated as BEDT-TTF or ET) and is illustrated in Fig. 1.3. The hybridization renders a single π orbit as the highest occupied molecular orbit(HOMO) extending perpendicular to the molecular plane. When organic molecules are packed close together, these π orbits overlap and form conduction bands. There is also small contribution from the lowest unoccupied molecular orbit(LUMO) in forming the conduction bands. Different packing motifs of the molecules are represented by different Greek letters, for example, the α, β and κ types illustrated in Fig. 1.4. To form a crystal, anions are needed and they form insulating layers. Different anion molecules X, say, $Cu\left[N\left(CN\right)_2\right]Br$, $Cu\left(NCS\right)_2$, I_3, $Cu_2\left(CN\right)_3$ etc, can be chemically combined with ET in the usual form of $(\mathrm{ET})_2X$ where on the average two ET molecules lose one electron to X. The whole material is a layered structure with the insulating layers separating nearby conducting layers made up of ET molecules, as shown in Fig. 1.5. Notice here the special arrangements of the ET molecules in panel (b). Two molecules face each other; these two molecules as a whole are nearly perpendicular to the nearby pairs, forming the κ type packing pattern shown in the third graph of Fig. 1.4. This layered structure is responsible for

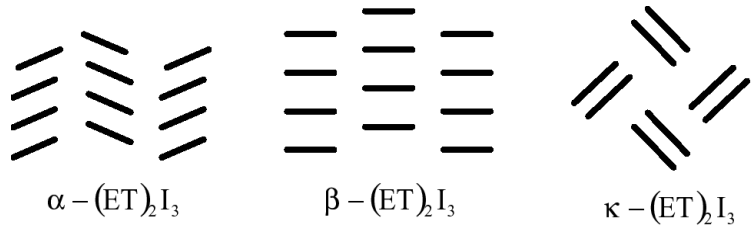

Figure 1.4 Schematic packing pattern of ET molecules of three different phases of $(ET)_2I_3$. Here each short line segment denotes an ET molecule (31).

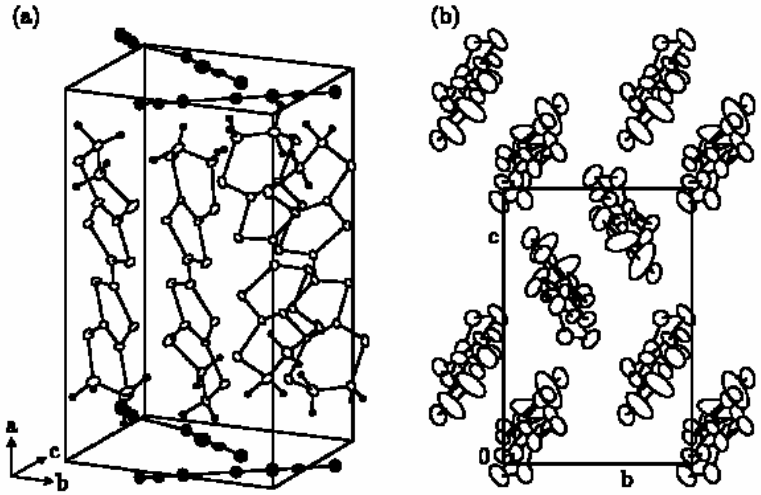

Figure 1.5 Structure of the κ-(BEDT-TTF)$_2Cu(NCS)_2$. (a) 3D view of the molecular arrangement. The BEDT-TTF molecules pack in planes separated along the a axis by layers of smaller $Cu(NCS)_2$ anions represented by line segments with filled dots on it. (b) Top view along the a axis onto the BEDT-TTF layer. The close packing of BEDT-TTF molecules allows substantial overlap of the molecular orbitals between two ET molecules. The square shown on the plot illustrates a unit cell of the lattice (34).

the low dimensional character of the material and is experimentally manifested in the Fermi surface measurements on $\kappa-(\mathrm{ET})_2\,Cu\,(NCS)_2$ (35), as is shown in Fig. 1.6. Also notice in the panel (a) of Fig. 1.5 that the ET molecules stand against the insulating layers. This leads people to believe that the material can be easily compressed, as is also experimentally verified (36). The physical properties of the organic charge transfer salt are affected by the size and type of the organic molecules, molecular stacking pattern, ethylene groups at the endpoints of the molecular backbones and the types of anions (31). Of course, they are also affected by the usual thermodynamic quantities: P, T, H, and strain etc.

Strong electron-electron interaction in $\kappa-(\mathbf{ET})_2\,X$ Under ambient pressure, $\kappa-(\mathrm{ET})_2\,X$ can have diverse phases for different choices of X. For example, it can be antiferromagnetic ($X=Cu\,[N\,(CN)_2]\,Cl$ (37)), a spin liquid ($X=Cu_2\,(CN)_3$ (4)(38)) or a superconductor ($X=Cu\,(NCS)_2$ (39)). As hydrostatic pressure exerting on the material increases, a phase transition takes place between an insulator and a superconductor at a temperature below several Kelvins (31)(32). This pressure-induced phase transition is a typical Mott-Hubbard type phase transition reflecting the strong e-e interaction. This interaction is also revealed by optical conductivity measurements carried out on $X=Cu\,(NCS)_2$, which is an ambient pressure superconductor (40). In the experiment, the DC Drude weights are different for two temperature values, as shown in Fig. 1.7, which cannot be explained with the simple band theory. Further on, the superconducting phase is found to be unconventional. The pairing has been concluded to be of singlet nature for $X=Cu\,[N\,(CN)_2]\,Br$. Numerous evidences support a d-wave pairing, e.g., the tunneling experiment on $X=Cu\,(NCS)_2$ (42) shown in Fig. 1.8. In the figure, it is easy to see that a varying d-wave pairing gap in the conduction plane reproduces reasonably well the data at different angles for small bias voltage. The gap amplitude vanishes around $\phi=51^\circ$.

Phase diagram for $\kappa-(\mathbf{ET})_2\,Cu_2\,(CN)_3$ The actual material of interest in this thesis is the κ-phase with anion type $X=Cu_2\,(CN)_3$. It was first discovered by U. Geiser, H. H. Wang et al in 1991 (43) and later revisited by Y. Shimizu, K. Miyagawa et al in 2003

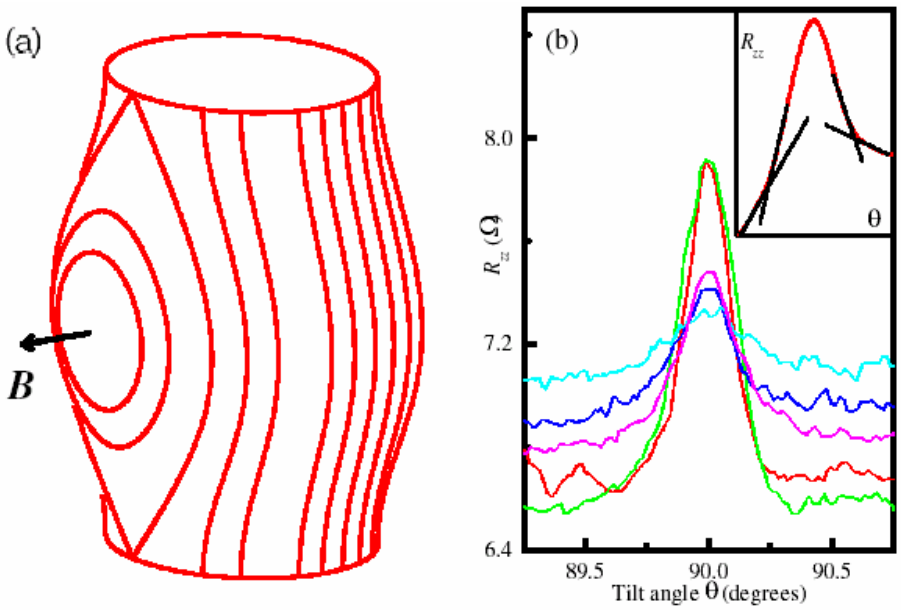

Figure 1.6 (a) Quasi-2D Fermi surface with weak interlayer dispersion effect. The curved lines and circles illustrate some of the quasiparticle orbits caused by an in-plane field B in the conduction plane. (b) Interlayer resistance R_{zz} of κ-(BEDT-TTF)$_2Cu(NCS)_2$ sample as a function of magnetic–field orientation($\theta = 90°$ corresponds to the in-plane magnetic field). Data for $T = 0.48K, 1.4K, 3.0K, 4.4K$ and $5.1K$ are shown, higher background magnetoresistance corresponding to increasing T. The inset shows the intersections of the linear extrapolations used to determine the peak width (35).

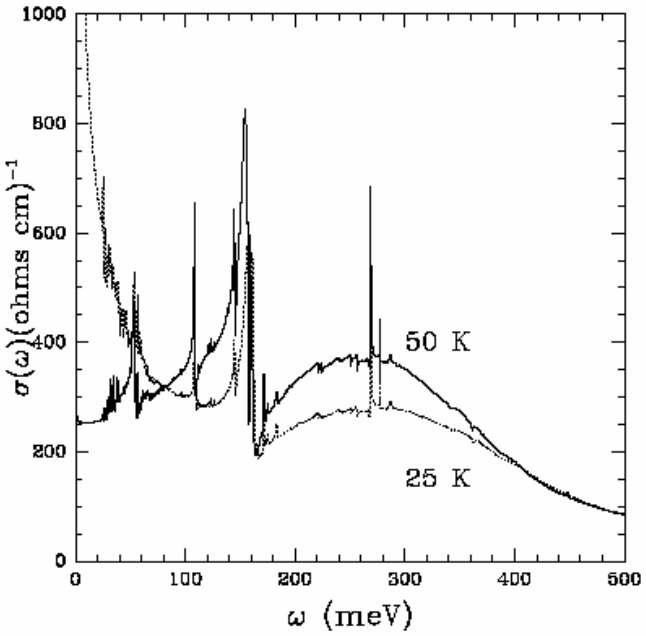

Figure 1.7 Non-Drude behavior of the frequency-dependent conductivity $\sigma(\omega)$ of $\kappa - (\mathrm{ET})_2 X$ with $X = Cu[N(CN)_2]Br$. Notice the strong temperature dependence of the low-frequency conductivity. The broad peak around $300meV$ can be identified with transitions between the lower and upper Hubbard subbands. The very sharp spikes are due to infra-red active phonons. The data shown is for the electric field along b axis, defined in Fig 1.5, in the molecular layer (41).

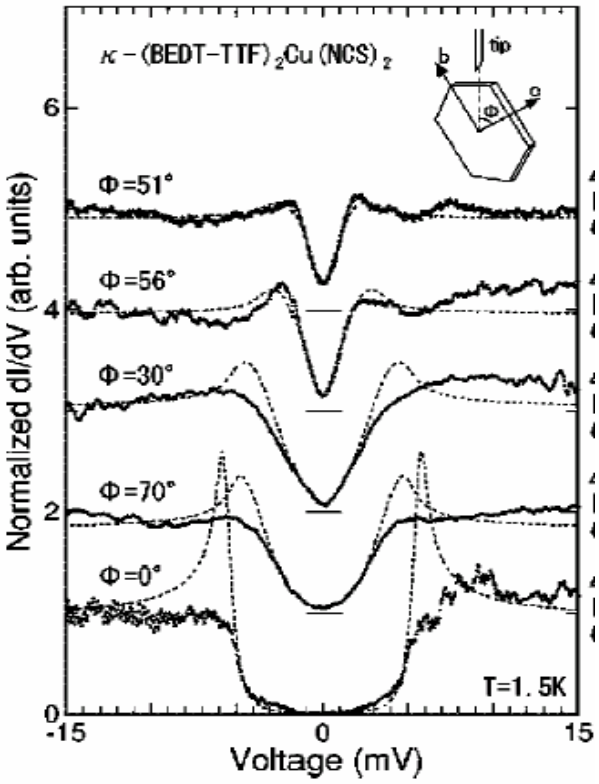

Figure 1.8 (dI/dV) data obtained in tunnelling experiments on the lateral surfaces of a $\kappa-(\text{BEDT-TTF})_2Cu(NCS)_2$ single crystal (solid lines; $T = 1.5K$). The inset shows the tunnelling direction defined as angle ϕ in the b-c conduction plane, defined in Fig 1.5. The dashed curves are a fit to a d-wave pairing model (42).

(4). Fig. 1.9 shows NMR measurements both on this material, shown in panel (a), and on another one with $X = Cu(NCN)_2Cl$ in panel (b) as a comparison. Although the absorption spectrum for this material gives only a persistent nonmagnetic state, which is manifested by very weak dependence on temperature, the ground state is strongly suggested to be a spin liquid state at ambient pressure. What is, perhaps, most interesting about this material is that pressure can tune the spin liquid state into a superconducting state without ever entering a magnetically ordered state. Similar to identifying that the isotope effect always goes with a conventional superconducting state, this is very important in answering whether unconventional superconductivity is always tied to the proximity to a magnetic phase transition or just a Mott transition or both (44). Meanwhile this seems to argue against theories that require long range antiferromagnetic fluctuation as the pairing mediator. Recently the whole phase diagram was mapped out in the $T - P$ plane for this material (45) and is shown in Fig. 1.10. Besides the vertical drop of the first order phase transition line at $T = 0$ around $P_c \approx 3.6 \times 10^{-1} GPa$, it is peculiar that $\partial T_c/\partial P > 0$ holds along that transition line for low yet finite T. By Clausius-Clapeyron relation,

$$\left.\frac{\partial T_c}{\partial P}\right|_{\text{phase boundary}} = \frac{\Delta V}{\Delta S},$$

where ΔV and ΔS are the volume and entropy jumps at the 1^{st} order phase transition, respectively. Notice the positive slope of the line. Since the volume decreases with pressure, the entropy also decreases when the spin liquid phase transits to the unconventional superconducting phase. This is very likely to exclude the existence of a finite spin gap in the spin liquid phase if the entropy of the unconventional superconducting phase has a power law dependence on T.

Model Hamiltonian to describe $\kappa - (\mathbf{ET})_2 Cu_2 (CN)_3$ The natural guess for the Hamiltonian description of the system is the use of the Heisenberg Hamiltonian for the spin degree's of freedom, because of the existence of the spin liquid insulating ground state at ambient pressure in this material. But this cannot explain the fact that the material can be tuned into a superconductor under pressure, which alters t/U with t being bandwidth

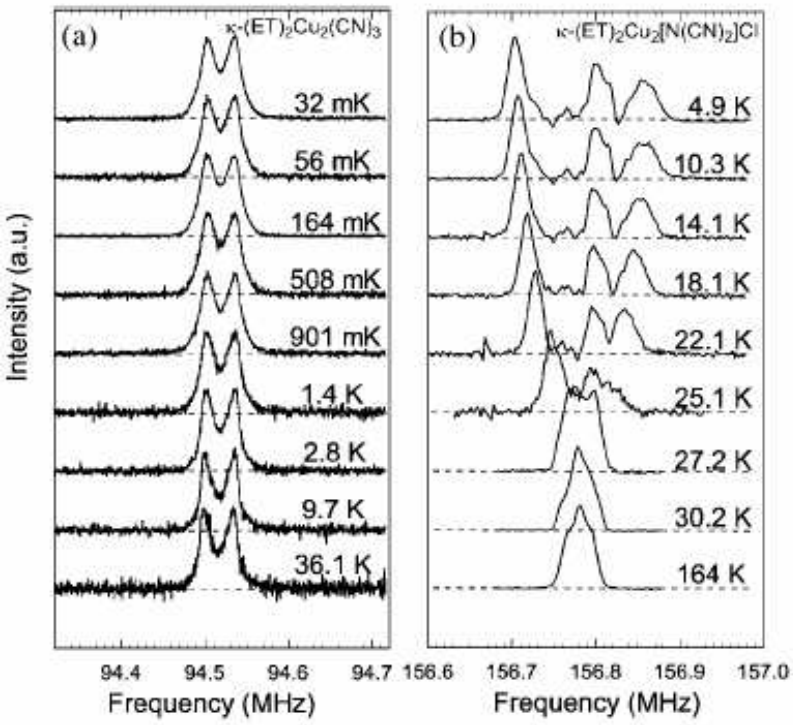

Figure 1.9 ^{1}H NMR absorption spectra for a single crystal of $\kappa-$(BEDT-TTF)$_2Cu_2(CN)_3$ in panel (a) and $\kappa-$(BEDT-TTF)$_2Cu(NCN)_2Cl$ in panel (b) (37) under the magnetic field perpendicular to the conduction plane. The spectra show nuclear dipole interactions between the protons in the ethylene groups in the ET molecule of both materials. The difference in the spectra shape at high temperature for both materials can be interpreted by different orientations of ET molecules against external magnetic field and is thus not important here. To panel (b), the spectra of $\kappa-$(BEDT-TTF)$_2Cu(NCN)_2Cl$ split below $27K$ reflecting a transition to an antiferromagnetic ordered state; to panel (a), however, the shape and location of the spectra of $\kappa-$(BEDT-TTF)$_2Cu_2(CN)_3$ don't show distinct change throughout the temperature range from $36.1K$ to as low as $32mK$, which is 4 orders of magnitude below the J value of $250K$. The result indicates the absense of long range magnetic ordering and strongly suggests a spin liquid state on the strongly spin frustrated triangular lattice (4).

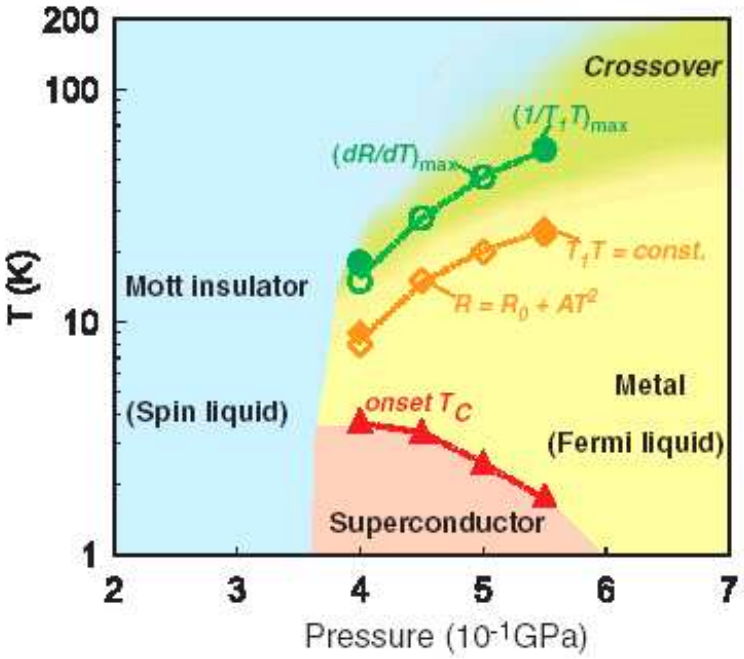

Figure 1.10 The $T-P$ phase diagram of $\kappa-(\text{BEDT-TTF})_2Cu_2(CN)_3$ constructed through resistance and NMR measurements under the hydrostatic pressure. Details to green and orange curves (the upper two curves) are stated in the reference and are irrelevant to this work. The red curve (the lowest one) showing the onset superconducting T_c was determined from the in-plane resistance measurements (45).

but does not change the band filling. This is because the Heisenberg Hamiltonian requires single occupation on each site and thus it always gives insulating behavior if the number of charge carriers doesn't change. Considering that increased pressure enhances charge carriers to delocalize, double occupancy must be allowed to enable charge carriers to move around. Thus the Hubbard Hamiltonian is a more reasonable choice to describe this type of material.

The question is then how to determine different hopping parameters t_{ij} and the onsite Hubbard energy U for this material. An analysis has been carried out on a two-molecule problem in (23) (46). It is assumed that electrons sit in HOMOs. The basic idea is to map the expected Hubbard model, defined as

$$\hat{H}_{em} = t \sum_{\sigma} \left(c^{\dagger}_{1,\sigma} c_{2,\sigma} + c^{\dagger}_{2,\sigma} c_{1,\sigma} \right) + U \sum_{i=1,2} n_{i,\uparrow} n_{i,\downarrow} + V \sum_{\sigma,\sigma'} n_{1,\sigma} n_{2,\sigma'}, \tag{1.20}$$

to a first principle calculation to microscopically obtain the relevant parameters based on the bare Hamiltonian,

$$\hat{H}_{1st} = \sum_{i=1,}^{n} \left(-\frac{1}{2} \nabla_i^2 + \hat{v}\left(i\right) \right) + \sum_{i<j}^{n} \frac{1}{r_{ij}}, \tag{1.21}$$

where t, U and V follow the definitions from Eq. 1.8; $n = \sum_{i=1,2;\sigma} c^{\dagger}_{i,\sigma} c_{i,\sigma}$ denotes total number of electrons on the two molecules, $\hat{v}\left(i\right)$ denotes attraction from core electrons and the ion and r_{ij} denotes distance between two electrons. It is found that t for two molecules facing each other is much stronger than they are otherwise. Thus these two molecules should be treated together as a unit called dimer to build the lattice. It is also found that U is much smaller than the bare U_0 because the addition of another electron onto the same molecule would force the existing electrons to reorganize themselves either on the same molecule or to be transferred to the other one in the dimer in order to lower the electrostatic energy (47). Similar effects also exist on the lattice which reduce U even further.

By introducing the concept of dimer in the κ type organic superconductors, the planar lattice made up of ET molecules can be abstracted as a triangular lattice having effective hoppings of different strength along different directions. The mapping is shown in the panel (a) and (b) of Fig. 1.11 and a topologically equivalent square lattice with specific diagonal hoppings is shown in the panel (c).

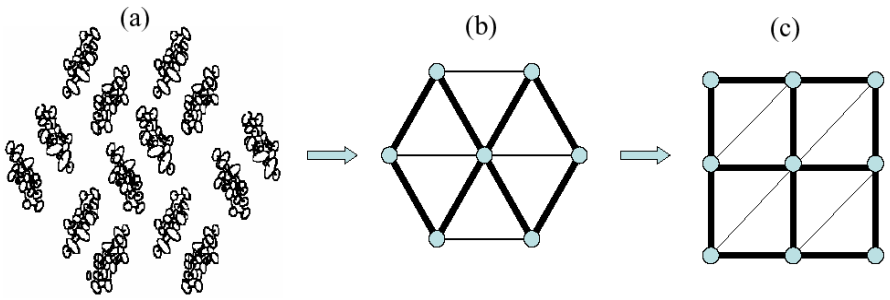

Figure 1.11 Illustration of how the abstract lattice is obtained from the actual lattice, which is made up of ET molecules shown in panel (a). By replacing the two molecules facing each other with a dimer and denoting it with a filled circle, the abstract lattice is shown in panel (b) where the thickness of the line segment represents the strength of the effective hopping along that specific direction. The triangular lattice can be transformed isomorphically into a square lattice with specific diagonal hoppings of different strengths, as shown in panel (c).

The effective Hubbard Hamiltonian to describe the square lattice related to 2D organic superconductors can be expressed as

$$\hat{H} = -t \sum_{\langle i,j\rangle,\sigma} \left(c^{\dagger}_{i,\sigma} c_{j,\sigma} + h.c. \right) - t' \sum_{\langle k,l\rangle,\sigma} \left(c^{\dagger}_{k,\sigma} c_{l,\sigma} + h.c. \right) + U \sum_{i} n_{i,\uparrow} n_{i,\downarrow} \tag{1.22}$$

where t and t' represent different effective hoppings along nearest neighbor, denoted by $\langle i,j\rangle$, and diagonal directions, denoted by $\langle k,l\rangle$, respectively, U denotes onsite repulsion for two electrons to sit on the same dimer site. The typical parameters for organic superconductors are estimated to be

$$t \approx 0.05 - 0.1eV,\ t' \approx 0.5 - 1.0t \text{ and } U \approx 5 - 10t$$

depending on the type of X. For $\kappa - (\mathrm{ET})_2 Cu_2 (CN)_3$ (4),

$$\frac{t'}{t} \approx 1.06$$

while the relevant U is less accurately determined.

With the dispersion well defined in terms of t and t', the band filling can be determined for the $\kappa-$ type packing pattern involving dimers as the building blocks. Each dimer carries

one hole and generates bonding and antibonding bands. Thus, the bonding band would be fully filled while the antibonding band would be half-filled. This is in agreement with the conclusions based on a Mott insulator model revealed in the different experiments.

Recent theoretical progresses on organic superconductors The strongly correlated nature of the materials were summarized in an early review (48). It was further substantiated by the inconsistencies between predictions based on weak coupling spin fluctuation approachs (49) and experimental measurements of the pairing gap (42). As one of the first works to include strong correlation effects into interpreting the superconductivity and its proximity to a spin liquid insulating state (44), we used a variational Monte Carlo simulation method with a new type of RVB wavefunction to describe the transition from a spin liquid state to a superconducting state. My work prompted a subsequent investigation on the same material (50). Other theories involve the Gutzwiller approximation of the Hubbard-Heisenberg Hamiltonian (51)(52), and recently a DMFT study on this problem as well. The phase diagram is successfully calculated using DMFT and is consistent with experimental measurements (53).

1.7 Introduction to $SrCu_2(BO_3)_2$

Related experimental facts Another Mott insulator of interest is $SrCu_2(BO_3)_2$, discovered in 1991 by R. W. Smith and D. A. Keszler (54). It has a tetragonal crystal structure with lattice constants $a = 8.995$ and $c = 6.649$ at room temperature. It has a layered structure with alternative $CuBO_3$ and Sr planes. The 3D view of the crystal is shown in panel (a) of Fig. 1.12 and a sketch of the $CuBO_3$ layer is shown in panel (b) there. In this layer Cu^{2+} ions connect each other either through BO_3 molecules or through two O sites and are located at crystallographically equivalent sites. Sr^{2+} ions do not sit directly above or below Cu^{2+} or B^{3+}, instead, they share quadrilateral faces of O sites to form one dimensional chains that extend parallel along c axis.

The magnetic ions are Cu^{2+} carrying a spin $S = 1/2$. The network structure formed by Cu^{2+} is shown in panel (c) of Fig. 1.12. A pair of nearest-neighbor Cu^{2+} ions are connected

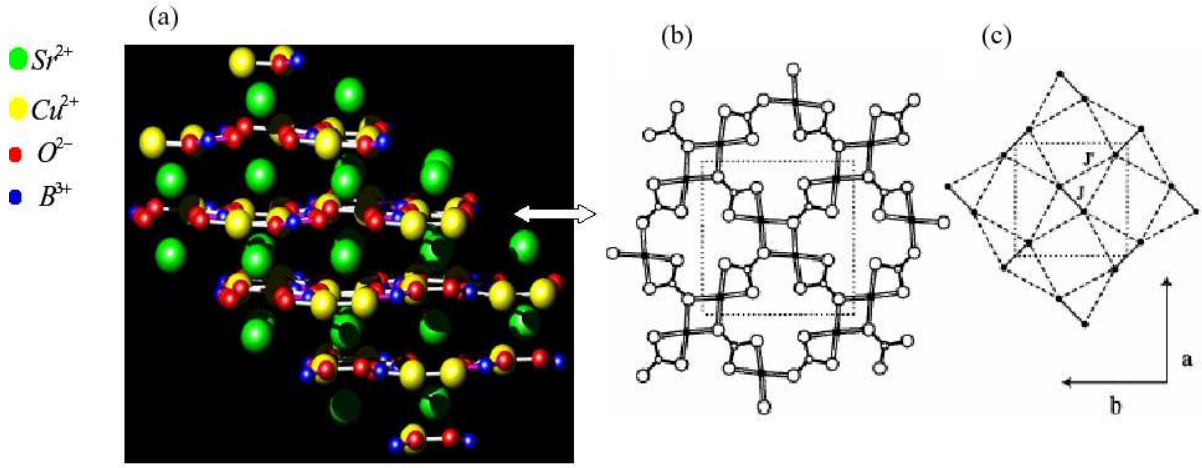

Figure 1.12 (a) Schematic 3D view of the crystal with each type of atoms shown with different color. (b) Schematic view of the crystal structure of $SrCu_2(BO_3)_2$ along [001]. The closed circles, small open circles, and large open circles denote, respectively, the Cu^{2+}, B^{3+}, and O^{2-} ions. The unit cell is indicated by dotted lines. (c) 2D coordinates of the Cu^{2+} spins. The first and second nearest neighbor Cu pairs are denoted by the solid and broken lines respectively. (55)

through O sites to form a dimer unit. They then connect orthogonally through BO_3 molecules to another dimer unit. The ions in a dimer are separated by 2.905Å and two next nearest neighbor Cu^{2+} ions by 5.132Å at room temperature. The magnetic property was revisited by H. Kageyama, K. Yoshimura, et.al (55) in 1999 and in other experiments later on (56). There are several unique features in this material, spin gapped behavior, almost flat dispersion for low energy excitation and existence of magnetization plateaux (56). There exists a spin gap of $\Delta \simeq 35$K manifested by exponentially decaying magnetic susceptibility when $T \to 0$ (55), as is shown in Fig. 1.13. The inelastic neutron scattering experiment (57) reveals that the first triplet excitation spectrum is nearly flat in momentum space. And there also exists magnetization plateaux of fractional Bohr magnetic moment, i.e. μ_B, per site in the magnetization curve (55)(58).

All these features can be explained reasonably well by the Heisenberg Hamiltonian

$$\hat{H}_h = \sum_{\langle i,j \rangle} J\hat{\mathbf{S}}_i \cdot \hat{\mathbf{S}}_j + \sum_{\langle l,m \rangle} J'\hat{\mathbf{S}}_l \cdot \hat{\mathbf{S}}_m \tag{1.23}$$

where $\langle i,j \rangle$ denotes next nearest neighbor spin sites and $\langle l,m \rangle$ denotes nearest neighbor spin sites illustrated in panel (c) of Fig. 1.12, and J and J' describe the corresponding exchange interactions accordingly. J and J' can be estimated by fitting the theoretical magnetic susceptibility to the experimental curve, which gives

$$J = 54\text{K and } J' = 85\text{K}.$$

More careful fits reveal a small component of interlayer coupling with $J'' = 5$K perpendicular to the $CuBO_3$ layer (56). This comparatively small value is an additional evidence for the quasi-2D nature of this material. There are additional experimental effects which call for corrections on the model expressed in Eq. 1.23, especially a Dzyaloshinsky–Moriya interaction (59)(60). However this interaction only becomes important in an applied magnetic field perpendicular to the Cu^{2+} plane. It is irrelevant for the effects to be investigated in this thesis.

Valence bond crystal as a ground state The spin lattice of $SrCu_2(BO_3)_2$ is topologically equivalent to the Shastry-Sutherland (SS) lattice (61), as is shown in Fig. 1.14.

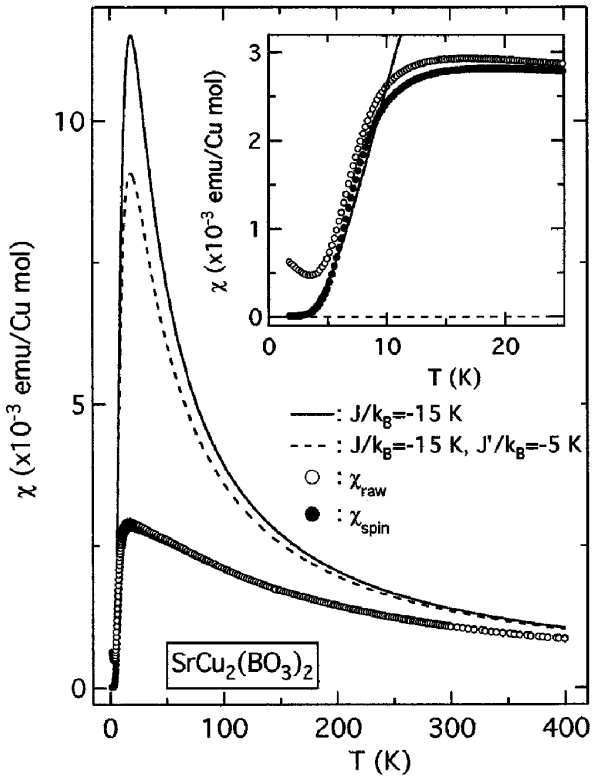

Figure 1.13 Temperature dependence of the magnetic susceptibility in $SrCu_2(BO_3)_2$ powder. The open and closed circles represent, respectively, the measured susceptibility χ_{raw}, and spin susceptibility χ_{spin} after subtracting the Curie-Weiss and constant terms from χ_{raw}. The solid and broken lines show the theoretical curves based on a dimer model. The enlarged plot is shown in the inset, where the solid curve indicates the fit to $\chi_{spin} \sim \exp(-\Delta_s/kT)$. (55)

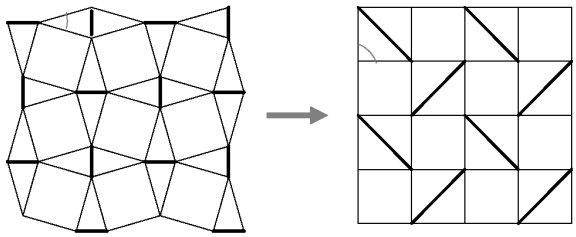

Figure 1.14 Illustration of topological equivalence of the actual spin lattice on the $CuBO_3$ plane (left) to the standard Shastry-Sutherland lattice (right). The actual spin lattice is also sketched in panel (c) of Fig 1.12. The equivalence is obtained by evolving the acute vertex angle shown on the top of the left lattice into a right one shown on the right lattice. (61)

The peculiarity of the SS lattice is that its ground state can be determined exactly as a singlet dimer state for a specific range of J'/J

$$|\Psi\rangle = \prod_{\langle l,m\rangle} \frac{1}{\sqrt{2}} \left(|l,\uparrow;m,\downarrow\rangle - |l,\downarrow;m,\uparrow\rangle\right) \tag{1.24}$$

where $\langle l,m\rangle$ denotes all the relevant diagonal bonds on the lattice and $|l,\uparrow;m,\downarrow\rangle$ denotes two holes with spin up at site l and spin down at site m. Since all the singlets are fixed on the diagonal bonds, this state is also called a valence bond solid or crystal. The exactness of the singlet dimer state as the ground state was first demonstrated by Shastry and Sutherland in Ref. (62) and the proof is briefly outlined below.

Firstly the Hamiltonian can be regrouped into the following form

$$\hat{H} = \sum_{\langle l,m\rangle} \left(\sum_a \hat{H}^a_{lm} \right), \tag{1.25}$$

with

$$\hat{H}^a_{lm} = \frac{J'}{2} \hat{\mathbf{S}}_l \cdot \hat{\mathbf{S}}_m + J \hat{\mathbf{S}}_a \cdot \left(\hat{\mathbf{S}}_l + \hat{\mathbf{S}}_m \right), \tag{1.26}$$

where sites a, l and m define an isosceles right triangle on the lattice with dimer bond $\langle l,m\rangle$ as the hypotenuse and site a as the vertex. This is illustrated in Fig. 1.15. By considering that

$$\hat{\mathbf{S}}_a \cdot \left(\hat{\mathbf{S}}_l + \hat{\mathbf{S}}_m \right) = \frac{1}{2} \left[\hat{S}^+_a \left(\hat{S}_l + \hat{S}_m \right)^- + \hat{S}^-_a \left(\hat{S}_l + \hat{S}_m \right)^+ \right] + \hat{S}^z_a \left(\hat{S}_l + \hat{S}_m \right)^z, \tag{1.27}$$

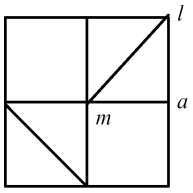

Figure 1.15 A triangle is specifically labeled to illustrate how the whole Hamiltonian $\hat{H}$ can be regrouped into a summation of unit Hamiltonians $\hat{H}^a_{lm}$ defined on each triangle.

with

$$\hat{S}^+ = \hat{S}^x + i\hat{S}^y \tag{1.28}$$

$$\hat{S}^- = \hat{S}^x - i\hat{S}^y, \tag{1.29}$$

where $\hat{S}^x, \hat{S}^y$ and $\hat{S}^z$ are the x, y and z components of the spin operator $\hat{\mathbf{S}}$ defined in Eq. 1.19, and noticing that $|\Psi\rangle$ is a direct product of all singlets along diagonal bonds, I can easily see that

$$\forall a,\ \hat{\mathbf{S}}_a \cdot \left(\hat{\mathbf{S}}_l + \hat{\mathbf{S}}_m\right) |\Psi\rangle = 0\,|\Psi\rangle\,. \tag{1.30}$$

Thus $|\Psi\rangle$ is an eigenvector of $\hat{H}$ with an eigenvalue of

$$E_{|\Psi\rangle} = -\frac{3}{8} N J'.$$

where N denotes total number of sites on the lattice. By Ritz variational principle, the actual ground state energy E_g cannot exceed $E_{|\Psi\rangle}$, or $E_g \leq E_{|\Psi\rangle}$.

On the other hand, there is the Anderson decomposition strategy (63) stating that the sum of the minimum energy of individual systems gives a lower bound of the total energy of the whole system. The proof is simple. Suppose that the whole Hamiltonian can be fully divided into different pieces without anything left unattended

$$\hat{H} = \sum_i \hat{H}_i \tag{1.31}$$

and there exist $|\psi_i\rangle$ as the ground state for each $\hat{H}_i$ such that $\forall\,|\varphi\rangle\,,\ \langle\varphi|\,\hat{H}_i\,|\varphi\rangle \geq \langle\psi_i|\,\hat{H}_i\,|\psi_i\rangle\,,$ then the ground state energy for $\hat{H}$ would satisfy

$$\begin{aligned}\langle\psi_H|\,\hat{H}\,|\psi_H\rangle &= \sum_i \langle\psi_H|\,\hat{H}_i\,|\psi_H\rangle \\ &\geq \sum_i \langle\psi_i|\,\hat{H}_i\,|\psi_i\rangle \end{aligned} \tag{1.32}$$

where $|\psi_H\rangle$ is the ground state for $\hat{H}$.

Applying it onto the SS lattice, one can get

$$\hat{H} = \sum_{\langle l,m\rangle}\sum_a \left[\frac{J'}{2}\hat{\mathbf{S}}_l\cdot\hat{\mathbf{S}}_m + J\hat{\mathbf{S}}_a\cdot\left(\hat{\mathbf{S}}_l+\hat{\mathbf{S}}_m\right)\right] \tag{1.33}$$

$$\geq \sum_{\langle l,m\rangle}\sum_a \left[\left(\frac{J'}{2}-J\right)\left(\hat{\mathbf{S}}_l+\hat{\mathbf{S}}_m\right)^2 - \frac{3}{8}J'\right]. \tag{1.34}$$

If $J'/J \geq 2$,

$$E_g \geq -\frac{3N}{8}J', \tag{1.35}$$

otherwise

$$E_g \geq 2N\left(\frac{J'}{2}-J\right) - \frac{3N}{8}J'. \tag{1.36}$$

Thus the upper and lower bounds for E_g coincide for $J' \geq 2J$ which means the singlet dimer state happens to be the exact ground state of the lattice.

In the other limit $J'/J \to 0$, the SS lattice reduces to the square lattice whose ground state is known to have antiferromagnetic long range order (15)(64). Considering both these limits, there is at least one phase transition at some critical $J'/J\big|_c$. This has been intensively studied using mean field or exact diagonalization methods and some intermediate phases have been introduced as the bridge between the singlet dimer state and the antiferromagnetic state (56)(65)(66). The accurate value for $J'/J\big|_c$ and the nature of the intermediate states are still open questions to be addressed. The consensus for $J'/J\big|_c$ is around 1.428 (56). Remember, the ratio to $SrCu_2\left(BO_3\right)_2$ is

$$\left.\frac{J'}{J}\right|_{SrCu_2(BO_3)_2} = 1.5741 \tag{1.37}$$

which is on the safe side of the singlet dimer ground state yet is very close to the critical ratio. Thus this ground state is expected to be fragile and strong quantum fluctuation is expected to play an important role upon doping or with changing frustration.

The sign of the diagonal hopping There are different ways to dope this material. Cu^{2+} ions can be directly replaced by ions without spins (in-plane doping), then the possible symmetry operations of the spin lattice would be reduced or even eliminated. What is of interest in this work is to replace Sr^{2+} with ions of valence other than 2 (out-of-plane doping). Then extra charge carriers can be introduced into the spin lattice while the lattice itself is still unaffected. By doping this way, the Hamiltonian to describe the doped system would be the $t-J$ Hamiltonian with possible three-site hopping term (not explicitly written out in the following expression)

$$\hat{H} = \sum_{\langle i,j\rangle,\sigma} t\tilde{c}^{\dagger}_{i,\sigma}\tilde{c}_{j,\sigma} + \sum_{\langle l,m\rangle,\sigma} t'\tilde{c}^{\dagger}_{l,\sigma}\tilde{c}_{m,\sigma} + \sum_{\langle i,j\rangle} J\left(\hat{\mathbf{S}}_i\cdot\hat{\mathbf{S}}_j - \frac{n_i n_j}{4}\right) + \sum_{\langle l,m\rangle} J'\left(\hat{\mathbf{S}}_l\cdot\hat{\mathbf{S}}_m - \frac{n_l n_m}{4}\right) \quad (1.38)$$

where

$$J = \frac{4t^2}{U} \text{ and } J' = \frac{4t'^2}{U},$$

$\tilde{c}_{i,\sigma} = c_{i,\sigma}\left(1-n_{i,\bar{\sigma}}\right)$, t and t' are hopping amplitudes on lateral and specific diagonal bonds on the lattice while U is the hidden onsite repulsion to give rise to the superexchange interaction J and J'. This is a natural extension from the Heisenberg Hamiltonian describing pretty well the undoped system.

There has, however, not been a generally acknowledged successful doping of this material in experiments. Thus, sofar, the values and signs of t and t' are unknown. To determine the magnitude and sign of these two hoppings, a band structure calculation was carried out by using a local density approximation(LDA) and it was then fitted to a tight binding model

$$\hat{H}_k = \sum_{\langle i,j\rangle,\sigma} tc^{\dagger}_{i,\sigma}c_{j,\sigma} + \sum_{\langle l,m\rangle} t'c^{\dagger}_{l,\sigma}c_{m,\sigma} \quad (1.39)$$

where $\langle i,j\rangle$ and $\langle l,m\rangle$ denote nearest and next nearest neighbor hoppings respectively on the SS lattice. The four branches of the energy dispersion at three symmetry points in momentum

space are

$$\varepsilon_\Gamma = \left(\varepsilon_0 - 4t + t', \varepsilon_0 - t', \varepsilon_0 - t', \varepsilon_0 + 4t + t'\right)$$

$$\varepsilon_X = \varepsilon_0 \pm \sqrt{4t^2 + t'^2} \text{ (each sign doubly degenerate)}$$

$$\varepsilon_M = \varepsilon_0 \pm t' \text{ (each sign doubly degenerate)}$$

where $\Gamma = (0,0)$, $X = (\pi, 0)$, $M = (\pi, \pi)$. We assume a unit lattice constant. The LDA calculation at the Γ-point gives

$$\varepsilon_\Gamma = (-0.15099\text{eV}, 0.0013\text{eV}, 0.0013\text{eV}, 0.5913\text{eV}).$$

This yields

$$t = 0.0927\text{eV},$$

$$t' = 0.10358\text{eV},$$

$$\varepsilon_0 = 0.11657\text{eV},$$

or

$$t = 1043\text{K and } t' = 1205\text{K}.$$

The ratio $t'/t \simeq 1.15$ is slightly smaller than $\sqrt{J'/J}$ determined experimentally. Yet only sign of t and t' is stressed in this calculation since only this information is unambiguously determined. In my work, I adapt the convention used in (61) and assume $J = 0.3t$, which includes band renormalization effect not included in the LDA calculation. The overall fit of the first principle calculation together with the tight binding model fit is shown in Fig. 1.16. From the fit, it is clear that the noninteracting picture for the undoped $SrCu_2(BO_3)_2$ predicts a semi-metal considering that each unit cell contains 4 charge carriers. The fact that this material is an insulator assumes the existence of strong e-e interaction which changes the conducting nature of the material.

Current progress on doped $SrCu_2(BO_3)_2$ So far, some mean field type analysis have been performed to investigate doping effects in this material. Different phases are proposed,

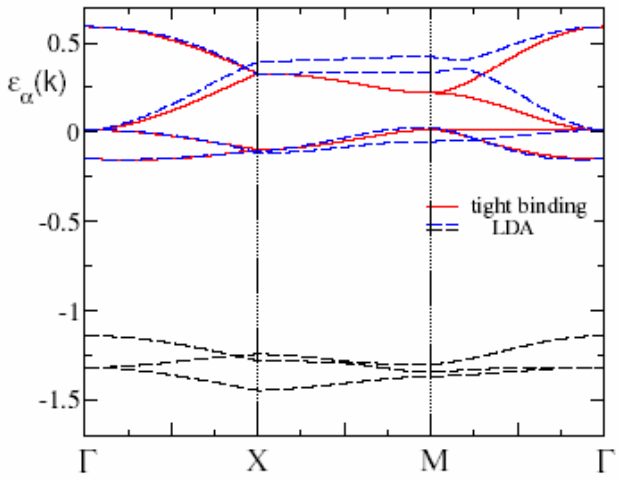

Figure 1.16 The bandstructure of $SrCu_2(BO_3)_2$ is obtained using density functional theory and denoted with dashed curve in the plot. A tight binding fit of the Shastry Sutherland lattice is superimposed with solid red curve which perfectly agrees with the Γ point in the dispersion. Only in-plane dispersion and the fits closest to the Fermi level are shown.

including superconducting phases (61)(67), flux phases (67) etc. As I will demonstrate, these results are due to the mean field nature of the method and their validity is questionable. Nevertheless, they give hints on the possible phases the material should have and how well the mean field approach would be potentially applicable to the current problem. On the other hand, exact diagonalization calculation predicts an insulating phase for the electron doping on a 32-site lattice by considering an out-of-plane doping (68). This calculation predicted isolated holes on the lattice and similar magnetic correlation pattern as on the parent compound. A very special variational study aimed at in-plane doping was carried out in (69). They looked at the in-plane magnetic correlation by considering how all the other spins respond to the impurity site. Experimentally, this material is very hard to be doped. So far there is only one publication available on Sr^{2+} replacement (70). The major conclusion is that the material remains insulating for either hole or electron doping. However, recent advances in the sample preparation of transition metal oxides give us every reason to be optimistic that the obstacles can be overcome in the doping of this material (71).

1.8 Main objectives and results

This paragraph outlines the main physical aspects, major objectives and the results relevant to my research. The RVB picture is very promising in describing the unconventional superconductivity (1) and it is most appropriate to describe a transition originated from a spin liquid state because it itself is such a state. Following the RVB picture (14), I used specific many-body trial wavefunctions to look into the zero temperature ground state properties of two different materials, $\kappa-(\mathrm{ET})_2 X$ and $SrCu_2(BO_3)_2$, both of which are believed to reflect different aspects of the same strongly correlated RVB physics. The generic form of the RVB wavefunction has been introduced in Eq. 1.6, but is rewritten here for emphasis because this is the central physical idea exploited in this thesis,

$$|\Psi_{RVB}\rangle = \hat{P}\,|\Phi_{BCS}\rangle\,. \tag{1.40}$$

Here $\hat{P}$ denotes some real space projection reflecting specific strongly correlated physics under consideration and $|\Phi_{BCS}\rangle$ is some generic BCS wavefunction.

The method to optimize the wavefunction is to use the variational Monte Carlo (VMC) simulation. The quantity to be minimized is the energy expectation evaluated as

$$\bar{E} = \frac{\langle \Psi_{RVB} | \hat{H} | \Psi_{RVB} \rangle}{\langle \Psi_{RVB} | \Psi_{RVB} \rangle}. \tag{1.41}$$

where $\hat{H}$ is the Hamiltonian to describe the specific system. The energy depends on many variational parameters, including parameters occurring in $\hat{P}$, to be explained in more details in the next chapter, and in $|\Psi_{RVB}\rangle$ such as effective hoppings between sites i and $j, \tilde{t}_{ij}$, variational chemical potential at site $i, \tilde{\mu}_i$, and pairing gaps between sites i and $j, \tilde{\Delta}_{ij}$. The complexity to a specific problem depends on the number of variational parameters and the size of the lattice. Likewise, other physical observables characterized by operator $\hat{O}$ can also be evaluated similarly as $\bar{E}$.

The application of the RVB approach to the organic superconductor and to the Shastry-Sutherland model is the major innovative aspect in this thesis. In order to explore the phase space most efficiently during the VMC simulation, a simple algorithm is developed to update steps for the variational parameters. In order to treat the complex unit cell structure in the SS model, a generalized multiband BCS wavefunction is derived. These two are the major technical developments involved in the research.

As compared to the standard BCS wavefunction, the multiband BCS wavefunction is able to describe inter- and intra-band pairing. Detailed derivations would be skipped here but only a brief introduction to the relevant notations is offered. The analytic expression for the multiband BCS wavefunction is written as

$$\left|\Phi_{BCS}^{M}\right\rangle = \prod_{n,n',\mathbf{k}} \left(1 + h_{n,n'}\left(\mathbf{k}\right) c_{n,\mathbf{k};\uparrow}^{\dagger} c_{n',-\mathbf{k};\downarrow}^{\dagger}\right) |0\rangle \tag{1.42}$$

with

$$h_{n,n'}\left(\mathbf{k}\right) = \left(\hat{u}^{-1} \cdot \hat{v}\right)_{n,n'}. \tag{1.43}$$

where $\hat{u}$ and $\hat{v}$ build up part of the unitary matrix

$$\mathbf{U} = \begin{pmatrix} \hat{u}^{\dagger} & \hat{w} \\ -\hat{v}^{\dagger} & \hat{\varkappa} \end{pmatrix} \tag{1.44}$$

to diagonalize the mean field decoupled Hamiltonian in the singlet pairing channel.

As will be demonstrated in details in this thesis, the RVB mechanism reveals significantly new and rich information for the ground state properties of these two systems.

For the organic superconductor, $\kappa - (\mathrm{ET})_2 Cu_2 (CN)_3$, I find:

- D-wave superconductivity exists in the transitional region sandwiched between a metallic and a spin liquid state as onsite repulsion U increase (or, equivalently pressure decreases).
- D-wave pairing symmetry persists in the spin liquid region and gives rise to gapless excitations in momentum space. This is consistent with experimental observations in Fig. 1.8 and Ref. (45).
- In the spin liquid state, a strong spacial correlation exists between doubly occupied sites and empty sites.
- A dramatic renormalization in energy dispersion exists in the spin-liquid insulating state, which leads to distinct spacial dependence of magnetic correlation from the metallic state.

For the Shastry-Sutherland lattice which is relevant to $SrCu_2 (BO_3)_2$, I find:

- This trial wavefunction is able to describe the exact ground state of the undoped system.
- The sign of the hoppings for $SrCu_2 (BO_3)_2$ is determined by fitting the tight binding model to a first principle band structure calculation.
- The electron doping on $SrCu_2 (BO_3)_2$ is equivalent to the hole doping on a $SrCu_2 (BO_3)_2$-like system whose diagonal hopping is opposite in sign.
- Nearly homogeneous charge distribution is found for both doping cases. But the variational chemical potentials are noticeably different within a unit cell.
- Mean field calculation gives inconsistent results with the current variational study for both doping cases.

- With respect to the hole doped system,

    1. a probable phase transition exists around 2.5% doping from an insulating state (or weakly conducting state) to a plaquette d-wave pairing state.
    2. spontaneous symmetry breaking is revealed for both effective hoppings and electron pairings.
    3. enhanced inhomogeneous superconductivity is found in the plaquette d-wave pairing state as compared to the superconductivity with homogeneous d-wave pairing strength.
    4. the magnetic correlation is dramatically different for the plaquette d-wave pairing phase as compared to the parent compound.

- With respect to the electron doped system,

    1. multiple local minima close in energy are found which complicate the analysis. Yet these minima give approximately the same physical observables.
    2. effective diagonal hoppings are strongly enhanced with respect to the bare hopping parameters.
    3. the magnetic correlation is very much like that of the parent compound, implying similar localized nature to the charge carriers as in the parent compound.
    4. off diagonal long range order (ODLRO) is calculated to vanish within an error limit of 10^{-4} although the pairing gaps can be finite.
    5. the low frequency Drude weight is nonzero and thus shows a strange metallic state with strong magnetic correlation.

CHAPTER 2. Wavefunction and technical details

2.1 Construction of the RVB wavefunction

The RVB wavefunction has the generic form

$$|\Psi_{RVB}\rangle = \hat{P}\,|\Phi_0\rangle \tag{2.1}$$

where $\hat{P}$ is a projection operator to project out specific electronic configurations with different weights; $|\Phi_0\rangle$ is some many-body wavefunction defining, with differring prior weights, possible electronic configurations available for the RVB wavefunction. $|\Phi_0\rangle$ has been named the underlying wavefunction.

To help interpret it better, an example is provided below, to illustrate the relevant physics of and concerns on the projected wavefunction. A usual RVB wavefunction chosen to describe the ground state of a single band $t-J$ Hamiltonian is written as

$$\left|\Psi_{RVB}^{t-J}\right\rangle \propto \prod_i \left(1 - n_{i,\uparrow} n_{i,\downarrow}\right) |\Phi_{BCS}\rangle \tag{2.2}$$

with the normalization factor omitted. This is first introduced by P.W. Anderson in 1987 for the purpose of understanding unconventional superconductivity (14). Here the index i runs through each lattice site. $n_{i,\sigma}$ for $\sigma = \uparrow, \downarrow$ is the number operator for electrons of a specific spin on the ith lattice site. Thus $\hat{D}_i = n_{i,\uparrow} n_{i,\downarrow}$ carries values 1 to denote that a specific site is occupied by two electrons, as is called a doubly occupied site or a doublon, or 0 otherwise. $|\Phi_{BCS}\rangle$ is the BCS wavefunction which explains the conventional superconductivity. By mapping Eq. 2.2 to Eq. 2.1, it is easy to notice that in this example

$$\hat{P} = \prod_i \left(1 - n_{i,\uparrow} n_{i,\downarrow}\right), \tag{2.3}$$

called Gutzwiller Projection (72), and

$$|\Phi_0\rangle = |\Phi_{BCS}\rangle\,. \tag{2.4}$$

In different problems, $\hat{P}$ and $|\Phi_0\rangle$ can be of other forms in order to capture specific features involved there.

Why would one choose Eq. 2.2 to be the candidate for the unconventional superconductivity? This can be answered from several perspectives. First, it is required that each site should be either empty or singly occupied for a model system to be describable with a $t-J$ Hamiltonian. This is reinforced exactly by the Gutzwiller projection in Eq. 2.3 which suppresses completely electronic configurations with doubly occupied sites anywhere on the lattice, as can be seen with the term $1-n_{i,\uparrow}n_{i,\downarrow}$ involved in $\hat{P}$. To express it more succinctly and physically more meaningfully, $\hat{P}$ can be rewritten equivalently into another form

$$\hat{P} = g^{\sum_i \hat{D}_i} \tag{2.5}$$

with $g = 0^+$ for the Gutzwiller projection. The exponential, $\sum_i \hat{D}_i$, counts total number of doubly occupied sites on a given electronic configuration. Only for $\sum_i \hat{D}_i = 0$ can a configuration survive the projection. Written as Eq. 2.5, $\hat{P}$ can be easily generalized to account for different strength of onsite repulsions by treating g as a variational parameter between 0 and 1. In the limit of $g = 1$, the projection is now trivially a constant and the RVB wavefunction reduces back to the BCS wavefunction, which describes a system with very weak e-e attraction.

Second, it is expected that the trial wavefunction is able to describe phenomena involving singlet pairings and superconductivity. The straightforward way to incorporate these features into a wavefunction is to use a prototype which already has these features in it. A natural candidate is of course the BCS wavefunction. By replacing the homogeneous pairing gaps with momentum dependent ones, the BCS wavefunction can incorporate into the trial wavefunction the unconventional pairing between two electrons. These pre-existing pairings presumably survive the projection when forming the RVB wavefunction. How strong the pairings would be is determined by the variational approach to minimize the expected energy. However, superconductivity might not be as lucky. Actually whether or not superconductivity exists,

together with other physical observables, checks how well the RVB wavefunction describes the unconventional superconductivity.

On the other hand, parameters involved in the BCS wavefunction might lose their clear physical interpretation due to the projection operation acting on it in order to incorporate into the problem the necessary effects out of the strong e-e interaction. The usual parameters entering the BCS wavefunction are

$$\epsilon\left(\mathbf{k}\right), \mu, \Delta\left(\mathbf{k}\right)$$

and they are the bare electron dispersion, the chemical potential for the system, and the pairing strength between two electrons and at the same time the superconducting order parameter, respectively. In the RVB wavefunction, all of them are just variational parameters in the first place. The projection totally changes the interpretation on μ. It is now just a variational parameter but might have similar trend as the actual chemical potential. The projection also affects $\Delta\left(\mathbf{k}\right)$. Its place as an order parameter for superconductivity is removed, but its role as a pairing gap between two electrons is still largely preserved (17). The effect on $\epsilon\left(\mathbf{k}\right)$ is more subtle although it clearly doesn't represent the actual excitation spectrum of electrons any more. It, however, still acts as an effective dispersion for some quasiparticles, which means the parameters involved in the dispersion can be totally different from what is for bare ones (44).

The effect of the projection on the BCS wavefunction can be illustrated in Fig. 2.1. The real space representation of the BCS wavefunction is illustrated in the panel (a). When the Gutzwiller projection is applied onto the BCS wavefunction, all the electronic configurations with doubly occupied sites are removed from the final RVB wavefunction, as shown in the panel (b).

2.2 RVB wavefunction for $\kappa-\left(\mathbf{ET}\right)_2 Cu_2\left(CN\right)_3$ and $SrCu_2\left(BO_3\right)_2$

As has been elaborated above, the unique physical features, either contained in a system or of interest to a researcher, should be taken into account when an appropriate RVB wavefunction is chosen to describe them. This is reflected in the choice of the projection operator and the

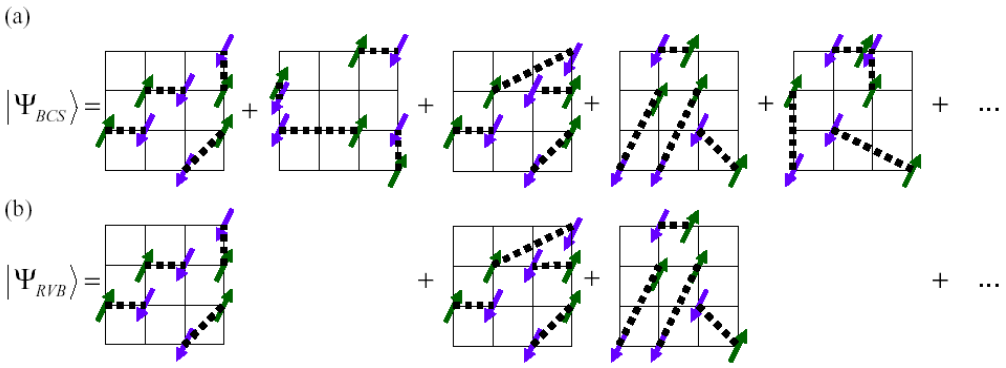

Figure 2.1 Graphic view of the BCS wavefunction in panel (a) and the RVB wavefunction after the real space projection is applied in panel (b), on a 4 by 4 lattice with 4 spin up and down electrons on it. Each bond is denoted by a thick dashed line segment, representing an electron pair of opposite spins. Each lattice denotes a specific electronic configuration with the corresponding weights omitted from the illustration. The summation signs imply a linear superposition of all these configurations.

underlying wavefunction for the projection to act on.

For $\kappa-(\mathrm{ET})_2\,Cu_2\,(CN)_3$, the experimental fact of a Mott transition caused by pressure strongly suggests that doubly occupied sites are allowed on the lattice. This means that such a term

$$\hat{P}_I = g^{\sum_i \hat{D}_i} \tag{2.6}$$

should exist in the overall projection operator, but now g acts as a variational parameter and takes value between 0 and 1. At the same time, the use of the Hubbard Hamiltonian with large U/t ratio to describe the system implies that the virtual exchange process, responsible for the $t-J$ physics and illustrated in Fig. 2.2, should play an important role here in helping electrons to move around. Ref. (73) suggests that the essence of the process is tied to the intermediate doublon-holon pair, shown in the middle of Fig. 2.2, where an empty site (holon) exists just nearby a doubly occupied site (doublon). An operator was introduced to track

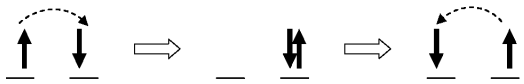

Figure 2.2 Illustration of the virtual exchange process between two electrons of opposite spins on the nearby sites. Each arrow denotes an electron of specific spin. The initial occupation is shown to the left of the figure. As the spin up electron hops to the right site, an intermediate configuration is produced having an empty and a doubly occupied site next to each other. Then, very rapidly, the spin down electron hops back to the left site and the final configuration is shown on the right of the figure. Through this process, the system develops an exchange energy of $J = 2t^2/U$.

whether this is the case for a given site,

$$\hat{\Theta}_i = n_{i\uparrow} n_{i\downarrow} \prod_{\delta} (n_{i+\delta} - n_{i+\delta,\uparrow} n_{i+\delta,\downarrow}) \tag{2.7}$$

where δ denotes all the nearest or next-nearest neighboring sites. This operator takes value 1 only when the given site is doubly occupied without any empty neighbors around it. The corresponding projection operation is then defined as

$$\hat{P}_{II} = h^{\sum_i \hat{\Theta}_i} \tag{2.8}$$

where h is called the Kaplan parameter in this thesis and assumes value between 0 and 1. Similar as the Gutzwiller parameter, the Kaplan parameter is also determined variationally and its magnitude shows how strongly a doublon and a holon are bound to each other, or equivalently, how significantly the $t - J$ physics enters the problem. It is also possible that the binding of a doublon and a holon differs along different hopping directions, which is not considered in this thesis. Then more Kaplan parameters should be introduced in that case. Combining both these considerations, the overall projection operator would be

$$\begin{aligned} \hat{P} &= \hat{P}_I \hat{P}_{II} \\ &= g^{\sum_i \hat{D}_i} h^{\sum_i \hat{\Theta}_i}. \end{aligned} \tag{2.9}$$

The choice of the underlying wavefunction is based on the knowledge of what a ground state might be on an anisotropic triangular lattice. From Ref. (74) it is known that the Hubbard model might be in a spin liquid insulating state without long-range magnetic order for $t'/t = 0.7$ and $U/t \lesssim 10 - 12t$. By considering that it readily describes a spin liquid state and a superconducting state, and noticing that the abstract lattice for organic superconductors has a simple unit cell structure, the usual single band BCS wavefunction is chosen to be the underlying wavefunction.

For $SrCu_2\left(BO_3\right)_2$, the choice of the $t-J$ Hamiltonian for the system has decided that the full Gutzwiller projection is appropriate for the variational RVB wavefunction. However, the underlying wavefunction cannot be the single band BCS wavefunction any more because of the symmetry of the SS lattice. As shown in Fig. 1.14, each unit cell contains 4 atoms and thus the relevant energy bands should be four. If no restriction is superimposed, all the possible pairings among electrons should be equally considered. These pairings can be within the same energy band, or between different energy bands. This implies that the wavefunctional form proposed in Ref. (9) is not appropriate any more because all the pairings there are just within the same energy band. Thus, this is why a multiband pairing BCS wavefunction is worked out in this thesis. It is still a BCS type because the concept of two electrons to form a Cooper pair is used.

2.3 Multiband pairing BCS wavefunction

Multiband pairing effects have been investigated in the past (75), yet explicit expressions for the pairing amplitude and the BCS wavefunction have, to the best of my knowledge, not been formulated. In this thesis, they are derived and the derivation is shown in great detail in Appendix A and B. A brief account on the derivation is given below, followed by the real space projection of this wavefunction.

Derivation of the pairing amplitude between two electrons Let us consider a problem on a lattice with N unit cells and m atoms within a unit cell. The following shortcut

notation is used for a given site

$$i \equiv (\mathbf{R}_i, r_i)\,,$$

where $\mathbf{R}_i, r_i$ denote the coordinate of a unit cell and the atomic index within that unit cell respectively. The $t-J$ Hamiltonian, without the three-site hopping term, can then be written as

$$\hat{H}^{t-J} = -\sum_{\langle i,j\rangle,\sigma} t_{i,j}\tilde{c}^{\dagger}_{i,\sigma}\tilde{c}_{j,\sigma} + \sum_{\langle i,j\rangle} J_{ij}\left(\hat{\mathbf{S}}_i\cdot\hat{\mathbf{S}}_j - \frac{n_i n_j}{4}\right) \tag{2.10}$$

where $\tilde{c}_{i,\sigma} = c_{i,\sigma}\left(1-n_{i,\bar{\sigma}}\right)$, $\langle i,j\rangle$ denotes all possible hoppings on the lattice while the exchange interaction J_{ij} and the spin operator $\hat{\mathbf{S}}$ follow the definitions in Eq. 1.18 and 1.19.

The BCS wavefunction can be equally understood as the ground state of a mean field fermionic Hamiltonian decomposed in the pairing channel. To apply this idea, the interaction part, which is the second part in Eq. 2.10, is re-expressed as

$$\hat{\mathbf{S}}_i\cdot\hat{\mathbf{S}}_j - \frac{n_i n_j}{4} = -\frac{1}{2}\tilde{\mathcal{B}}^{\dagger}_{i,j}\tilde{\mathcal{B}}_{i,j} \tag{2.11}$$

with

$$\tilde{\mathcal{B}}_{i,j} = \tilde{c}_{i;\downarrow}\tilde{c}_{j;\uparrow} - \tilde{c}_{i;\uparrow}\tilde{c}_{j;\downarrow} \tag{2.12}$$

the annihilation operator for a spin singlet between site i and j. From the special arrangement of $\mathcal{B}$ on the right side of Eq. 2.11, it is not surprising why the $t-J$ Hamiltonian can be used to obtain the BCS type wavefunction. The crucial component, spin singlet operator, is readily contained in this interaction.

By introducing the mean field pairing

$$\Delta_{ij} = \left\langle\tilde{\mathcal{B}}_{i,j}\right\rangle, \tag{2.13}$$

which is now just a complex parameter, ignoring constant terms in the energy and dropping the restriction of single occupation on each site, the $t-J$ Hamiltonian is transformed into a solvable mean field Hamiltonian

$$\hat{H}^{mf} = -\sum_{\langle i,j\rangle,\sigma} t_{ij}c^{\dagger}_{i,\sigma}c_{j,\sigma} - \frac{1}{2}\sum_{\langle i,j\rangle} J_{ij}\left(\Delta^{*}_{ij}\mathcal{B}_{i,j} + \mathcal{B}^{\dagger}_{i,j}\Delta_{ij}\right). \tag{2.14}$$

By applying the Fourier transformation onto the fermionic operators

$$c_{r,\mathbf{k};\sigma} = \frac{1}{\sqrt{N}} \sum_{\mathbf{R}} e^{-i\mathbf{k}\cdot\mathbf{R}} c_{r,\mathbf{R};\sigma}, \tag{2.15}$$

Eq. 2.14 can be written equivalently in momentum space as

$$\hat{H}^{mf} = -\sum_{\mathbf{k}} \begin{pmatrix} \left(\psi_{\uparrow}^{T}(\mathbf{k})\right)^{\dagger} & \psi_{\downarrow}(-\mathbf{k}) \end{pmatrix} \begin{pmatrix} T(\mathbf{k}) & D(\mathbf{k}) \\ D^{\dagger}(\mathbf{k}) & -T(\mathbf{k}) \end{pmatrix} \begin{pmatrix} \psi_{\uparrow}^{T}(\mathbf{k}) \\ \psi_{\downarrow}^{\dagger}(-\mathbf{k}) \end{pmatrix} \tag{2.16}$$

where $T^{\dagger}(\mathbf{k}) = T(\mathbf{k})$ and $\psi_{\sigma}(\mathbf{k}) = \begin{pmatrix} c_{1,\mathbf{k};\sigma} & c_{2,\mathbf{k};\sigma} & \ldots & c_{m,\mathbf{k};\sigma} \end{pmatrix}$.

Let us suppose that there exists a $2m \times 2m$ unitary matrix

$$\mathbf{U}^{\dagger} = \begin{pmatrix} \hat{u}^{\dagger} & \hat{w} \\ -\hat{v}^{\dagger} & \hat{\varkappa} \end{pmatrix}, \tag{2.17}$$

with $\hat{u}, \hat{v}, \hat{w}$ and $\hat{\varkappa}$ block matrices of size $m \times m$ and satisfying $\hat{v} \cdot \hat{\varkappa} = \hat{u} \cdot \hat{w}$, to diagonalize the mean field matrix

$$\hat{H} = \begin{pmatrix} T(\mathbf{k}) & D(\mathbf{k}) \\ D^{\dagger}(\mathbf{k}) & -T(\mathbf{k}) \end{pmatrix} \tag{2.18}$$

by $\mathbf{U}^{\dagger}\hat{H}\mathbf{U}$. This would give rise to $2m$ eigenvalues which come out in positive and negative pairs (61). Without losing generality, it can be assumed that the first four eigenvalues are positive, then the annihilation operator for quasiparticles of $\hat{H}^{mf}$ can be written as

$$z_i(\mathbf{k}) = \sum_{j=1}^{m} \left[\hat{u}_{ij} c_{j,\mathbf{k};\uparrow} - \hat{v}_{ij} c_{j,-\mathbf{k};\downarrow}^{\dagger}\right]. \tag{2.19}$$

Meanwhile, the following ersatz is introduced for the ground state wavefunction of $\hat{H}^{mf}$

$$\left|\Phi_{BCS}^{M}\right\rangle \propto e^{\sum_{n_1,n_2,\mathbf{k}} h_{n_1,n_2}(\mathbf{k}) c_{n_1,\mathbf{k};\uparrow}^{\dagger} c_{n_2,-\mathbf{k};\downarrow}^{\dagger}} \left|0\right\rangle. \tag{2.20}$$

Here $h_{n_1,n_2}(\mathbf{k})$ denotes the pairing amplitude for two electrons with opposite spins located at $(\mathbf{k}, n_1)$ and $(-\mathbf{k}, n_2)$. n_1, n_2 can either be band indices or site indices. To let Eq. 2.20 be the ground state wavefunction, it is required that

$$z_i(\mathbf{k}) \left|\Phi_{BCS}\right\rangle = 0 \tag{2.21}$$

for $i = 1, 2, ...m$. Finally the analytic form for the pairing amplitudes are determined to be

$$\varrho\left(\mathbf{k}\right) = \hat{u}^{-1} \cdot \hat{v} \tag{2.22}$$

where $\left[\varrho\left(\mathbf{k}\right)\right]_{n_1,n_2} = h_{n_1,n_2}\left(\mathbf{k}\right)$. As a comment, from the above expression $\varrho\left(\mathbf{k}\right)$ is invariant with respect to different phase conventions chosen to define z_i.

Real space projection of the BCS wavefunction It is necessary to project $\left|\Phi_{BCS}^{M}\right\rangle$ into the real space representation. This projection is carried out in two steps. The first step is to project out a fixed number of particles out of the BCS wavefunction. This is done by noticing that Eq. 2.20 can be rewritten as

$$\left|\Phi_{BCS}^{M}\right\rangle \propto e^{\sum_{n_1,n_2,\mathbf{k}} h_{n_1,n_2}(\mathbf{k}) c^{\dagger}_{n_1,\mathbf{k};\uparrow} c^{\dagger}_{n_2,-\mathbf{k};\downarrow}} \left|0\right\rangle \tag{2.23}$$

$$= \sum_{N=0}^{\infty} \frac{1}{N!} \left(\sum_{n_1,n_2,\mathbf{k}} h_{n_1,n_2}\left(\mathbf{k}\right) c^{\dagger}_{n_1,\mathbf{k};\uparrow} c^{\dagger}_{n_2,-\mathbf{k};\downarrow} \right)^{N} \left|0\right\rangle \tag{2.24}$$

and thus $2N$ particles in the system is just

$$P_N \left|\Phi_{BCS}\right\rangle \propto \left(\sum_{n_1,n_2,\mathbf{k}} h_{n_1,n_2}\left(\mathbf{k}\right) c^{\dagger}_{n_1,\mathbf{k};\uparrow} c^{\dagger}_{n_2,-\mathbf{k};\downarrow} \right)^{N} \left|0\right\rangle . \tag{2.25}$$

The second step is to project the above expression into specific real space occupation with equal number of spin up and down electrons. Generically any electronic configurations in real space can be denoted as

$$\left|\vec{r}_{\uparrow}, \vec{r}_{\downarrow}\right\rangle = \left|\mathbf{r}_{1;\uparrow}, \mathbf{r}_{2;\uparrow}, ...\mathbf{r}_{N;\uparrow}, \mathbf{r}_{N+1;\downarrow}, \mathbf{r}_{N+2;\downarrow}, ...\mathbf{r}_{2N;\downarrow}\right\rangle . \tag{2.26}$$

The inner product of the BCS wavefunction with $\left|\vec{r}_{\uparrow}, \vec{r}_{\downarrow}\right\rangle$, which automatically projects out $2N$ particles of equal number of spin up and down, can be written as

$$\left\langle \vec{r}_{\uparrow}, \vec{r}_{\downarrow} | \Phi_{BCS} \right\rangle \propto \left\langle 0 \right| \left(\prod_{i} c_{\mathbf{r}_{i;\uparrow},\uparrow} c_{\mathbf{r}_{i;\downarrow},\downarrow} \right) \prod_{n_1,n_2,\mathbf{k}} \left(1 + h_{n_1,n_2}\left(\mathbf{k}\right) c^{\dagger}_{n_1,\mathbf{k};\uparrow} c^{\dagger}_{n_2,-\mathbf{k};\downarrow} \right) \left|0\right\rangle , \tag{2.27}$$

by noticing that

$$e^{h_{n_1,n_2}(\mathbf{k}) c^{\dagger}_{n_1,\mathbf{k};\uparrow} c^{\dagger}_{n_2,-\mathbf{k};\downarrow}} = 1 + h_{n_1,n_2}\left(\mathbf{k}\right) c^{\dagger}_{n_1,\mathbf{k};\uparrow} c^{\dagger}_{n_2,-\mathbf{k};\downarrow} \tag{2.28}$$

due to the fermionic nature of $c^{\dagger}$. The later manipulation and simplification is rather tedious and are included in Appendix B. The final conclusion is that the $2N$ particle projection can be expressed in a determinant form

$$\langle \vec{r}_{\uparrow}, \vec{r}_{\downarrow} | \Phi_{BCS} \rangle \propto \begin{vmatrix} \phi_{v_{N+1}}^{v_1}(\mathbf{R}_1 - \mathbf{R}_{N+1}) & \phi_{v_{N+2}}^{v_1}(\mathbf{R}_1 - \mathbf{R}_{N+2}) & & \\ \phi_{v_{N+1}}^{v_2}(\mathbf{R}_2 - \mathbf{R}_{N+1}) & \phi_{v_{N+2}}^{v_2}(\mathbf{R}_2 - \mathbf{R}_{N+2}) & & \\ & & \ldots & \\ & & & \phi_{v_{2N}}^{v_N}(\mathbf{R}_N - \mathbf{R}_{2N}) \end{vmatrix} \tag{2.29}$$

where $\phi_{v_j}^{v_i}(\mathbf{R}_i - \mathbf{R}_j)$ is the pairing wavefunction between two electrons with opposite spins at site i and j, and is defined as

$$\phi_{v_j}^{v_i}(\mathbf{R}_i - \mathbf{R}_j) = \sum_{\mathbf{k}} h_{v_i, v_j}(\mathbf{k})\, e^{-i\mathbf{k}\cdot(\mathbf{R}_i - \mathbf{R}_j)}. \tag{2.30}$$

2.4 Reformulation of physical expectation into statistical language

The physical quantities observed in the trial wavefunction, $|\Psi_{RVB}\rangle$, are defined as an expectation

$$\left\langle \hat{O} \right\rangle = \frac{\langle \Psi_{RVB} | \hat{O} | \Psi_{RVB} \rangle}{\langle \Psi_{RVB} | \Psi_{RVB} \rangle} \tag{2.31}$$

where $\hat{O}$ is the corresponding physical operator. The denominator is introduced to normalize the trial wavefunction. Here is a list of the relevant physical observables involved in this thesis work. The corresponding physical operators are also provided, together with a brief discussion if necessary.

- Energy expectation, E, with

$$\hat{O} = \hat{H}. \tag{2.32}$$

- Charge density, n_i, with

$$\hat{O} = \sum_{\sigma} c_{i,\sigma}^{\dagger} c_{i,\sigma}. \tag{2.33}$$

- Magnetic correlation, χ_{ij}, between two lattice sites, i and j. The corresponding operator is defined as

$$\hat{O}_{ij} = S_i^{+} S_j^{-} \tag{2.34}$$

with S^+ and S^- defined in Eq. 1.28 and 1.29. By plugging in Eq. 1.19, the corresponding fermionic representation for these two spin operators is checked to be

$$S^+ = c^\dagger_\uparrow c_\downarrow \tag{2.35}$$

$$S^- = c^\dagger_\downarrow c_\uparrow. \tag{2.36}$$

To the spin liquid state considered in this thesis, there is a special property for χ_{ij} due to $SU(2)$ rotational invariance in the spin space, that is,

$$\left\langle S^+_i S^-_j \right\rangle = 2 \left\langle S^z_i S^z_j \right\rangle. \tag{2.37}$$

- Off diagonal long range order (ODLRO), ψ_s, defined as

$$|\psi_s|^2 = \lim_{|\mathbf{R}_i - \mathbf{R}_j| \to \infty} \left\langle \mathcal{B}^\dagger_{i,i+\delta} \mathcal{B}_{j,j+\gamma} \right\rangle \tag{2.38}$$

where $\mathcal{B}_{i,i+\delta}$ is defined in Eq. 2.12 and δ, γ are some constant vectors along which singlet pairs are constructed. It is actually a correlation function for two spin singlets separated faraway in distance. It is understood that a nonvanishing ODLRO implies the Meisner effect and the flux quantization (76)(77), and is thus sufficient to indicate the onset of superconductivity.

- Low frequency Drude weight, D_{low}, with

$$\begin{aligned}\hat{O} = &\sum_{\mathbf{r},\mathbf{r}';\sigma} t_{\mathbf{r}\mathbf{r}'} \left[h_{\mathbf{r},\bar{\sigma}} c^\dagger_{\mathbf{r},\sigma} c_{\mathbf{r}',\sigma} h_{\mathbf{r}'\bar{\sigma}} \right] \left(\mathbf{r}_x - \mathbf{r}'_x \right)^2 \\ &+ \sum_{\mathbf{r},\mathbf{r}',\mathbf{R},\sigma,\sigma'} \frac{t_{\mathbf{r},\mathbf{R}} t_{\mathbf{R},\mathbf{r}'}}{U} \left[h_{\mathbf{r},\bar{\sigma}} c^\dagger_{\mathbf{r},\sigma} c_{\mathbf{R},\sigma} n_{\mathbf{R},\bar{\sigma}} c^\dagger_{\mathbf{R},\sigma'} c_{\mathbf{r}',\sigma'} h_{\mathbf{r}',\bar{\sigma}'} \right] \left(\mathbf{r}_x - \mathbf{r}'_x \right)^2.\end{aligned} \tag{2.39}$$

where $h_{\mathbf{r},\bar{\sigma}}, n_{\mathbf{R},\bar{\sigma}}$ follow notations in Eq. 1.14 and $\mathbf{r}_x$ is the x component of a lattice site vector $\mathbf{r}$ (17). This expression is specifically related to the $t-J$ Hamiltonian with the three-site hopping term included in Eq. 1.14. The derivation is included in Ref. (17) and is omitted here.

- Total charge fluctuation, δn_{ij}, on site i and j. It cannot be expressed by a single operator but is related to charge density operators. It is defined as

$$\delta n_{ij} = \sqrt{\left\langle \left(\sum_\sigma \left(c^+_{i,\sigma} c_{i,\sigma} + c^+_{j,\sigma} c_{j,\sigma} \right) \right)^2 \right\rangle - \left\langle \sum_\sigma \left(c^+_{i,\sigma} c_{i,\sigma} + c^+_{j,\sigma} c_{j,\sigma} \right) \right\rangle^2} \tag{2.40}$$

and gives useful information on superconducting phase fluctuation (78).

The expectation for a physical quantity defined in Eq. 2.31 looks most simple, however, its evaluation is definitely nontrivial. The difficulty lies in the fact that the inner products involved in the expectation cannot be evaluated directly. The whole expression has to be rewritten as a summation over local quantities under a specific distribution function. Monte Carlo (MC) simulation can then be used to finish carrying out the rest of the evaluation. This is done as follows:

The complete closure relationship in the Fock space with N spin-up and N spin-down electrons on a lattice is written as

$$I = \sum_{\substack{\{r_{1;\uparrow}, r_{2;\uparrow}, ...r_{N;\uparrow}\} \\ \{r_{1;\downarrow}, r_{2;\downarrow}, ...r_{N;\downarrow}\}}} |r_{1;\uparrow}, r_{2;\uparrow}, ...r_{N;\uparrow}, r_{1;\downarrow}, r_{2;\downarrow}, ...r_{N;\downarrow}\rangle \langle r_{1;\uparrow}, r_{2;\uparrow}, ...r_{N;\uparrow}, r_{1;\downarrow}, r_{2;\downarrow}, ...r_{N;\downarrow}| \quad (2.41)$$

where $r_{i;\uparrow(\downarrow)}$ denotes the lattice site on which the ith spin-up(down) electron sits, or in short notation

$$I = \sum_{\{\vec{r}_\uparrow, \vec{r}_\downarrow\}} |\vec{r}_\uparrow, \vec{r}_\downarrow\rangle \langle \vec{r}_\uparrow, \vec{r}_\downarrow| \quad (2.42)$$

with $\vec{r}_\sigma \equiv r_{1;\sigma}, r_{2;\sigma}, ...r_{N;\sigma}$. By inserting it into Eq. 2.31, I obtain

$$\left\langle \hat{O} \right\rangle = \sum_{\{\vec{r}_\uparrow, \vec{r}_\downarrow\}} \rho\left(\vec{r}_\uparrow, \vec{r}_\downarrow\right) \left(\sum_{\{\vec{r}'_\uparrow, \vec{r}'_\downarrow\}} \langle \vec{r}_\uparrow, \vec{r}_\downarrow| \hat{O} \left|\vec{r}'_\uparrow, \vec{r}'_\downarrow\right\rangle \frac{\left\langle \vec{r}'_\uparrow, \vec{r}'_\downarrow | \Psi_{RVB} \right\rangle}{\langle \vec{r}_\uparrow, \vec{r}_\downarrow | \Psi_{RVB} \rangle} \right) \quad (2.43)$$

with

$$\rho\left(\vec{r}_\uparrow, \vec{r}_\downarrow\right) = \frac{\left|\langle \vec{r}_\uparrow, \vec{r}_\downarrow | \Psi_{RVB} \rangle\right|^2}{\sum_{\{\vec{r}^*_\uparrow, \vec{r}^*_\downarrow\}} \left| \left\langle \vec{r}^*_\uparrow, \vec{r}^*_\downarrow | \Psi_{RVB} \right\rangle \right|^2}. \quad (2.44)$$

This can now be interpreted as a statistical mechanics problem. The expectation value is the mean of the expression bracketed in Eq. 2.43 and the corresponding distribution function is $\rho\left(\vec{r}_\uparrow, \vec{r}_\downarrow\right)$ in a $2N$ dimensional discrete finite phase space. After reformulating Eq. 2.31 into Eq. 2.43, it is a standard practice to use the MC simulation to evaluate the mean. The method used in generating the Markov chain is with the Metropolis algorithm, to be discussed in the next paragraph.

2.5 Twice application of the Metropolis algorithm

A very efficient method to generate an intended distribution in a multi-dimensional space is to use the Markov Chain Monte Carlo (MCMC) method (79). A Markov chain, x_i, is a random array,

$$x_i = (r_{i,1}, r_{i,2}, ...r_{i,k})$$

where k is chosen to be the dimensionality of the phase space where the distribution function is to be generated. By varying each coordinate, $r_{i,j}$, of the array within its allowed range, x_i represents different points in the phase space. The Markov property should be satisfied for x_i and is expressed mathematically as

$$\Pr(x_{n+1}|x_n, x_{n-1}, ...x_1) = \Pr(x_{n+1}|x_n) \tag{2.45}$$

where $\Pr(x|...)$ denotes the conditional probability of x given something else. In simple language, the Markov property requires that a new element in the Markov chain should only depend on its one-time-step-ahead neighboring element. A relevant example of a Markov chain is given in Appendix C.

With several other enhanced conditions, the Markov chain is able to generate the expected distribution in the long run independent of the starting element (79)(80). One way to satisfy these conditions is to use the Metropolis algorithm, invented by Nicholas Metropolis in 1953 (81) and later improved by W.K. Hastings in 1970 (82). (More details on the Hastings-improved Metropolis algorithm is given in Appendix D.) The idea is closely related to the principle of detailed balance in statistical mechanics,

$$p(x_1) W(x_2|x_1) = p(x_2) W(x_1|x_2) \tag{2.46}$$

where $p(x)$ is the equilibrium distribution function and $W(x_2|x_1)$ denotes the transitional probability from state x_1 to x_2. The Metropolis algorithm makes use of this idea backwards. It introduces a specifically chosen $W(x_2|x_1)$ to fulfil the detailed balance mentioned above,

$$W(x_2|x_1) = \min\left(\frac{p(x_2)}{p(x_1)}, 1\right). \tag{2.47}$$

and then $p(x)$ is generated asymptotically as the expected stationary distribution. Practically, there are subtleties in how to implement this algorithm most efficiently. These are related to how to mix states most efficiently, or in other words, to make the Markov chain as mobile as possible in the phase space.

One subtlety is the choice of a pseudo-random number generator to update the Markov chain. There are different random number generators to use, for example, linear congruential generator, multiple recursive congruential generator and Mersenne twister (83)(84); and there are articles on how to check a random number generator (85). What I choose are $ran3$ from Numerical Recipe (86) and $mt19937$ invented by Makoto Matsumoto and Takuji Nishimura in 1997 (87). Among all the random number generators, $mt19937$ is most intriguing to me. Any random number sequence it generates has a very long periodicity in repeating itself, very well-controlled equidistribution which means negligible serial correlation in its output sequence, and what's more, all of these properties can be rigorously proved (87). Another subtlety is how to choose the step size for each coordinate of the random array, x_i, as would also be addressed in the following sections.

Metropolis algorithm in evaluating physical observable Because the physical observables can be reexpressed as the mean of a function over some distribution function as in Eq. 2.43, the Metropolis algorithm can be used to help generating a sequence of samples which satisfy the distribution function re-written here for easy reference

$$\rho\left(\vec{r}_{\uparrow},\vec{r}_{\downarrow}\right)=\frac{\left|\langle\vec{r}_{\uparrow},\vec{r}_{\downarrow}|\Psi_{RVB}\rangle\right|^{2}}{\sum_{\{\vec{r}_{\uparrow}^{*},\vec{r}_{\downarrow}^{*}\}}\left|\left\langle\vec{r}_{\uparrow}^{*},\vec{r}_{\downarrow}^{*}|\Psi_{RVB}\right\rangle\right|^{2}}. \tag{2.48}$$

Let us suppose a spin up electron is chosen to update to another location and thus $|\vec{r}_{\uparrow}\rangle\rightarrow\left|\vec{r}_{\uparrow}^{\prime}\right\rangle$, the transitional probability $W_{|\vec{r}_{\uparrow}\rangle\rightarrow|\vec{r}_{\uparrow}^{\prime}\rangle}$ for this update is defined as

$$W_{|\vec{r}_{\uparrow}\rangle\rightarrow|\vec{r}_{\uparrow}^{\prime}\rangle}=\min\left(\left|\frac{\left\langle\vec{r}_{\uparrow}^{\prime},\vec{r}_{\downarrow}|\Psi_{RVB}\right\rangle}{\langle\vec{r}_{\uparrow},\vec{r}_{\downarrow}|\Psi_{RVB}\rangle}\right|^{2},1\right) \tag{2.49}$$

by following Eq. 2.47. To attain the highest efficiency in generating the distribution function, it is important to choose an appropriate scheme to update an electron to a new lattice site.

The following scheme is used for this purpose

- For 10% of chances, directly hop the electron to a randomly chosen empty site.
- Otherwise, try the electron with direct or spin-flip move to a randomly chosen nearest or next nearest neighbor site.

In implementing the update of, say, a spin up electron to a new lattice site, $W_{|\vec{r}_\uparrow\rangle\rightarrow|\vec{r}'_\uparrow\rangle}$ needs to be calculated which involves the evaluation of the ratio $\left\langle \vec{r}'_\uparrow, \vec{r}_\downarrow|\Psi_{RVB}\right\rangle / \langle \vec{r}_\uparrow, \vec{r}_\downarrow|\Psi_{RVB}\rangle$. Usually this is related to evaluating $\left\langle \vec{r}'_\uparrow, \vec{r}_\downarrow|\Phi_{BCS}\right\rangle / \langle \vec{r}_\uparrow, \vec{r}_\downarrow|\Phi_{BCS}\rangle$ because the projection operators usually commute with the particle number operators. The general expression for $\langle \vec{r}_\uparrow, \vec{r}_\downarrow|\Phi_{BCS}\rangle$ is a determinant, as given in Eq. 2.29 and shown in Appendix B. Generally the direct evaluation of a determinant is time-consuming. However, the calculation of $\left\langle \vec{r}'_\uparrow, \vec{r}_\downarrow|\Phi_{BCS}\right\rangle$ can be very much simplified by noticing that it calculates a new determinant whose square matrix is altered by only one column or one row as compared to $\langle \vec{r}_\uparrow, \vec{r}_\downarrow|\Phi_{BCS}\rangle$ of one time step ahead (88). By using the information from $\langle \vec{r}_\uparrow, \vec{r}_\downarrow|\Phi_{BCS}\rangle$ and applying the matrix algebra, an iterative expression for $\left\langle \vec{r}'_\uparrow, \vec{r}_\downarrow|\Phi_{BCS}\right\rangle$ can be obtained which expediates the evaluation very much. The necessary explanation is provided in Appendix E.

As the procedure continues, a sequence of $\{\vec{r}_\uparrow, \vec{r}_\downarrow\}$ is generated. And the local physical observable,

$$\begin{aligned} O(t_i) &= O\left(\vec{r}_\uparrow(t_i), \vec{r}_\downarrow(t_i)\right) \\ &= \sum_{\{\vec{r}'_\uparrow, \vec{r}'_\downarrow\}} \left\langle \vec{r}_\uparrow(t_i), \vec{r}_\downarrow(t_i)\right| \hat{O} \left|\vec{r}'_\uparrow, \vec{r}'_\downarrow\right\rangle \frac{\left\langle \vec{r}'_\uparrow, \vec{r}'_\downarrow|\Psi_{RVB}\right\rangle}{\left\langle \vec{r}_\uparrow(t_i), \vec{r}_\downarrow(t_i)|\Psi_{RVB}\right\rangle}, \end{aligned} \tag{2.50}$$

called an observation, is calculated accordingly to each member of the sequence. These observations can be consecutively partitioned into bins with each of them containing thousands of observations. Let N denote number of observations in each bin. Each bin is then averaged to give rise to a sample,

$$O_i = \frac{1}{N}\sum_{k=1}^{N} O(t_{i+k}) \tag{2.51}$$

which satisfies a Gaussian distribution centered at the expected mean of the physical observable, $\left\langle \hat{O}\right\rangle$, according to the Central Limit Theorem (CLT). Finally, $\left\langle \hat{O}\right\rangle$ is estimated by the

average over all the samples,

$$\bar{O} = \frac{1}{n_b} \sum_{i=1}^{n_b} O_i \tag{2.52}$$

and the standard error for $\bar{O}$ is calculated as

$$Var_{\bar{O}} = \frac{1}{n_b \left(n_b - 1\right)} \left(\sum_{i=1}^{n_b} O_i^2 - n_b^2 \left(\bar{O}\right)^2 \right) \propto \frac{1}{\sqrt{n_b N}} \tag{2.53}$$

where n_b denotes number of bins, or samples.

The RVB trial wavefunction depends on the specific boundary conditions chosen for the problem. This usually causes a finite size effect and should not be important if the lattice size is big enough. But for a finite lattice size, inappropriate boundary conditions might introduce fake effects into the result. The boundary conditions involved in this thesis can either be periodic or antiperiodic. The choice of which boundary conditions used is in principle not restricted, as long as it is used consistently throughout the simulation and it doesn't affect any energy evaluation. However, the periodic boundary conditions applied to both directions are often energetically favored and, meanwhile, it maintains the symmetry of the variational parameters on both axes. On the other hand, antiperiodic boundary conditions might introduce additional complexity in analyzing the simulation results. All these issues are summarized in Appendix F.

Metropolis algorithm in global minimum search As a variational approach, the parameters introduced in the RVB wavefunction have to be optimized to give lowest expected energy, E. To help with this, simulated annealing algorithm is used by defining an artificial distribution function as

$$p\left(\vec{u}\right) = Ce^{-\frac{E(\vec{u})}{k_T}} \tag{2.54}$$

where $\vec{u} = (u_1, u_2, ..., u_m)$ is the set containing all the variational parameters, C is some normalization constant and k_T is called the virtual temperature (89). k_T is solely an auxiliary parameter introduced to help locate the functional minimum. The algorithm mimics the annealing process by starting with a very high temperature and reducing it very slowly. For a fixed temperature, lower energy corresponds to higher probability density. With a gradually

reducing temperature, more weights would be accumulated around the global energy minimum and parameters are thus most likely to fall within that region of the phase space. The rationale for the Metropolis algorithm to be applicable in looking for the energy minimum is due to the fact that no information would be missing if the complete distribution can be accurately generated. The use of the simulated annealing algorithm is to focus the movement of the Markov chain around lower energy region to improve efficiency.

To carry out the Metropolis algorithm on the distribution function defined in Eq. 2.54, the relevant transitional probability $W_{\vec{u}\to\vec{u}'}$ is defined as

$$W_{\vec{u}\to\vec{u}'} = \min\left(e^{-\frac{E(\vec{u}')-E(\vec{u})}{k_T}}, 1\right) \tag{2.55}$$

with $\vec{u}' = \{u_1', u_2', ..u_i'...\}$ an updated parameter set as compared to $\vec{u}$. As is easy to see from this expression, k_T plays another role of defining a typical energy difference to be accessible in a single update.

The step size is another parameter worth considering. It is legitimate to update any number of variational parameters at the same time. But usually only one parameter is updated. So $\vec{u}'$ can be written as

$$\begin{aligned}\vec{u}' &= \left\{u_1', u_2', ..u_i'...\right\} \\ &= \{u_1, u_2, ..u_i + \delta u_i...\} \\ &= \vec{u} + \{0, 0, ..\delta u_i...\}\,.\end{aligned} \tag{2.56}$$

If one chooses fixed steps for all the parameters, then

$$\delta u_i = \epsilon\delta_i \tag{2.57}$$

where $\epsilon \in [-1, 1]$ is a uniform random number and δ_i is a constant step for the ith dimension. However, this is not the most efficient method available to generate a distribution by using a fixed step for each dimension. This can be easily understood by noticing that the energy landscape can be completely irregular and unpredictable in the whole phase space. Even at the same location of the phase space, reduced k_T intuitively requires a smaller step size to give rise to smaller energy difference between two consecutive updates. To treat this problem,

I developed a simple yet very powerful scheme to update steps continuously anywhere and anytime in the phase space.

To begin with, acceptance ratio, κ, is introduced as

$$\kappa = \frac{n_a}{n_t} \tag{2.58}$$

where n_a is the number of accepted updates and n_t is the number of total trial updates. The idea is: the step size should be reduced when the actual acceptance ratio, κ_a, is less than the pre-assumed one, κ_f; or increased if otherwise. How much the step size should be adjusted is suggested by a model calculation. The model assumes a quadratic dispersion,

$$E(x) = ax^2, \tag{2.59}$$

which is a valid assumption when the simulation is around a local minimum, and repeats the update many times by sitting initially at $x = 0$. The theoretical acceptance ratio for a given step size A with respect to the transitional probability defined in Eq. 2.55 is evaluated to be

$$\kappa = \frac{\int_0^{A^*} e^{-x^2} dx}{A^*} = g(A^*) \tag{2.60}$$

where $A^* = A\sqrt{\frac{a}{k_T}}$. Thus the new step size, A_{new}, should satisfy

$$\frac{A_{new}}{A} = \frac{g^{-1}(\kappa_f)}{g^{-1}(\kappa_a)} \tag{2.61}$$

in order to maintain a fixed acceptance ratio.

There are many practical considerations with respect to the above scheme and other issues involved in the simulated annealing algorithm, in order to make it run stabler and more efficiently. They are summarized in Appendix G.

CHAPTER 3. Results for $\kappa-(\mathbf{ET})_2 Cu_2 (CN)_3$

As a member of organic superconductors, $\kappa-(\mathrm{ET})_2 Cu_2 (CN)_3$ shares many common features of this class. For example, it has a half-filled energy band; it undergoes a phase transition from a Mott insulating state to an unconventional superconducting state by tuning pressure; it has strong e-e interaction and is described by a Hubbard Hamiltonian

$$\hat{H} = -t \sum_{\langle i,j\rangle,\sigma} \left(c^{\dagger}_{i,\sigma} c_{j,\sigma} + h.c. \right) - t' \sum_{\langle k,l\rangle,\sigma} \left(c^{\dagger}_{k,\sigma} c_{l,\sigma} + h.c. \right) + U \sum_{i} n_{i,\uparrow} n_{i,\downarrow} \tag{3.1}$$

on an anisotropic triangular lattice shown in Fig. 1.11. The detailed explanation to the notations involved is given after Eq. 1.22. What make this material special is that the insulating state is a spin liquid state caused by the strong geometric frustration. This is likely caused by the fact that $t'/t \approx 1$ for this material. The goal of the study is to see whether the strongly correlated physics, which dominates the phase transition and the unconventional superconductivity, can be explained reasonably well by a RVB wavefunction where strong e-e interaction is incorporated through projections proposed under physical consideration. The wavefunction can be explicitly written down as

$$|\Psi_{RVB}\rangle = g^{\sum_i \hat{D}_i} h^{\sum_i \hat{\Theta}_i} \left|\Phi^S_{BCS}\right\rangle \tag{3.2}$$

explained in detail in the last chapter. The single band BCS wavefunction is defined as

$$\left|\Phi^S_{BCS}\right\rangle \propto e^{-\sum_{\mathbf{k}} \phi_{\mathbf{k}} c^{\dagger}_{\mathbf{k},\uparrow} c^{\dagger}_{-\mathbf{k},\downarrow}} |0\rangle \tag{3.3}$$

where

$$\phi_{\mathbf{k}} = \frac{\tilde{\Delta}_{\mathbf{k}}}{E_{\mathbf{k}} + (\tilde{\epsilon}_{\mathbf{k}} - \tilde{\mu})} \tag{3.4}$$

with

$$E_{\mathbf{k}} = \sqrt{(\tilde{\epsilon}_{\mathbf{k}} - \tilde{\mu})^2 + \tilde{\Delta}^2_{\mathbf{k}}}. \tag{3.5}$$

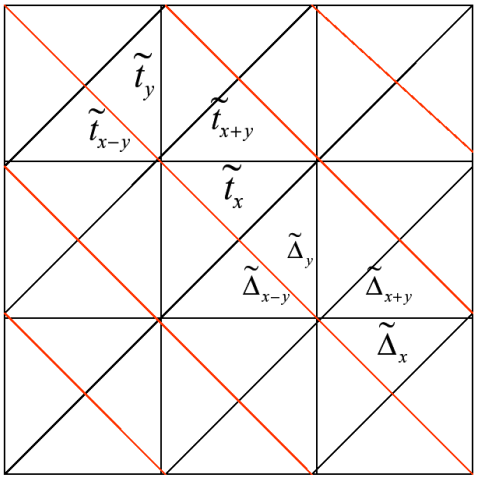

Figure 3.1 Illustration of definition of the variational parameters, including effective hoppings and pairings, on the square lattice. Red lines (from the upper left corner to the lower right corner) correspond to the additional effective diagonal hoppings not existing in the bare dispersion.

The explicit functional forms for $\tilde{\epsilon}_{\mathbf{k}}$ and $\tilde{\Delta}_{\mathbf{k}}$ are

$$\tilde{\epsilon}_{\mathbf{k}} = \tilde{t}_x \cos k_x + \tilde{t}_y \cos k_y + \tilde{t}_{x+y} \cos(k_x + k_y) + \tilde{t}_{x-y} \cos(k_x - k_y)$$
$$\tilde{\Delta}_{\mathbf{k}} = \tilde{\Delta}_x \cos k_x + \tilde{\Delta}_y \cos k_y + \tilde{\Delta}_{x+y} \cos(k_x + k_y) + \tilde{\Delta}_{x-y} \cos(k_x - k_y).$$

The variational parameters for the simulation are the different effective hoppings,

$$\tilde{t}_x, \tilde{t}_{x+y}, \tilde{t}_{x-y}, \tilde{t}_y,$$

a variational chemical potential, different projection parameters,

$$\tilde{\mu}, g, h$$

and different pairing gaps

$$\tilde{\Delta}_x, \tilde{\Delta}_{x+y}, \tilde{\Delta}_{x-y}, \tilde{\Delta}_y$$

along the bonds where effective hoppings are defined. Fig. 3.1 illustrates on the lattice the definition of some of the above variational parameters.

All the simulations are done on a lattice of size at least 12×12 with antiperiodic boundary condition on $\hat{x}$ axis and periodic boundary condition on $\hat{y}$ axis to avoid singularities caused by vanishing pairings at specific momentum points. The bare parameters take values as $t = -1.0, t'/t = 0.7$ with $U/|t|$ ranging from 5.0 to 12.0. For this material, the experimentally determined t'/t is slightly different from the value used here. But this difference is checked not to be of vital importance by other calculations using different methods (50)(53). In the rest of this chapter, U is used exchangeable with $U/|t|$ except for cases where they might cause confusion. By noticing that the pairing amplitude, $\phi_{\mathbf{k}}$, only depends on the ratio of the variational parameters in $\tilde{\Delta}_{\mathbf{k}}, \tilde{\epsilon}_{\mathbf{k}}$ and $\tilde{\mu}$, one of these parameters can be fixed without losing generality. Actually $\tilde{t}_x$ is fixed to be 1.0.

Implication of g and h Due to the nature of the local projection operators, $\hat{D}_i$ and $\hat{\Theta}_i$, it is reasonable to think that the Gutzwiller parameter, g, controls the average number of doubly occupied sites (doublon), while the Kaplan parameter, h, reflects how strong a doubly occupied site would be tied to an empty site (holon) as its nearest or next nearest neighbor. The U dependence of these two parameters are shown in Fig. 3.2, and the behavior of holons, or equally doublons, can be roughly seen from the two curves.

For small U, holons move around nearly freely except for limited restriction from the double occupancy on each site. This is reflected by a small g and an h value close to 1. As U increases, the number of doubly occupied sites is gradually reduced, which is physically expected and is shown by a declining g. The binding between doulons and holons is gradually enhanced, shown by a reduced h value away from 1. As U reaches beyond $U_{c_1} \approx 8.5$, a sudden drop in h indicates the onset of a much stronger correlation between doublons and holons, while a continuous g shows a nearly unchanged number of doublons. This is suggestive of a new phase developing out of the original one. The discontinuity in h implies the change in phases is first order although h itself cannot be thought of as the order parameter simply because it doesn't drop to zero while an order parameter does so. By looking at Fig. 3.3, it can be seen that finite pairing and ODLRO develop around U_{c_1}. This indicates that the possible phase transition is between a metallic phase and a superconducting phase.

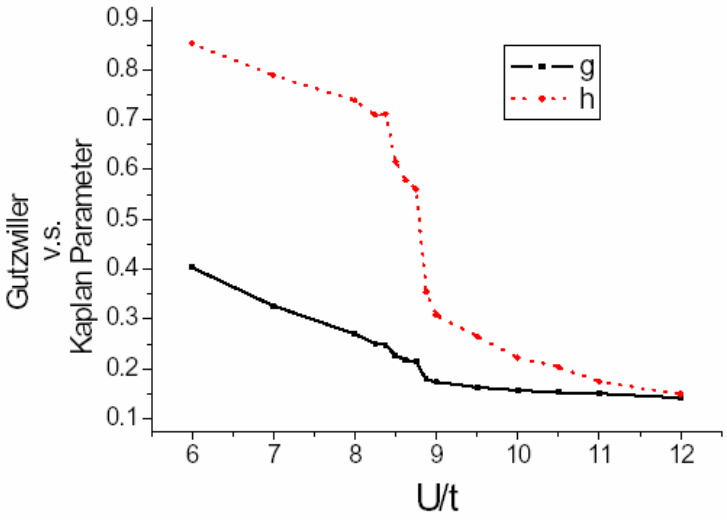

Figure 3.2 Gutzwiller parameter g and Kaplan parameter h vs. onsite repulsion U. It is easy to notice that both these parameters reduce suddenly at $U_{c_1} \approx 8.5$ and $U_{c_2} \approx 9.0$, suggesting possible phase transitions.

Within a very narrow region of U, both h and g experience another sudden drop around $U_{c_2} \approx 9$. The reduction in g is unexpected if the same phase is assumed across $U \approx 9$ because the change in U, the direct control over double occupancy, is continuous. This new phase is featured by a sudden suppression of doublons and meanwhile, it seems to be dominated strongly by the $t - J$ physics. Thus, direct electron movement is responsible for less of the charge mobility, as is implied by the enormous reduction in h around U_{c_2} and its continuous reduction as U increases. The nature of this phase should be the same as that of $U \to \infty$ for both g and h curves are continuous in U as shown in Fig. 3.2. It is a straightforward fact that the phase in the large U limit is insulating and this is also the case here.

Phase diagram revealed by the ODLRO Both the optimal pairing and the ODLRO are obtained as a function of U and are shown in Fig. 3.3. The optimal pairing automatically chooses a spacial symmetry of the d-wave type with $\tilde{\Delta}_x = -\tilde{\Delta}_y$. The U dependence of the pairing strength is shown in the upper panel of the figure. The ODLRO follows the definition

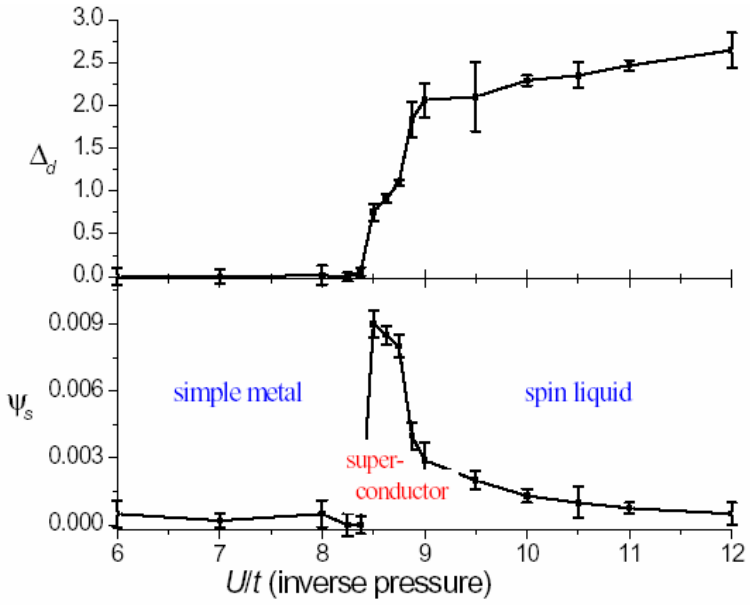

Figure 3.3 The upper panel shows pairing strength vs. onsite repulsion U. The optimal pairing pattern is d-wave, $\tilde{\Delta}_x = -\tilde{\Delta}_y$. For $U < U_{c_1}$, $\tilde{\Delta}$ basically vanishes. As U increases, $\tilde{\Delta}$ increases rapidly and then is followed by a slow increase. The lower panel shows the ODLRO calculated w.r.t the optimal pairings shown above. The persistence of the ODLRO around U_{c_1} suggests a superconducting state. For $U < U_{c_1}$, a vanishing ODLRO with zero pairing strength assumes a metallic state; for $U \gg U_{c_2}$, slow decay of the ODLRO is believed to be an artifact of the trial wavefunction (90). Combined with finite pairing, a spin liquid state is otherwise expected for large U.

in Eq. 2.38 with $\delta = \gamma$ between nearest neighbor sites along the $\hat{y}$ axis. Its U dependence is shown in the lower panel of the figure.

For $U < U_{c_1}$, the ODLRO vanishes as expected physically because the pairing also vanishes in the system. The BCS wavefunction then reduces to describe filling of a free Fermi sea. Without this projection, it describes a metallic state because the energy band is not fully filled. Even with the projection, the nature of the RVB state is still expected to be metallic because of the finite values of g and h. Finite g suggests that electrons can still move around the lattice without major restrictions because doubly occupied sites are allowed to a large

extent. An h close to 1 clearly implies that there is little resistance coming from doublon holon binding against the electron movement. However, a metallic state is unintuitive to me since $U/|t|$ is not small at all.

When U is between U_{c_1} and U_{c_2}, finite pairing develops very rapidly, as is shown in the upper panel of Fig. 3.3. This implies that some effective attraction begins to emerge between nearest neighboring electrons along $\hat{x}$ and $\hat{y}$ axes although the only physical interaction in the Hamiltonian is the repulsion between two electrons on the same site. The effective attraction is also supported by the corresponding sudden reduction in the parameter h at the two critical U values, implying enhanced binding between two electrons. However, the effective attraction cannot be simply ascribed to the competition between t and U because the optimization gives no pairing along the diagonal direction although the bare hopping exists there. With a finite pairing at $U = U_{c_1}$, a finite ODLRO appears suddenly manifesting the onset of superconductivity. This is an alternative signal of the potential first order phase transition besides the discontinuity in h. The maximal ODLRO appears for some intermediate $\tilde{\Delta}$ value but not for an even larger magnitude. This is in contradiction to the conclusion from the mean field theory where $\tilde{\Delta}$ is at the same time the superconducting order parameter of the system. This fact shows the strong e-e interaction built in the RVB wavefunction totally changes the physics of the system. Why a larger pairing between two electrons would not necessarily give rise to stronger superconductivity has partially been understood by the increasing difficulty in moving an electron around as U increases. Thus the additional requirement of moving two pairs of electrons phase coherently is much harder to satisfy (17). However, this effect should not be the only one causing the sudden drop of the ODLRO at $U = U_{c_2}$ because the change of the ODLRO would then be smooth in the U dependence. The other possible cause might be the reorganization of electrons in the system around U_{c_2}, as is reflected by a sudden enhancement in $\tilde{\Delta}$ and sudden reduction in h and g. For $U \gg U_{c_2}$, the state can be regarded as a fragile superconductor because of the slowly decaying tiny ODLRO. But this has been argued to be an artifact of the current trial wavefunction because the movement of an electron cannot be fully suppressed unless g is exactly zero (90). Thus this phase is usually interpreted to be a

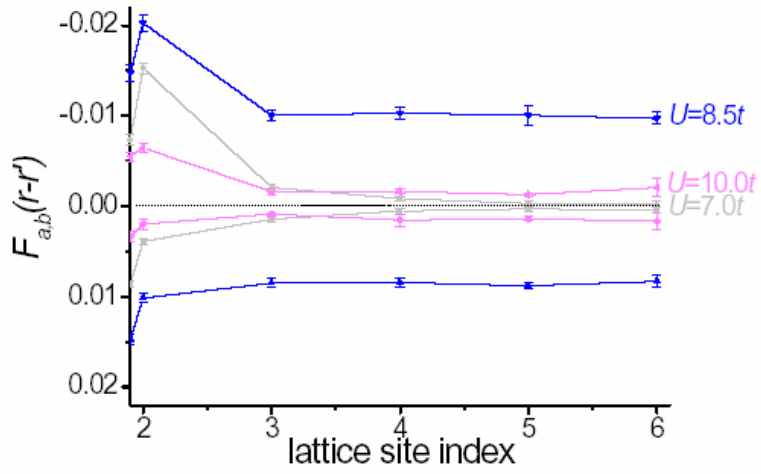

Figure 3.4 Spacial dependence of the ODLRO to three U values. The ODLRO is stabilized within three lattice constants for all Us.

spin liquid insulating state in order to be consistent with the conclusion coming from the large U limit of the current Hamiltonian.

The spacial dependence of the singlet singlet correlation function, $F_{ab}\left(\mathbf{R}-\mathbf{R}'\right)$, is defined as

$$F_{ab}\left(\mathbf{R}-\mathbf{R}'\right)=\left\langle \mathcal{B}^{\dagger}_{\mathbf{R},\mathbf{R}+a}\mathcal{B}_{\mathbf{R}',\mathbf{R}'+b}\right\rangle \tag{3.6}$$

following the notations from Eq. 2.38. The ODLRO, ψ_s, is related to $F_{ab}\left(\mathbf{R}-\mathbf{R}'\right)$ by

$$\lim_{|\mathbf{R}-\mathbf{R}'|\to\infty} F_{ab}\left(\mathbf{R}-\mathbf{R}'\right)=|\psi_s|^2\,. \tag{3.7}$$

The lattice dependence of $F_{ab}\left(\mathbf{R}-\mathbf{R}'\right)$ is shown in Fig. 3.4. From the plot, it is easy to see that $F_{ab}\left(\mathbf{R}-\mathbf{R}'\right)$ quickly stabilizes when the two singlets are separated by 3 lattice constants.

Soon after this work, the experimental phase diagram was measured on this material and is presented in Fig. 1.10. By noticing that increasing pressure corresponds to effectively decreasing U, and comparing the calculated phase diagram here to the experimental one at $T\to 0$K, an obvious distinction can be detected that the sharp transition in the experiment is, however, between the spin-liquid and unconventional superconducting state. The possible reason to

this inconsistency has been identified in the work of T. Watanabe, H. Yokoyama et al (50). Motivated by the current work, they introduced an additional Kaplan parameter to account for possibly different doublon-holon bindings along both lateral and diagonal directions. They then got qualitatively consistent results with the experiment.

Renormalization on the electron dispersion and its effect As has been mentioned above, the strong e-e interaction manifests itself in distinguishing the pairing, $\tilde{\Delta}$, from the superconducting order parameter. It also shows itself in choosing the effective fermionic dispersion, $\tilde{\epsilon}_{\mathbf{k}}$, to be different from the bare one as finite pairing develops. This renormalization effect lies mainly in the effective diagonal hoppings and is shown in Fig. 3.5. To appreciate it, please bear in mind that the bare diagonal hoppings are fixed at

$$t_{x+y} = 0.7t,\ t_{x-y} = 0.0t$$

for all U values. This renormalization effect seems to be a generic feature of materials with strong e-e interaction as well as geometric frustration, as is also hinted in Ref. (91) in a DMFT calculation and in Ref. (92) in a VMC calculation.

For $U < U_{c_1}$, the BCS wavefunction reduces to describing the free band filling, because of the vanishing pairing. Correspondingly, the effective diagonal hoppings take the same values as the bare ones as they should do. However, they are not uniquely determined. Actually, the total energy shows a flat dispersion on these hoppings, which is represented by the huge error bar in the figure. This has been checked and is due to the finite size effect. When pairing vanishes, what is crucial for the wavefunction are the occupied momentum points whose energies are lower. It is not hard to see that there exists different dispersion relationships which are able to give the same set of occupied momenta and thus result in the same trial wavefunction.

For $U > U_{c_2}$, the physics lies mainly in the strongly reduced effective diagonal hopping and consequentially a spacially more symmetric charge distribution, $n_{\mathbf{k}}$. The bare diagonal hopping, t_{x+y}, is required to have a much smaller value in its variational counterpart, $\tilde{t}_{x+y}$, by energy minimization, while the other diagonal hopping, $\tilde{t}_{x-y}$, develops a comparable magnitude as $\tilde{t}_{x+y}$. The resulting $\tilde{\epsilon}_{\mathbf{k}}$ is presumably related to the effective dispersion of the quasi-particles

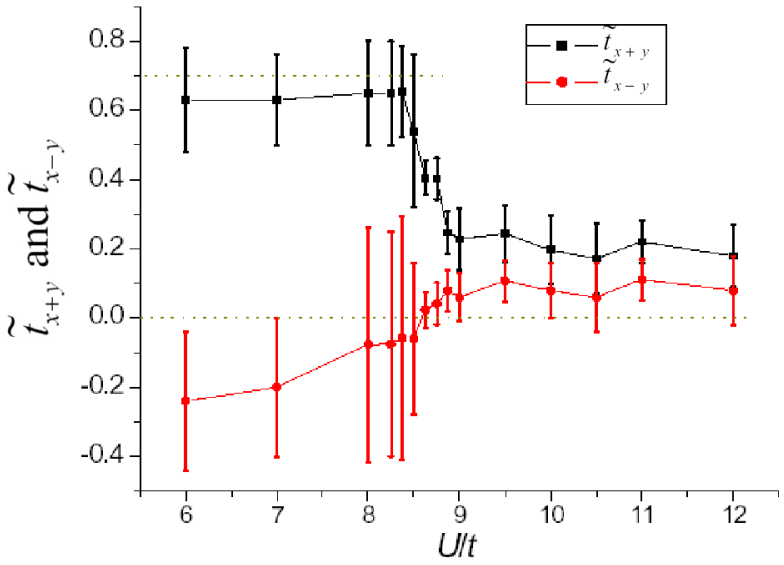

Figure 3.5 Effective diagonal hoppings, $\tilde{t}_{x+y}$ and $\tilde{t}_{x-y}$, along $\hat{x}+\hat{y}$ and $\hat{x}-\hat{y}$ directions respectively, vs. onsite repulsion U. For $U < U_{c_1}$, there is strong degeneracy in these two effective hoppings, an artifact due to the finite size effect in case of vanishing gaps; for $U > U_{c_2}$, $\tilde{t}_{x+y}$ is strongly reduced as compared to its original hopping while $\tilde{t}_{x-y}$ is now comparable to $\tilde{t}_{x+y}$ in magnitude. As an outcome, the renormalized excitation spectrum is more symmetric than the original one in momentum space.

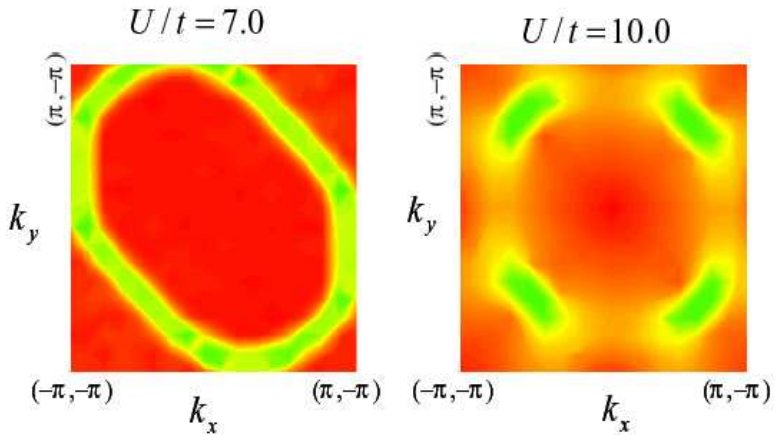

Figure 3.6 Contour plot of $|\nabla_{\mathbf{k}} n(\mathbf{k})|$ for $U = 7$ and $U = 10$. The strongly renormalized dispersion for $U = 10$, together with the strong d-wave pairing, generates a nearly fourfold symmetric structure with the largest gradients along diagonal directions even though the bare hoppings differ completely along these directions. Red color shows small gradient while green color shows larger gradients.

aroused in the system due to the strong e-e interaction. But this interpretation is not rigorous because the resulting BCS wavefunction still has to undergo the projection operation to incorporate the strong e-e interaction. The physically more meaningful quantity is the charge distribution in momentum space, whose gradient is shown in the right plot of Fig. 3.6. The maximum gradients are located at the four nearly rotationally symmetric locations in green. These locations can be predicted by the quasiparticle filling of $\tilde{\epsilon}_{\mathbf{k}}$ together with the vanishing d-wave pairings along the diagonal directions, which is exactly the way how the same thing is predicted within a weak interacting theory. As a comparison, the maximum gradients of $n_{\mathbf{k}}$ coincide with the Fermi surface of the bare dispersion for $U < U_{c_1}$, which is shown in the left plot of the figure. It is in this sense that $\tilde{\epsilon}_{\mathbf{k}}$ is interpreted as the effective dispersion relationship for quasi-particles. At the same time, this coincidence also assumes that the projection doesn't change significantly the charge distribution defined by the BCS wavefunction in momentum space.

When U increases from U_{c_1} to U_{c_2}, the effective diagonal hoppings change continuously to connect the two limits. Meanwhile, the energy minimum is more and more well-defined, illustrated in Fig. 3.5 with reduced error bars, as the pairing becomes finite. The interest here lies mainly in the superconductivity maximized around $U = U_{c_1}$. The natural question to ask is the role played by the geometric frustration on the superconductivity. This is made possible by interpreting $\tilde{\epsilon}_{\mathbf{k}}$ to be the effective dispersion which determines most directly how much geometric frustration is actually introduced into the system. The full answer to this question could be possible if ψ_s were calculated for different values of $\tilde{t}_{x+y}$ and $\tilde{t}_{x-y}$ while other parameters were kept fixed, which was, however, not done in this thesis work. What have been considered are the wavefunctions optimized in energy at different U values. The analysis is thus complicated by different amount of geometric frustration together with different e-e interaction. However, it is likely that in the current problem $\tilde{\epsilon}_{\mathbf{k}}$ with reduced geometric frustration favors the formation of the d-wave pairing, which is directly related with superconductivity.

The renormalized dispersion, $\tilde{\epsilon}_{\mathbf{k}}$, also affects the magnetic correlation, χ_{ij}. The spacial dependence of χ_{ij} is shown in Fig. 3.7 for an unrenormalized dispersion at $U = 7$ and for a strongly renormalized one at $U = 11$. The comparison indicates two major differences, one is in the spacial dependence and the other in the contrast between the two diagonal directions. The spacial dependence of the magnetic correlation for $U = 11$, which corresponds to a spin liquid state, is antiferromagnetic and decays much slower than that for $U = 7$. And, χ between nearest neighbor sites is much more enhanced for larger U, as is clearly shown in the inset of the figure. On the other hand, χ along the two diagonal directions are nearly the same for $U = 11$, while they are clearly different for $U = 7$: the χ along $\hat{x} - \hat{y}$, where no bare hopping exists, constantly vanishes but the χ along $\hat{x} + \hat{y}$ is finite and is of the same sign as the χs along the lateral directions. All these are consistent with what is implied by $\tilde{\epsilon}_{\mathbf{k}}$. For $U = 11$, $\tilde{\epsilon}_{\mathbf{k}}$ has nearly the same effective hopping magnitude in both diagonal directions. At the same time, the weakened frustration contained in the effective dispersion, $\tilde{t}_{x+y}/\tilde{t} \approx 0.2$, enhances the magnetic correlation to be of wider range. Both of these two facts, together with the d-wave pairing, give a reasonable interpretation of site dependence of χ in the right panel of

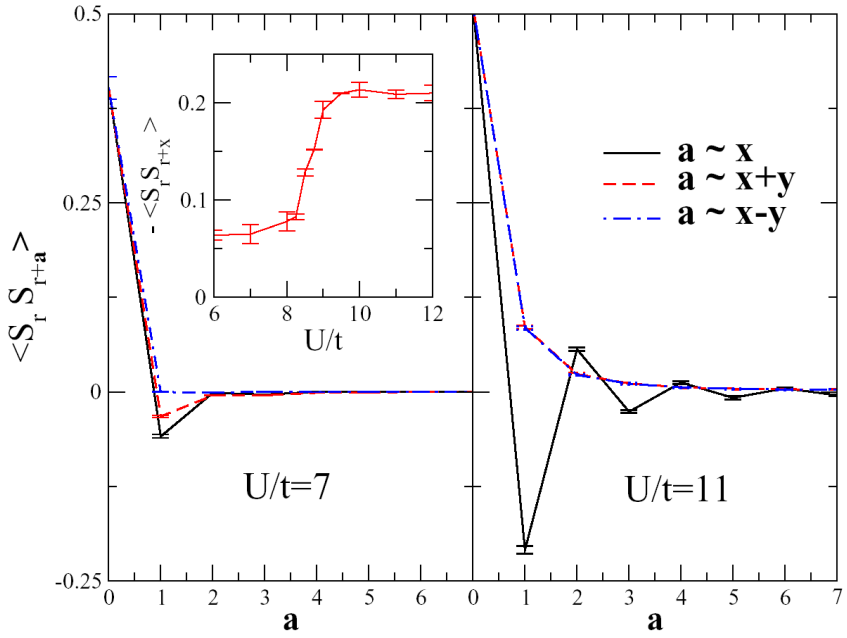

Figure 3.7 Spacial dependence of $\chi_{0,a} = 2\langle S_0^z S_a^z \rangle$ on two U values. For $U = 11$, the magnetic correlation, χ, along the two diagonal directions become indistinguishable even though the bare hoppings are very different. For $U = 7$, the two χs can easily be distinguished. The inset shows U dependence of $\chi_{i,i+x}$, magnetic correlation between two nearest neighboring sites along $\hat{x}$ axis.

Fig. 3.7. For $U = 7$, $\tilde{\epsilon}_{\mathbf{k}}$ is identically the same as $\epsilon_{\mathbf{k}}$. This means that there is strong geometric frustration along $\hat{x} + \hat{y}$, which qualitatively changes the nature of the magnetic correlation to be antiferromagnetic on that direction, while no interaction exists along $\hat{x} - \hat{y}$ and thus no magnetic correlation should be expected.

Comment on the finite size effect In order to see how seriously the optimal parameters would depend on the lattice size, optimal d-wave pairing strengths have been calculated for different lattice sizes. The results are shown in Fig. 3.8 for both $U = 9.5$ with finite pairing and $U = 7.0$ with vanishing pairing. The conventional $1/L$ extrapolation carried out for $U = 9.5$ shows that the pairing does not vanish for infinite lattice size.

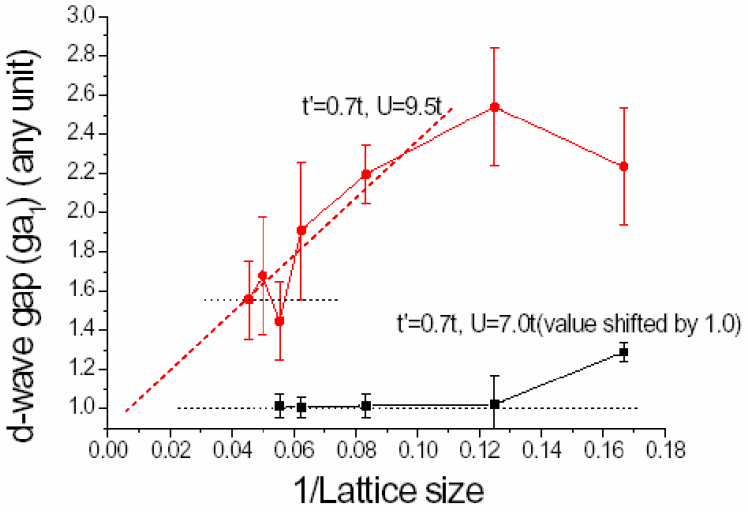

Figure 3.8 Size dependence of optimal d-wave pairing on lattices up to 22×22 for $U = 9.5$ and 7.0. To show both dependences in the same figure, $\tilde{\Delta}$ for $U = 7.0$ is shifted upward by unit magnitude. Extrapolation to larger systems for $U = 9.5$ supports a finite pairing even on an infinitely large lattice.

CHAPTER 4. Results for Shastry-Sutherland(SS) lattice

For $SrCu_2\left(BO_3\right)_2$, the major physics lies in the $CuBO_3$ layers separated from each other by Sr^{2+} layers. The spins are carried by Cu^{2+} ions and they form a lattice structure which is topologically equivalent to the Shastry-Sutherland (SS) lattice shown in Fig. 1.14. The Hamiltonian defined on it is the Heisenberg Hamiltonian in Eq. 1.23, or

$$\hat{H}_h = \sum_{\langle i,j \rangle} J \hat{\mathbf{S}}_i \cdot \hat{\mathbf{S}}_j + \sum_{\langle l,m \rangle} J' \hat{\mathbf{S}}_l \cdot \hat{\mathbf{S}}_m. \tag{4.1}$$

The most inspiring feature of the SS lattice is that it has the same exactly solvable ground state for $J'/J \geq 2$, the spin singlet dimer state (62). It is a product of singlets along specific diagonal directions and is expressed in Eq. 1.24, or

$$|\Psi\rangle = \prod_{\langle l,m \rangle} \frac{1}{\sqrt{2}} \left(|l, \uparrow; m, \downarrow\rangle - |l, \downarrow; m, \uparrow\rangle \right). \tag{4.2}$$

Further theoretical studies have extended the threshold J'/J to be around 1.428 beyond which the singlet dimer state is the ground state. Meanwhile, the relevant J'/J for $SrCu_2\left(BO_3\right)_2$ is 1.5741 (56).

In this chapter, the doping effect of this material is investigated. It is an out-of-plane doping where Sr^{2+} ions are replaced by other ions. It includes both electron and hole doping and is described by the $t-J$ Hamiltonian in Eq. 1.38, or

$$\begin{aligned} \hat{H} = & \sum_{\langle i,j \rangle, \sigma} t \tilde{c}^{\dagger}_{i,\sigma} \tilde{c}_{j,\sigma} + \sum_{\langle l,m \rangle, \sigma} t' \tilde{c}^{\dagger}_{l,\sigma} \tilde{c}_{m,\sigma} \\ & + \sum_{\langle i,j \rangle} J \left(\hat{\mathbf{S}}_i \cdot \hat{\mathbf{S}}_j - \frac{n_i n_j}{4} \right) + \sum_{\langle l,m \rangle} J' \left(\hat{\mathbf{S}}_l \cdot \hat{\mathbf{S}}_m - \frac{n_l n_m}{4} \right) \end{aligned} \tag{4.3}$$

where

$$J = \frac{4t^2}{U} \text{ and } J' = \frac{4t'^2}{U}.$$

The three-site hopping terms are not explicitly written out in the above expression but are included in the study. Experiments so far have determined J and J', but not the relative sign between t and t'. To answer this question, a first principle calculation is carried out on the band structure of this material and a tight binding model is fitted to it. This fit reveals that $t' > 0$, while the sign of t is of irrelevance to this material. Due to the fact that only one electron is allowed on each lattice site, only hole doping can be treated directly in the simulation. How to treat electron doping is not so straightforward. The necessary consideration will be provided in the relevant sections.

The RVB wavefunction used for this Hamiltonian has been explained in Chapter 2. It is a fully projected multiband BCS wavefunction, explicitly written out as

$$|\Psi_{RVB}\rangle = \prod_i \left(1 - n_{i,\uparrow} n_{i,\downarrow}\right) \left|\Phi_{BCS}^M\right\rangle \tag{4.4}$$

where

$$\left|\Phi_{BCS}^M\right\rangle = \prod_{\mathbf{k},n_1,n_2} \left(1 + h_{n_1,n_2}\left(\mathbf{k}\right) c_{\mathbf{k};n_1,\uparrow}^\dagger c_{-\mathbf{k};n_2,\downarrow}^\dagger\right) |0\rangle \,. \tag{4.5}$$

The relevant notations have been explained in Eq. 2.20. All the variational parameters are contained in $h_{n_1,n_2}\left(\mathbf{k}\right)$. But unlike $\phi_{\mathbf{k}}$ in the single band BCS wavefunction, there is no explicit relationship for $h_{n_1,n_2}\left(\mathbf{k}\right)$ to depend on these parameters. The matrix expression is provided in Eq. 2.22. Although more variational parameters can be included in the study, only the following parameters are considered here: the six effective hoppings

$$\tilde{t}_{x_1}, \tilde{t}_{x_2}, \tilde{t}_{x+y}, \tilde{t}_{x-y}, \tilde{t}_{y_1}, \tilde{t}_{y_2},$$

the four variational chemical potentials

$$\tilde{\mu}_0, \tilde{\mu}_1, \tilde{\mu}_2, \tilde{\mu}_3$$

and the six pairing gaps

$$\tilde{\Delta}_{x_1}, \tilde{\Delta}_{x_2}, \tilde{\Delta}_{x+y}, \tilde{\Delta}_{x-y}, \tilde{\Delta}_{y_1}, \tilde{\Delta}_{y_2}.$$

along the bonds where exchange interactions are available. They are supposed to include the minimal number of variational parameters which are needed to describe this problem. The definitions are illustrated in Fig. 4.1

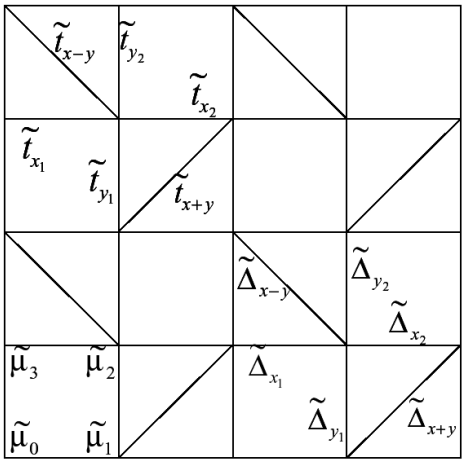

Figure 4.1 Illustration of definition of all the variational parameters used in the multiband BCS wavefunction on the SS lattice. $\tilde{\mu}s$ are variational chemical potentials on each atom in the unit cell, while $\tilde{t}$ and $\tilde{\Delta}$ are variational hoppings and pairings between nearby atoms.

All the simulations are done on the 12×12 lattice with antiperiodic boundary condition along $\hat{x}$ axis and periodic boundary condition along $\hat{y}$ axis, if not stated otherwise. However, unlike the organic superconductor, this choice of boundary condition is, generally speaking, not necessary because the concerns on the singularity for the pairing amplitude in the single band BCS wavefunction doesn't exist on the SS lattice. What's more, it introduces confusion into the data analysis. But all these are noted only at the end of the study. Explicit calculations checked that these boundary conditions didn't change the major conclusions, but the optimal value might be changed for each variational parameter. The bare parameters involved in the Hamiltonian take values as $t = -1.0$, $J = 0.3\,|t|$ and $\alpha = t'/t = \pm 1.25$. These values were taken from Ref. (61) before the band structure calculation was carried out. Especially $J = 0.3\,|t|$, which is the typical relationship for high T_c cuprates. On the other hand, experiments have determined that J is around 54K, while fitting band dispersion sets t to be around 1043K. Thus $J = 0.05t$ seems to be a more realistic relationship for $SrCu_2\,(BO_3)_2$. However, several checks have been carried out and the major conclusions don't seem to be sensitive to J/t ratios.

Secondly, the variational parameters involved in the multiband BCS wavefunction also have one degree of freedom based on the similar reasonings as in the single band BCS wavefunction. This is fixed by taking $\tilde{t}_{x_1}$ to be the energy unit for all the other variational parameters.

There are some general conclusions which apply to both doping cases

$$\tilde{\mu}_0 = \tilde{\mu}_2 \text{ and } \tilde{\mu}_1 = \tilde{\mu}_3$$
$$\tilde{t}_{x_1} = \tilde{t}_{y_2} \text{ and } \tilde{t}_{x_2} = \tilde{t}_{y_1}.$$

The relationships for $\tilde{\mu}_i$ are physically easy to understand. Actually $\tilde{\mu}_0$ and $\tilde{\mu}_2$, or $\tilde{\mu}_1$ and $\tilde{\mu}_3$, are connected by a diagonal bond if the point group symmetry of the SS lattice is considered. The relationships for $\tilde{t}$ are nontrivial. This strongly suggests a spontaneous symmetry breaking in effective hoppings on the lattice. On the other hand, existence of multiple energy minima make the analysis of the simulation results more difficult, especially to the electron doped case.

Besides the variational study, a slave-boson mean field treatment is also applied to the same problem. A mean field theory is usually considered inferior as compared to a variational study using a carefully chosen trial wavefunction. The same situation is also expected here because the single occupation restriction on each site is hard to impose analytically. However, the mean field study can still give useful insights into the problem in different aspects. Actually something which is quite uncommon for this problem is found by comparing the conclusions from both approaches.

4.1 Exact ground state for the half-filled SS lattice

The real space projection of the BCS wavefunction shows that it is a linear superposition of products of singlets between different sites on the lattice. The singlet dimer state is one of those products and is thus contained in the BCS wavefunction as a special subset. It is, however, totally nontrivial that a simple full Gutzwiller projection is able to exactly filter out this special term. But this *is* the case in the current problem. Part of the reason can be ascribed to the use of $\left|\Phi^M_{BCS}\right\rangle$ where the very symmetry of the SS lattice is fully implemented. As a contrast, the Gutzwiller projected single band BCS wavefunction is unable to give the

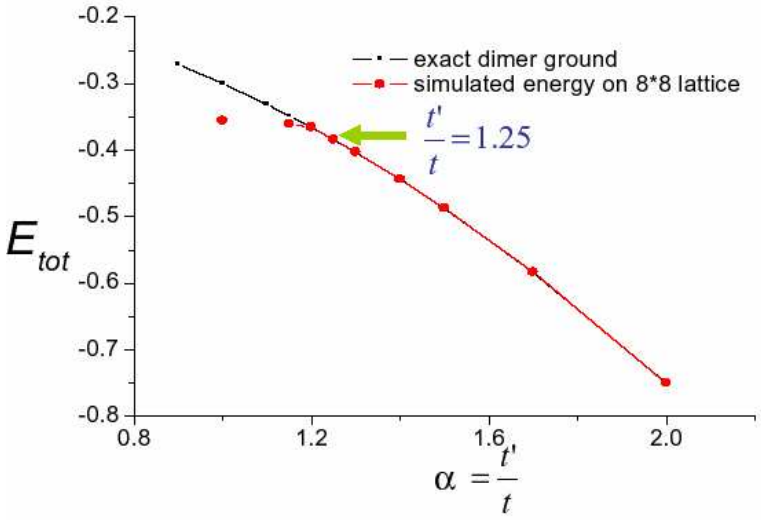

Figure 4.2 α dependence of the simulated total energy, $E_{\rm tot}$, on the 8×8 lattice and the energy for the theoretical single dimer state, $E^{SS}_{\rm dimer}$, for the half-filled SS lattice. The curve for $E_{\rm tot}$ is shown in red big dots while the curve for $E^{SS}_{\rm dimer}$ in black small dots. The lines connecting the dots are just guidance to eye. For the α range where the two curves overlap with each other, the agreement is within an error of 10^{-7}. By the way, additional terms $n_i n_j/4$ are added to the Heisenberg Hamiltonian in Eq. 4.1. This doesn't change the physics for the half-filled case yet the total energy of the dimer ground state is shifted downward by $\frac{N}{2}\left(\frac{J'}{4}+J\right)$.

required singlet dimer state.

In Fig. 4.2 shows the fact that the exact ground state is obtained in the current RVB wavefunction. There, the simulated energy, $E_{\rm tot}$, and the theoretical energy for the singlet dimer state, $E^{SS}_{\rm dimer}$, are both presented against $\alpha = |t'/t|$. From the plot, it is clear that $E_{\rm tot}$ agrees perfectly with $E^{SS}_{\rm dimer}$ for $\alpha > 1.2$ within an error higher than 10^{-7}. Although the evaluation is done on an 8×8 lattice, the agreement is checked and found to be lattice size independent, which is expected from the localized feature of the singlet dimer state. Physically this agreement reveals that the current RVB trial wavefunction is capable of capturing the correct physics related to the complicated unit cell structure of the SS lattice. However for

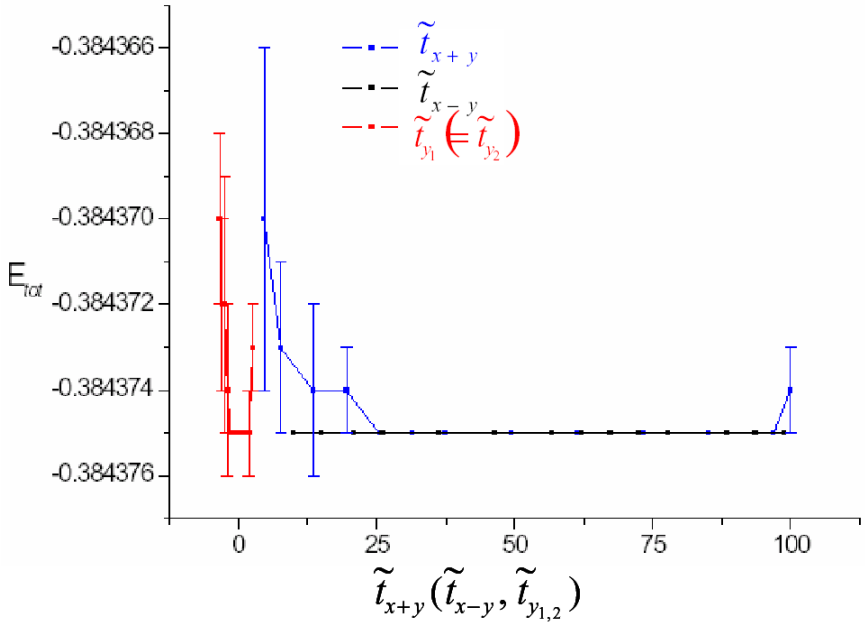

Figure 4.3 Illustration of strong degeneracy on effective hoppings for $\alpha = t'/t = 1.25$. All the energies are calculated with other parameters not fully optimized when each effective hopping changes its value. $\tilde{t}_{x_1} = \tilde{t}_{x_2}$ is chosen to be the energy unit. The red curve on the left shows $\tilde{t}_y$ dependence of the simulated energy. The blue and black curves on the right show $\tilde{t}_{x+y}$, $\tilde{t}_{x-y}$ dependence of this energy, which both share a large range of dispersionless values. The feature of an errorless energy evaluation reassures the nature of an eigenstate.

$\alpha < 1.2$, the simulation is able to give out a better variational state than the singlet dimer state due to the fact that E_{tot} is lower. This critical α is in good agreement with other theoretical solutions to this problem (56).

Another surprise comes from the fact that there is very strong degeneracy in the variational phase space for $\alpha > 1.2$, which is shown in Fig. 4.3 on several effective hoppings using $\alpha = 1.25$ as an example. The wide flat errorless basin for the diagonal hoppings very clearly illustrates the degeneracy. Yet actually this degeneracy is an artifact from the simulation because it is well known that the singlet dimer ground state is a unique state and involves only spin degrees of freedom. However, the fermionic representation of a spin operator, expressed in Eq. 1.19,

artificially introduces spacial degrees of freedom from a particle's creation and annihilation operators. The singlet property is implicitly taken care of by requiring the spacial pairing amplitude of two electrons to be of even parity. All these comments imply that it is possible for the simulation to bring up a flat dispersion, but they still don't answer why the simulation must give rise to such a fact. This is still an open question in the current study. Possible reasons might include the $SU(2)$ spin rotational symmetry inherited in the Heisenberg Hamiltonian. Reasons might also be related to the fact that a spin singlet can have arbitrary even spacial functional forms.

The exactness of the simulated ground state as the singlet dimer ground state can also be proved by the magnetic correlation on the lattice. Theoretically, the magnetic correlation for two sites in the spin dimer state would be

$$\chi_{ij} = \begin{cases} -\frac{1}{2} & \text{for site } i,j \text{ linked by a diagonal dimer bond} \\ 0 & \text{o.w.} \end{cases} .$$

This result is fully reproduced by the simulation within an error of 10^{-4} here.

Finally, the current trial wavefunction might be used to add efforts to determine the critical α value, α_c, beyond which the singlet dimer state ceases to be the ground state of the SS lattice. One can even reason that this trial wavefunction will give a better estimation on α_c than other current methods except for the exact diagonalization study, which is, however, limited by small lattice size. The calculation would be similar to what has been presented in Fig. 4.2, but would be more elaborate. It was not carried out in this study because of time limit. There are several things to consider if one decides to work on this problem. First, the rigorous α_c value can never be obtained unless the true ground state is known around α_c. Second, even with the current trial wavefunction, α_c would be lattice size dependent because the other ground state for $\alpha < \alpha_c$ would be the case. Third, which is purely technical, it would be extremely hard to locate a slightly energetically favored local minimum in a large dispersionless phase space.

4.2 Physical properties of the doped SS lattice

The RVB wavefunction used in this study has been shown to give the exact ground state for the undoped (or parent) SS lattice describing $SrCu_2(BO_3)_2$. This fact is so far known to be unique for a quantum many body system. It implies that the trial wavefunction is very well controlled for studying the SS lattice under small doping, because the ground state energy changes continuously with doping. The mobile charge carriers can be introduced either as holes by taking electrons out of the system, for example, replacing Sr^{2+} with Na^{+}, or as electrons by adding electrons into the system, for example, replacing Sr^{2+} with Al^{3+}. However, these are difficult to synthesize. Different groups are trying these replacements, but only one successful case has been reported so far. In this case, only insulating behavior is found for both doping cases. In the following paragraphs, we would like to discuss the predictions from the current variational study.

It is straightforward to treat the hole doping in the variational study by assigning fewer electrons than the number of lattice sites into the system. But the electron doping cannot be treated alike because the model Hamiltonian requires a single occupation on each site. This difficulty is addressed by a particle-hole transformation in the next paragraph. Another complication arising during the simulation is the existence of multiple minima in the phase space, which is not surprising for a function with so many variational parameters. What is special in the electron doped case is that many minima well-separated in the phase space have close energies to each other. However, it is lucky that these minima always give similar physical observables, as is verified by direct calculations. This greatly simplifies the analysis for the electron doped case.

The physical quantities are usually presented in the same graph with both electron and hole dopings plotted, electron doping to the left and hole doping to the right, except for those graphs that only provide information for a single doping type. From these figures, it is notable that there is a strong asymmetry between these two types of doping. The hole doped SS lattice can be described as a plaquette d-wave pairing superconductor, while the electron doped SS lattice is a valence bond strange metal. The result for the electron doped case is negotiable because it

is very odd to have a metallic state in a strongly interacting system without symmetry breaking at zero Kelvin (93). However, the current trial wavefunction doesn't contain a magnetically ordered state as one of its options. Such a state cannot be excluded from a ground state.

How to treat electron doping? With using the $t-J$ Hamiltonian on the SS lattice, electron doping cannot be treated by simply assigning the system more electrons than total number of lattice sites. This must result in sites with double occupancy and is thus forbidden by the Hamiltonian. A way around is this to see whether it is possible to transform electrons into holes by a particle-hole transformation while at the same time keeping the Hamiltonian and its relevant restrictions unchanged.

The $t-J$ Hamiltonian expressed in Eq. 4.3 can be equivalently written as

$$\begin{aligned}\hat{H} = &\sum_{\langle i,j\rangle} t c^{\dagger}_{i,\sigma} c_{j,\sigma} + \sum_{\langle l,m\rangle} t' c^{\dagger}_{l,\sigma} c_{m,\sigma} \\ &+ \sum_{\langle i,j\rangle} J\left(\mathbf{S}_i \cdot \mathbf{S}_j - \frac{n_i n_j}{4}\right) + \sum_{\langle l,m\rangle} J'\left(\mathbf{S}_l \cdot \mathbf{S}_m - \frac{n_l n_m}{4}\right) \qquad (4.6)\end{aligned}$$

$$\sum_{\sigma} n_{i,\sigma} \leq 1 \qquad (4.7)$$

where $\langle i,j\rangle$ denotes nearest neighbor sites and $\langle l,m\rangle$ denotes next nearest neighbor sites. The only difference between Eq. 4.3 and the above expression is that the single occupation restriction is explicitly written out here in Eq. 4.7.

Let us consider a general particle-hole transformation

$$c_{j,\sigma} \rightarrow c^{\dagger}_{j,\sigma} e^{i\theta_j} \qquad (4.8)$$

where j is the lattice index, θ_j is some additional phase factor to $c^{\dagger}_{j,\sigma}$ and satisfies the same symmetry and boundary conditions as that of the SS lattice. Remember that different choices of θ_j don't change the physics of the problem. It is straightforward to check that under this transformation $\mathbf{S}_i \cdot \mathbf{S}_j$ is invariant and $\sum_{\sigma} n_{i,\sigma} \leq 1$ is still satisfied, while $n_i n_j$ is shifted by an irrelevant constant term. What is nontrivially changed is the hopping term

$$\sum_{\langle i,j\rangle} t c^{\dagger}_{i,\sigma} c_{j,\sigma} \rightarrow \sum_{\langle i,j\rangle} \left[-t e^{-i(\theta_i - \theta_j)}\right] c^{\dagger}_{j,\sigma} c_{i,\sigma}.$$

Thus the $t-J$ Hamiltonian would be kept unchanged if a corresponding transformation on the hopping term is introduced as

$$t_{ij} \rightarrow t_{ij}^{*} = -t_{ij} e^{-i(\theta_i - \theta_j)}. \tag{4.9}$$

Different options can be chosen for θ_i. The simplest choice is

$$\theta_i = 0$$

which gives

$$t \rightarrow t^{*} = -t \tag{4.10}$$

$$t' \rightarrow t'^{*} = -t'. \tag{4.11}$$

Another choice would be

$$\theta_i = \frac{\pi}{a}\left(x_i + y_i\right)$$

where a is the lattice constant and (x_i, y_i) is the coordinate of the ith lattice site, and this gives

$$t \rightarrow t^{*} = t \tag{4.12}$$

$$t' \rightarrow t'^{*} = -t'. \tag{4.13}$$

These two choices seem to be the only options which give different relationships between the original and the transformed hopping amplitude and at the same time satisfy the requirements on the symmetry and boundary conditions on the lattice.

By collecting all the above information, it is proved that the hole doped case for a $t-J$ Hamiltonian with hopping $\pm t, -t'$ describes the same physics as the electron doped case for a $t-J$ Hamiltonian with hopping t, t'.

What is shared by both doping cases? Although the behaviors for both doping cases are totally different in many physical aspects, they share one thing in common. That is, the charge distribution is almost isotropic on the lattice. The maximum relative charge density difference, defined as $\left(n_{\max} - n_{\min}\right) / \left(n_{\max} + n_{\min}\right)$, is about 0.1% among the sites. This is

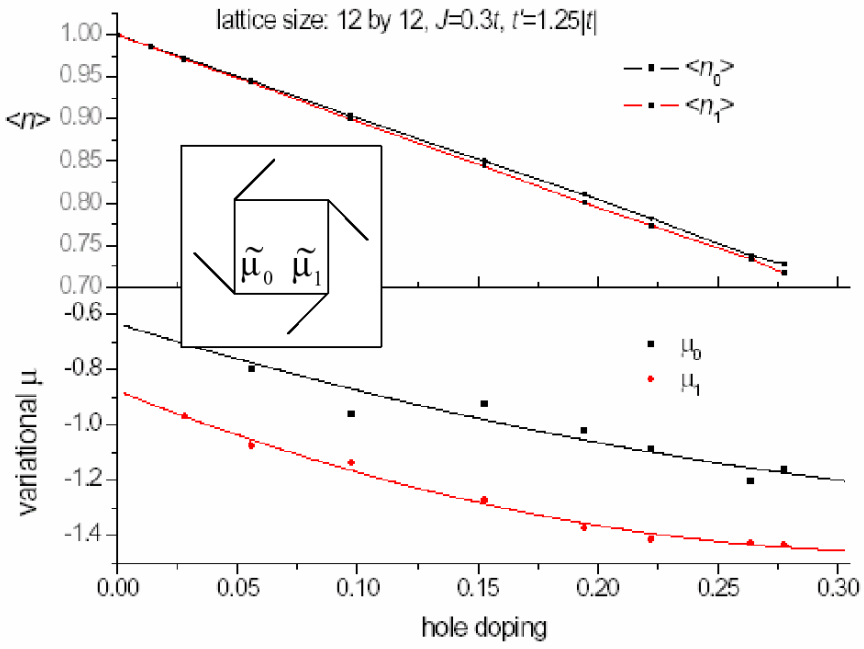

Figure 4.4 Charge expectation, $\langle n \rangle$, and variational chemical potentials, $\tilde{\mu}$, for different hole concentrations are shown in this plot. The curves are just guide to eye. The inset is excerpted from Fig 4.1 to show $\tilde{\mu}s$ within the unit cell. The upper panel shows charge expectation on the two inequivalent sites. A tiny relative difference of 0.1% in charge density appears as doping increases. The lower panel shows different $\tilde{\mu}$s on the two inequivelant sites. The big difference in $\tilde{\mu}$s are in sharp contrast to the nearly homogenous charge distribution on the lattice.

illustrated for the hole doped case in the upper panel of Fig. 4.4. This conclusion is reassuring for the Hamiltonian under study. Otherwise Coulomb interactions between nearby sites would have to be included into the model.

However, the two variational chemical potentials can be distinctive from each other. To use the case of hole doping as an example, the distinction is shown in the lower panel of the figure with a smaller $\tilde{\mu}$ at site 1 within a unit cell. A smaller $\tilde{\mu}$ at site 0 would be the other degenerate solution. The fact that the charge is still balanced between these two sites reflects similar degeneracy in other variational parameters in order to counteract the biasness raised

by $\tilde{\mu}$. In the plot, both the variational $\tilde{\mu}$ decrease as doping increases, as is expected for a true chemical potential to accommodate less and less electrons in the system. This suggests that the variational chemical potentials are still related in some way to the true chemical potential. However, the difference in $\tilde{\mu}$ clearly shows that they are not the true chemical potential which would otherwise be uniform in the whole system, as is required by phase equilibration. On the other hand, the strong tendency to reach charge homogeneity can be regarded as a self-consistency check on the current study. That the system chooses such a nontrivial way to maintain this charge homogeneity implies a possible intrinsic spontaneous symmetry breaking in the problem.

Renormalized diagonal hoppings The strong asymmetry manifests itself between both doping types in the effective hoppings. The doping dependence of these hoppings are shown in Fig. 4.5. The attention is mainly focused on the two effective diagonal hoppings, $\tilde{t}_{x+y}$ and $\tilde{t}_{x-y}$, since they give the predominant renormalization effects as compared to the other hoppings. The values of the hoppings shown in the plot should not be taken seriously but the trends should. This is because the effective hoppings can have a different symmetry with respect to that of the original lattice. Thus the hopping, treated as the energy unit in the trial wavefunction, might not be continuously dependent on the hole concentration. (However, the effective hoppings on the lateral directions don't differ too much.) The descending trend on the renormalization effect as doping increases is easy to understand. Less charge carriers on the lattice reduce chances to form doubly occupied sites. Thus the on site repulsion plays a less important role.

In the electron doped case, $\tilde{t}_{x\pm y}$ are nearly indistinguishable from each other, which assumes that there is no symmetry breaking on the lattice. The doping dependence of $\tilde{t}_{x\pm y}$ follows a monotonic decrease. In the case of no doping, $\tilde{t}_{x\pm y}$ are of the order of 10 times $\tilde{t}_{x_1}$, the energy unit in the trial wavefunction, shown in Fig. 4.3. As doping increases, $\tilde{t}_{x\pm y}$ gradually reduce till finally the $\tilde{t}_{x\pm y}/\tilde{t}_{x_1}$ ratio reduce to the bare ratio, 1.25, at about 25% of doping. If we still assume the conclusion made in the last chapter is correct concerning an effective dispersion within the RVB picture, which says that the effective dispersion describes largely the motion

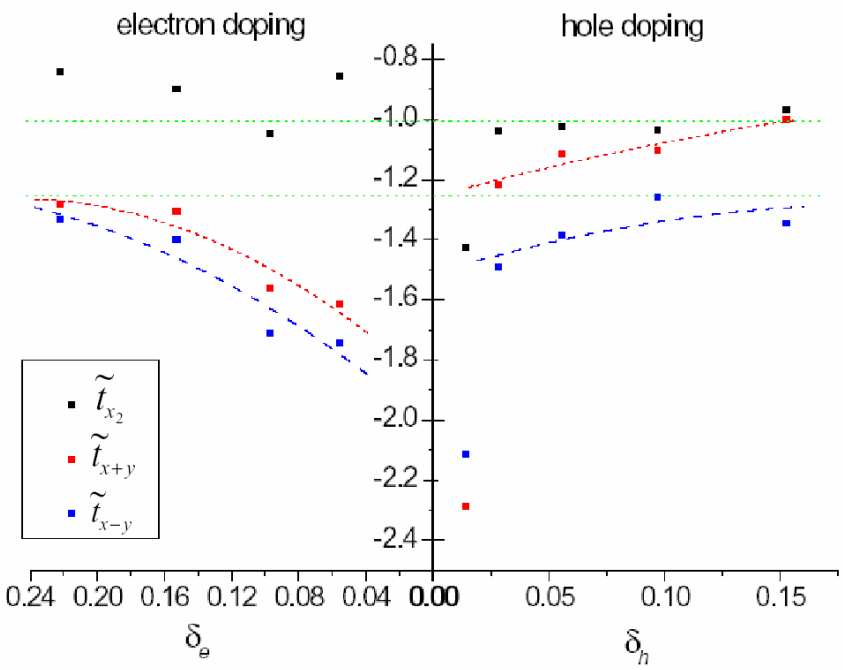

Figure 4.5 Effective hoppings vs. dopings for both doping cases, electron doping shown on the left and hole doping on the right. Dotted horizontal lines indicate the two different kinds of original hoppings on the lattice; dashed curves are guide to eye and show trends of doping dependence. Please notice that the absolute y values are in descending order in the figure and $\tilde{t}_{x_1}$ is treated as the energy unit in the trial wavefunction. For the electron doped case, increasing doping reduces hopping renormalization. For the hole doped case, the effective diagonal hoppings are much more enhanced for very small doping. They then are abruptly reduced beyond some doping threshold and becomes distinguishable to each other.

of quasiparticles in the system, the enhanced effective hopping along the diagonal directions suggests that quasiparticles prefer a hopping or exchange interaction along the diagonal directions. This implies that the electrons prefer to be localized along the diagonal directions when additional electrons are added into the system. This naturally leads us to believe that the same physics in the parent compound would be preserved here. This guess is later verified by the calculation of magnetic correlation, but it is not completely true.

In the hole doped case, the doping dependence of $\tilde{t}_{x\pm y}$ has a discontinuity around $\delta_h^c = 2.5\%$. For doping less than δ_h^c, the effective diagonal hoppings are much more enhanced than their bare values, very similar to that of the electron doped case. As doping passes over δ_h^c, $\tilde{t}_{x\pm y}$ are strongly reduced in magnitude. Meanwhile, they become distinguishable with one effective hopping being renormalized to be less than 1.25 while the other a bit larger than 1.25. These are clearly shown in the right panel of Fig. 4.5. Obviously the abrupt discontinuity suggests a phase transition at 2.5% doping. The nature of both phases will be clarified in later paragraphs. The phase for $\delta < \delta_h^c$ might have some similarities with that of the electron doped case while the phase for $\delta > \delta_h^c$ should be a novel one reflecting less frustration along the diagonal directions.

The difference in the behavior for both doping cases can be observed from the particle-hole transformation defined in Eq. 4.8. It let $t' \to -t'$ to mimic the behavior for the electron doped case. Considering the fact that $|t'/t| > 1$ for $SrCu_2\left(BO_3\right)_2$, t' would then be the major hopping amplitude in the Hamiltonian and its sign would surely make a difference.

Magnetic correlation Another interesting contrast between electron and hole doping is the magnetic correlation. Their doping dependences are shown in Fig. 4.6 by three representative values, χ_{00}, the average occupation on the lattice shown with black solid lines, $\chi_{0,x}$, the magnetic correlation between two nearest neighbor sites shown with red dashed lines and $\chi_{0,-x-y}$ the magnetic correlation along the diagonal bond where a singlet is preformed in the parent compound, shown with black dotted lines. In both doping cases, χ_{00} reduces linearly as doping increases. This behavior is actually expected, and can be treated as a validity check on the code. What are of major difference are $\chi_{0,x}$ and $\chi_{0,-x-y}$.

In the electron doped case, $\chi_{0,x}$ is always kept small but $|\chi_{0,-x-y}|$ reduces gradually from

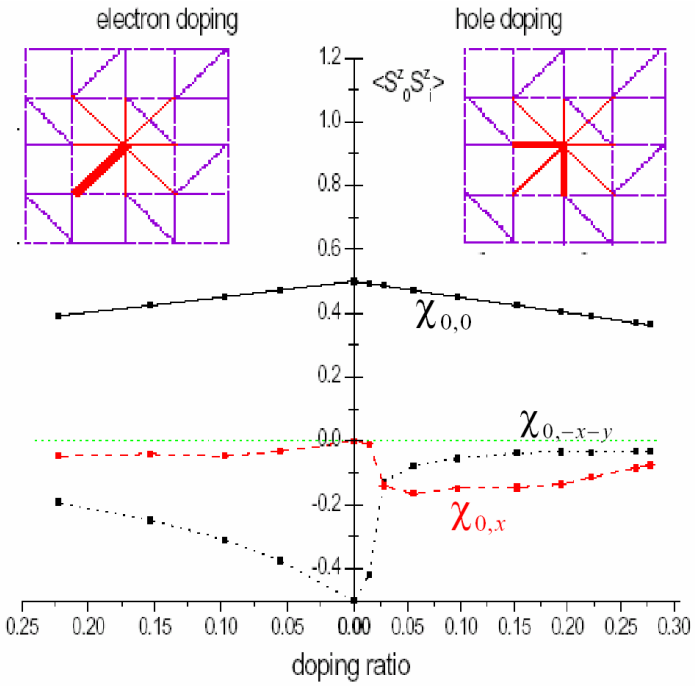

Figure 4.6 Doping dependence of $\chi_{0,i}$ for the three chosen directions. The dark solid curve shows $\chi_{0,0}$ on the same site; the dark dotted curve shows $\chi_{0,-x-y}$ along the diagonal bond direction and the red dashed curve shows $\chi_{0,x}$ between nearest neighbors on the x axis. For the electron doped case, the magnetic correlation pattern is very similar to that of the parent compound, illustrated in the left inset for 10% doping. The strongest magnetic correlation is still along the diagonal bond direction, and a small component along x and y axes. This is shown with thick and thin line segments respectively in the inset. For the hole doped case, an abrupt change in magnetic correlation happens around 2.5% of doping with the strongest component being changed from the diagonal direction to the lateral directions. The right inset illustrates the strongest magnetic correlations along x and y axes for 10% hole doping.

the value 1 for the parent compound to 0.2 at about 25% doping. This magnetic correlation pattern appears for all the energy minima studied and is very similar to that of the parent compound. This is thus a strong indication that the underlying state is still closely related with singlets along the specific diagonal bonds. The reduced magnitude in $\chi_{0,-x-y}$ implies the extra electrons introduced into the system are scattered around and separated from each other, as can be seen from the nearly linear dependence on doping. That is to say, the singlets are more diluted as doping increases. On the other hand, the deviation from linearity for doping dependence of $\chi_{0,-x-y}$ must be related with the small yet finite $\chi_{0,x}$. This means that electrons are not fully isolated in the specific diagonal bonds as extra electrons are added in. They are now able to interact and communicate with each other along the lateral directions. However, these effects are extremely short ranged, as can be seen from Fig. 4.7, the spacial dependence of different magnetic correlations. From the left panel of this figure, it is clear that the magnetic correlations die out within one lattice constant. Thus the electron doped system can still be described using a valence-bond-state-like picture, fully consistent with the exact diagonalization study in Ref. (68). Then, how about its conductivity? Would it still be an insulator as the parent compound? This has to be checked explicitly by using the low frequency Drude weight.

In the hole doped case, the doping dependence of χ is qualitatively different from that of the electron doped case, as shown in Fig. 4.6. The difference lies in the two related aspects, the existence of a possible phase transition and a re-organization of the electronic behavior. Around $\delta_h^c = 2.5\%$ doping, there is an abrupt change in the magnetic correlation. When doping is smaller than δ_h^c, the pattern is similar to that of the electron doped case although the reduction in $\chi_{0,-x-y}$ is much quicker (not shown in the figure). When δ is beyond δ_h^c, χs along the lateral directions become dominant among all the magnetic correlations while χ along the diagonal bond direction is strongly reduced. However, they are still comparable to each other in magnitude and are of the same nature. For example,

$$\frac{\chi_{0,-x-y}}{\chi_{0,x}} \approx \frac{1}{3} \tag{4.14}$$

for 10% of hole doping. The spacial dependence of the magnetic correlations are shown in the

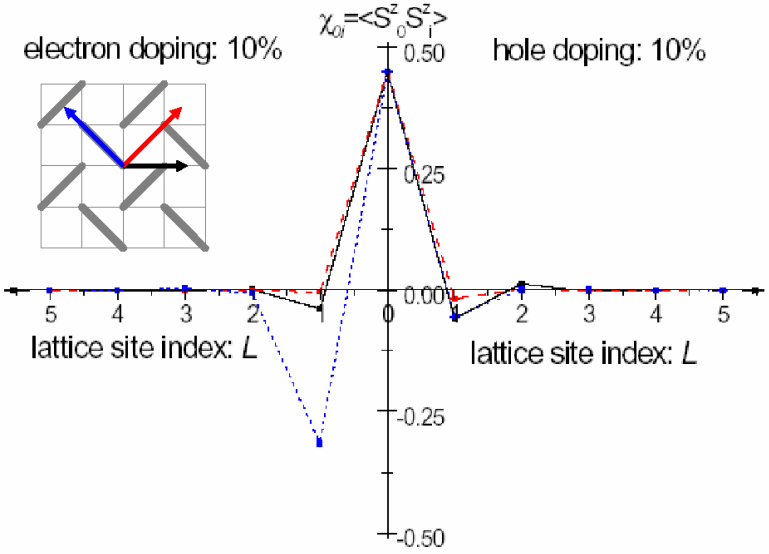

Figure 4.7 Spacial dependence of $\chi_{0,i}$ on the lattice at 10% doping. Curves with different colors and line styles represent χ along the three directions shown on the lattice in the inset. The black solid line represents $\chi_{0,x}$, the blue dotted line represents $\chi_{0,-x-y}$ and the red dashed line represents $\chi_{0,x-y}$. For the electron doped case, the strongest magnetic correlation is along the diagonal bond where the singlet lies in the parent compound. However, there also exists a small magnetic correlation along the lateral directions. All χs are short ranged and die out beyond one lattice constant. For the hole doped case, the magnetic correlations are qualitatively different from that of the parent compound. The strongest magnetic correlations are now along the lateral directions, but χs to all the nearest and next nearest neighboring sites are comparable to each other. Their range is still short, but extends to two or more lattice constants.

right panel of Fig. 4.7. They extend wider on the lattice as compared to the electron doped case although they are still short-ranged. All these show that the electrons are antiferromagnetically correlated to each other not only between nearest neighboring sites, typical for a square lattice without frustration or with only weak frustration, but also between next nearest neighbors. This implies that the system reorganizes itself to give rise to a totally different type of geometric frustration in the system compared to the original SS lattice. The effective hoppings, $\tilde{t}$, revealed for the hole doped case suggest that the electrons develop a stronger tendency to delocalize along the lateral directions.

Pairing between two electrons This set of variational parameters, $\tilde{\Delta}$, are most seriously affected by the existence of multiple energy minima, especially in electron doped case. Unlike the undoped SS lattice, the local minima are well defined in the variational phase space. For electron doped case, these minima are very close in energy but can be far apart in $\tilde{\Delta}s$, whose optimal values don't seem to be logically related in any way. For example at 10% electron doping, two energy minima are found to be

$$\tilde{\Delta}_{x_1} = 0.073, \tilde{\Delta}_{x_2} = 0.034, \tilde{\Delta}_{y_1} = -0.286, \tilde{\Delta}_{y_2} = -0.244, \tilde{\Delta}_{x+y} = 0.282, \tilde{\Delta}_{x-y} = 0.359$$

$$\tilde{\Delta}_{x_1} = -1.32, \tilde{\Delta}_{x_2} = -1.48, \tilde{\Delta}_{y_1} = -1.12, \tilde{\Delta}_{y_2} = -1.28, \tilde{\Delta}_{x+y} = -0.84, \tilde{\Delta}_{x-y} = -1.88$$

with a relative energy difference of $\Delta E/\bar{E} = 0.3\%$. Thus there is no clear physical picture that is suggested by the pairing parameters for the electron doped case.

The physical picture for the hole doped case is, however, much better suggested by the pairing parameters for doping larger than δ_h^c. It is statistically found that the following relationships are satisfied among the pairings

$$\tilde{\Delta}_{x_1} \approx -\tilde{\Delta}_{y_2} \tag{4.15}$$

$$\tilde{\Delta}_{x_2} \approx -\tilde{\Delta}_{y_1} \tag{4.16}$$

$$\tilde{\Delta}_{x+y} \approx \tilde{\Delta}_{x-y} \approx 0 \tag{4.17}$$

together with

$$\frac{\tilde{\Delta}_{x_1}}{\tilde{\Delta}_{x_2}} \gg 1 \text{ or } \frac{\tilde{\Delta}_{x_2}}{\tilde{\Delta}_{x_1}} \gg 1, \tag{4.18}$$

where both the cases with equal ratio are degenerate in energy. Other variational parameters are assumed to change accordingly. Mapped back onto the SS lattice, the pairings with larger strength form regularly aligned squares with an original diagonal exchange interaction contained inside. This is illustrated in the inset of Fig. 4.8. By taking into account the fact that the two pairing parameters on the same axis share the same sign, as indicated in Eq. 4.18, the state can be called a plaquette d-wave pairing state. The stability of this state is controlled by the larger pairing parameter, whose doping dependence is shown in Fig. 4.8.

For small doping, less than 2.5%, the pairing is very much complicated by the existence of multiple energy minima and thus the pairing nature is undetermined. As doping increases, plaquette d-wave pattern emerges with very strong strength and then gradually reduces in magnitude. The location of each small plaquette is contrary to one's expectation. It shows that the hole doped system tends to have lower symmetry by choosing to locate a plaquette on a unit cell with only 2-folded rotational symmetry. At the same time, the pairing plaquette contains in it the weakened effective diagonal hopping if the effective hoppings are also mapped onto the pairing plaquette lattice. These observations are in full consistency with what have been observed in the magnetic correlation, including the fact that χ are antiferromagnetic to all the nearest and next nearest neighboring electron pairs, and, $\chi_{0,x}$ and $\chi_{0,-x}$, or $\chi_{0,y}$ and $\chi_{0,-y}$, differ slightly from each other. The formation of such a pairing pattern clearly shows how the system fully reorganizes itself and leads to a delocalization of singlets. It implies that the hole doped system is now a true RVB state as compared to the electron doped case. Why such a plaquette phase would be formed and why it chooses such a specific unit cell to stay might be related with strong quantum fluctuation. As has been analyzed in Ref. (66), a half-filled SS lattice with $Sp\,(N)$ symmetry leads to several plaquette states, including one similar to ours, once strong quantum fluctuations were taken into account. It is thus plausible that doping with holes is one way to enhance quantum fluctuations.

The robustness of the plaquette d-wave pairing phase is manifested by comparing it to two other phases, the homogeneous pairing phase and the noninteracting phase. Taking as an example the case of 10% hole doping and denoting energies to these three phases as $E_{\text{plaquette}}$,

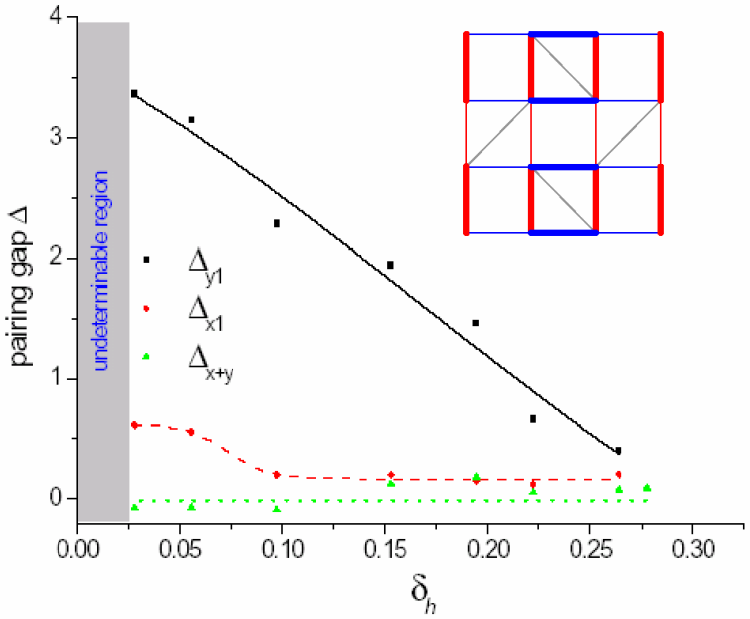

Figure 4.8 Pairing strength vs. hole doping concentration δ_h. The curves are just guides to eye. The pairing nature is d-wave like but with pairing strength alternating in space. An illustration is given in the inset to show what the pairing pattern looks like on the lattice. The thickness in the line segments corresponds to pairing magnitude and red/blue color corresponds to different sign of the pairing. The diagonal lines indicate the location of the singlets in the parent compound. For $\delta_h < 2.5\%$, there exists too many local minima close in energy and thus pairings are therefore not well-determined. Otherwise, the two pairings with different strength along lateral directions reduces with doping. The diagonal pairings are always tiny in the strength.

$E_{\text{homogenous}}$ and $E_{\text{noninteracting}}$, the relative energy gain can be expressed as

$$\frac{E_{\text{plaquette}} - E_{\text{homogenous}}}{E_{\text{homogenous}} - E_{\text{noninteracting}}} \approx 1.0 \tag{4.19}$$

together with the absolute energy gain

$$E_{\text{plaquette}} - E_{\text{homogenous}} \approx -0.043t. \tag{4.20}$$

At the same time, the plaquette d-wave pairing phase is verified to be stable against J values to as small as $J = 0.03t$.

ODLRO and low frequency Drude weight It is now time to see whether the doped materials are conducting or superconducting. The benchmark of superconductivity is the nonvanishing off diagonal long range order (ODLRO) defined in Eq. 2.38. It is calculated for both doping cases and is shown in Fig. 4.9. It is found for the electron doped case that the ODLRO is constantly zero within an error limit of 10^{-4} for all doping concentrations under consideration. As has been mentioned before, although complicated by multiple energy minima, pairings between electrons always exist. The vanishing ODLRO shows, however, these pairs don't move coherently in phase. Actually even the mobility of electrons is also in doubt if a comparison is made with respect to the many physical aspects between the electron doped case and the insulating parent compound. This concern will be carefully addressed.

The hole doped case corresponds to an inhomogeneous superconductor. Two different ODLROs are found due to the plaquette pairing formation on the lattice. They are shown as the black solid line and green dotted line in the right panel of Fig. 4.9. There exists some threshold doping value, δ_0, for finite ODLROs to appear. This δ_0 seems to be smaller than δ_h^c where χ changes most rapidly. As doping increases, the major ODLRO doesn't change monotonically, but the smaller one does. The maximum ODLRO appears around 20% hole doping. Simulation is not carried out beyond 25% doping for fear that the current trial wavefunction might not be good enough. The singlet singlet correlation function, $F_{ab}\left(\mathbf{R} - \mathbf{R}'\right)$, is shown against separation between two singlets in the inset of the figure. Two cases of spin orientations are provided to give enough details on the ODLRO. From the graph, it can be seen that the spacial

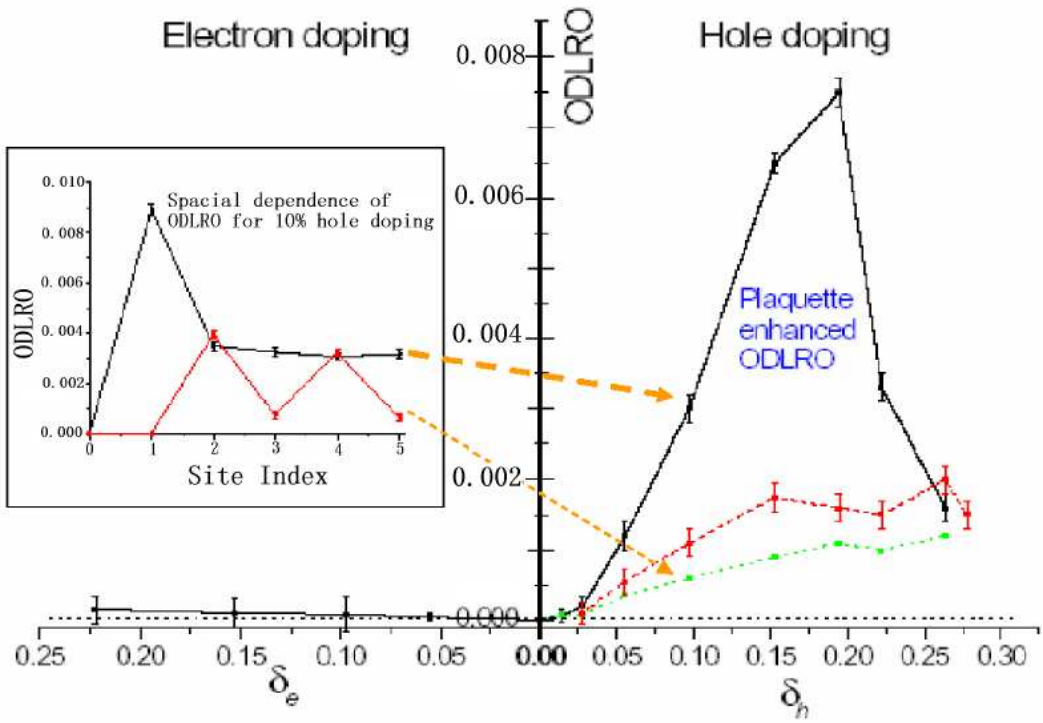

Figure 4.9 The ODLRO vs. doping for both doping cases. For electron doping, the ODLRO vanishes within error limit; for hole doping, three different ODLROs are provided. The dark solid and green dotted curves correspond to the plaquette enhanced and weakened ODLRO respectively; red dashed curve shows the ODLRO calculated from the homogenous d-wave pairing in order to show the plaquette enhanced superconductivity. The spacial dependences for two ODLROs, $F_{\hat{y}\hat{y}}(n\hat{x})$ in black and $F_{\hat{x}\hat{x}}(n\hat{x})$ in red, are shown for 10% hole doping in the inset of the left panel. Here n is the site index. The stable value which levels off corresponds to the enhaced ODLRO shown in the right panel (indicated by the upper broken arrow).

equilibration is reached when two singlets are separated by only two lattice constants. This is surprising and indicates the spacial wavefunction of singlet pairs are still confined in space, which might be a remnant effect from the undoped parent compound. The spacial dependence of $F_{ab}\left(\mathbf{R}-\mathbf{R}'\right)$ can actually be related to the pairing strength as

$$F_{ab}\left(\mathbf{R}-\mathbf{R}'\right)=\left\langle \mathcal{B}^{\dagger}_{\mathbf{R},\mathbf{R}+a}\mathcal{B}_{\mathbf{R}',\mathbf{R}'+b}\right\rangle \propto \tilde{\Delta}^{*}_{\mathbf{R},\mathbf{R}+a}\tilde{\Delta}_{\mathbf{R}',\mathbf{R}'+b} \tag{4.21}$$

for $|\mathbf{R}-\mathbf{R}'|>1$ where the lattice constant is chosen to be the unit. When the two singlets are robust in both pairing strengths, F_{ab} is also strong; while one of them is weak, F_{ab} is also weak.

The physics of the inhomogeneous superconductor is clarified by comparing the two ODLROs mentioned above, called the enhanced or weakened ODLRO from now on, to the ODLRO from the trial wavefunction with homogeneous pairings, which is automatically optimized to be d-wave. The homogeneous ODLRO, $\psi_{s,\mathrm{hom}}$, is shown in Fig. 4.9 with a red dashed line and is between the other two ODLROs. Compared to $\psi_{s,\mathrm{hom}}$, the enhanced ODLRO, and thus the superconductivity of the inhomogeneous superconductor, is obviously boosted by the formation of the plaquette pairing pattern, as is also noticeable from Eq. 4.21 considering the fact that

$$\tilde{\Delta}_{x_2}<\tilde{\Delta}_{\mathrm{homo}}<\tilde{\Delta}_{x_1}$$

or the other way around. For example at about 20% doping, the enhanced ODLRO is more than 3 times of the homogeneous ODLRO (optimal $\tilde{\Delta}_{\mathrm{homo}}\approx 0.3$ at 20% doping). Why the plaquette pairing pattern would enhance the superconductivity might be explained if not fully in a recent publication (94). The authors suggest that, within the weak coupling BCS theory framework, superconductivity would be enhanced if the spacial characteristic length, L, is comparable to superconducting coherence length, ξ, because the enhanced electron pairs would then tunnel most efficiently between the nearby superconducting islands. In my case, L is the distance between two nearby pairing plaquettes, which equals one lattice constant, and ξ is also about one lattice constant. Thus these two length scales satisfy the condition proposed in the reference.

As some further discussions, the ODLRO from the current RVB wavefunction is about 10% of that of the unprojected BCS wavefunction using the same set of variational parameters. Secondly, the mean field transitional temperature, T^*, can be estimated as

$$T^* \simeq \sqrt{t\,|E_{\text{plaquette}} - E_{\text{noninteracting}}|} \simeq 0.3t \tag{4.22}$$

if the normal state entropy is $S \simeq T/t$ and the mean field T^* of a 2-D model yields a rough estimate for an anisotropic 3-D material. By considering that the actual transition temperature would be reduced by fluctuations and strong correlation effects, $T_c \simeq T^*/10$ is of several Kelvins at best.

Let us go back to the previous question, what would be the characteristics of the electron doped SS lattice? Would it still be an insulator considering that it shares so many similar features with its parent compound? These include, for example, existence of multiple minima close in energy, enhanced effective diagonal hoppings, similarity in the magnetic correlation pattern and the vanishing ODLRO. However, the calculation on the low frequency Drude weight, D_{low}, whose static version is directly related to the conductivity, shows that this is not the case. Actually D_{low} is even bigger than that for the hole doped material of same hole concentration, which is known to be a superconductor. The doping dependence of Drude weight is shown in Fig. 4.10. For the electron doped case, it seems to satisfy

$$D_{low} \simeq 3.18\delta_e t \tag{4.23}$$

at small doping concentration, where δ_e is the electron doping concentration and t is the bare lateral hopping as the energy unit. Thus the electron doped material is concluded to be a strongly correlated metal.

Finite size effects and some remarks Due to the large amount of computational time involved in the simulation, the finite size effect is not completely checked. Alternatively, the plaquette phase is verified to remain a local minimum on the 18×18 lattice. Then, the ODLRO was calculated on larger lattice sizes by using the same optimal parameters found on the 12×12 lattice. The calculations are shown in Fig. 4.11 for 10% doping. From the

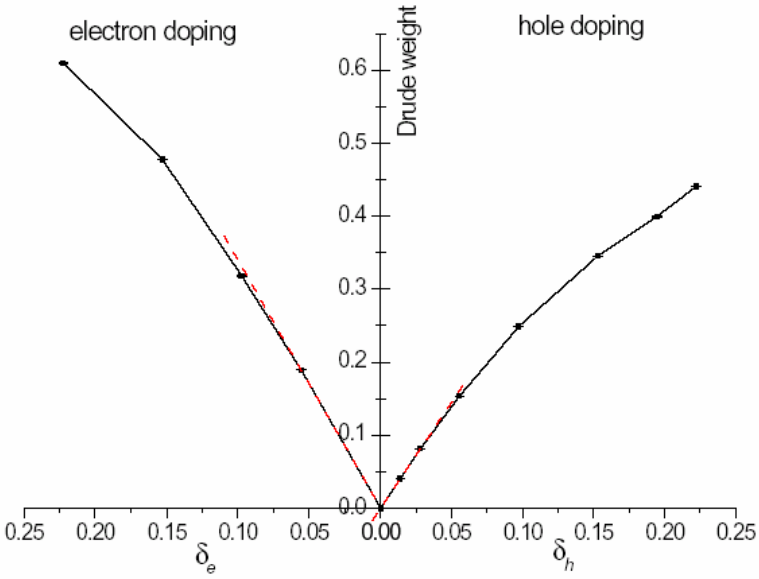

Figure 4.10 Low frequency Drude weight vs. doping. For small doping in the electron doped case, $D_{low} \simeq 3.18\delta_e t$. For small doping in the hole doped case, $D_{low} \simeq 2.9\delta_h t$.

plot, only a tiny dependence on the lattice size is found for the ODLRO. This fact can be understood if the electron pairing wavefunction is of short range in space and thus can barely feel the lattice boundary. This is consistent with the fact that the ODLRO stabilizes within a very short separation between two singlets. Thus, it is summarized that the existence of the plaquette phase for the hole doped case argues robustly against the finite size effect.

There are several things which need comments or further work. There is a sharp contradiction between the current prediction and the only experimental result in Ref. (70). I would not worry too much about the hole doped case since the energy gain is huge between the plaquette phase and the noninteracting phase, although its vulnerability against possible distortion and impurities in the $CuBO_3$ plane is still unclear in this study. However, the electron doped case causes more concerns because of its close similarity to the parent compound. The sudden losing of the insulating behavior as electrons are added into the system is pretty annoying although this is not in principle forbidden. However, the experimental insulating behavior against the

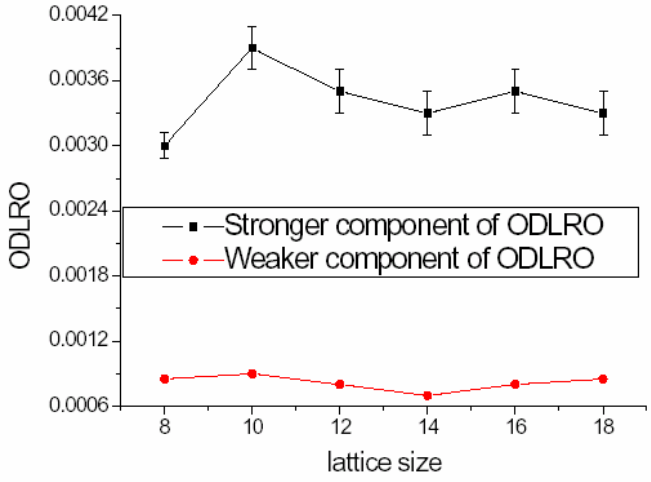

Figure 4.11 Shown here is the size dependence of the enhanced and the weakened ODLRO evaluated using the same set of parameters under different hole concentrations. From the plot, it is obvious that the ODLRO is much weakly size dependent.

predicted metallic state for finite doping can be explained by Anderson's argument with the impurities and lattice distortion which are introduced inevitably during the doping process (95). One might also suppose the electron doped system may be involved with other degrees of freedom which cannot be, or have not been, addressed by the current wavefunction.

One candidate among other possible degrees of freedom is the spin degree's freedom. The spontaneous magnetization cannot be addressed by the current RVB wavefunction. However, a slightly doped system is potentially able to develop finite magnetization (96). Maybe this is also the case for the electron doped case, which would mean that the conclusions developed here are not related with the experiment. However, the exact diagonalization study of doping with one electron on a small lattice seems to show that finite magnetization might not be the case here (68).

Another choice is to consider other spontaneous symmetry breaking phases, for example, the flux phase defined as

$$\tilde{t}_{ij} = \left|\tilde{t}_{ij}\right| e^{\theta_{ij}} \text{ and } \tilde{\Delta}_{ij} \in \mathbb{R}$$

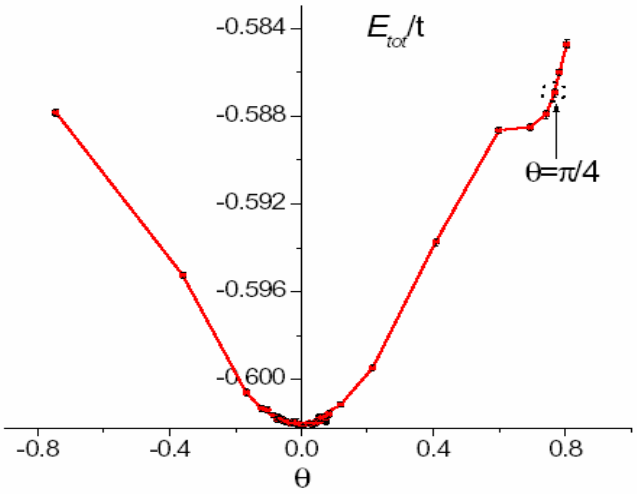

Figure 4.12 Flux phase, θ, dependence of total energy is shown for 5% electron doping. Starting with optimal parameters found for $\theta = \pi/4$, minimization is carried out on θ with other parameters fixed at the optimal values. The curve obviously shows that $\pi/4$ flux phase is not energetically favored.

where θ_{ij} denotes any phases accompanying the effective hopping. What have been considered so far correspond to the zero flux phase. For the half-filled case, the flux phase is degenerate to some phase with complex pairing strength. But this equivalence doesn't hold if doping is introduced (97). The main focus here is on the π flux phase defined by

$$\theta_{ij} = \frac{\pi}{4} \tag{4.24}$$

in order to gain an additional phase factor of π for an electron to move around the four edges of any smallest square on the SS lattice. This is because some mean field theory work has predicted its existence within doping range of $0.023 \sim 0.12$ (67). In the current simulation, 5% doping was chosen and θ was changed continuously while all the other parameters are kept at the optimized values for the π flux phase. The results are shown in Fig. 4.12 and indicate that a vanishing flux phase is very much preferred.

4.3 Slave Boson mean field treatment

Slave-Boson mean field theory has also applied to the doped SS lattice. Several predictions have been made, including singlet dimer d-wave pairing state (61), π-flux phase (67), etc. The numerical simulation, however, has disapproved the $\pi-$flux phase and shows that it is not even a local energy minimum. The next comparison should be the plaquette pairing state for the hole doped case, which is a very important conclusion readily predicted from the current variational study but not found in any mean field treatments. However, this might be due to the fact that the choice of such a state has been pre-excluded from the mean field studies by defining homogeneous pairings to start with (61). Here, an explicit check of such a plaquette state is carried out to help better clarify the inconsistencies between these two approaches.

By adapting conventions and notations from (61) and closely following derivations there, the $t-J$ Hamiltonian expressed in Eq. 4.3 gives the following grand canonical ensemble free energy for zero temperature

$$F = N\left[J\left(\left|\tilde{\Delta}_{x_1}\right|^2+\left|\tilde{\Delta}_{y_1}\right|^2+\left|\tilde{\Delta}_{x_2}\right|^2+\left|\tilde{\Delta}_{y_2}\right|^2\right)-2\left(\mu_0+\mu_1\right)+\frac{J'}{2}\left(\left|\tilde{\Delta}_{x-y}\right|^2+\left|\tilde{\Delta}_{x+y}\right|^2\right)\right] - \sum_{\mathbf{k},\epsilon_i}\epsilon_i\left(\mathbf{k}\right)\theta\left(\epsilon_i\left(\mathbf{k}\right)\right) \tag{4.25}$$

where N denotes total number of unit cells on the lattice, $\epsilon_i\left(\mathbf{k}\right)$ denotes positive eigenvalues calculated from the mean field Hamiltonian H_m, whose details can be found in Ref. (61), and the indication function $\theta\left(x\right)$ is defined as

$$\theta\left(x\right)=\begin{cases}0 & \text{for } x<0\\ 1 & \text{for } x>0\end{cases}. \tag{4.26}$$

$\tilde{\Delta}$ and μ_i are referred to Fig. 4.1. Here μ_i are used to give more freedom to adjust the charge density on the lattice and the following restrictions

$$\mu_0=\mu_2, \mu_1=\mu_3 \tag{4.27}$$

are applied in the above derivation.

A Legendre transformation is further applied to switch the free energy, F, into the canonical ensemble as

$$F_{can} = F + 2\sum_{i=0,1} N\mu_i \tag{4.28}$$

where $N = -\frac{1}{2}\left.\frac{\partial F}{\partial \mu_i}\right|_{\tilde{\Delta}}$. A minimization procedure is then applied onto F_{can} to get the optimal values for the relevant parameters. It immediately turns out that

$$\mu_0 = \mu_1$$

assuming no charge inhomogeneity in the problem. At the same time, by defining δ_e and δ_h to be the electron and hole doping concentrations, the results are shown in Fig. 4.13 which clearly shows nonexistence of plaquette phases.

Although for a $t-J$ Hamiltonian both methods give qualitatively consistent conclusions on a square lattice (17)(98), this doesn't seem to be the case on the SS lattice. A comparison indicates that the major conclusions from the mean field theory cannot be reproduced in the variational treatment, and vice versa. Additionally, this difference should not be attributed to the three-site hopping term ignored from Eq. 4.3 yet included in the simulation because this effect should be tiny for the case of small amounts of doping. As has been mentioned at the beginning of this chapter, we have more confidence in the results of the projected wavefunction as it better addresses the physics involved on the SS lattice, and it is able to give the exact ground state at zero doping. The totally different behaviors coming out of both approaches implies that the omitted quantum fluctuations in the mean field theory actually play a very important role in producing the correct physics for the doped SS lattice.

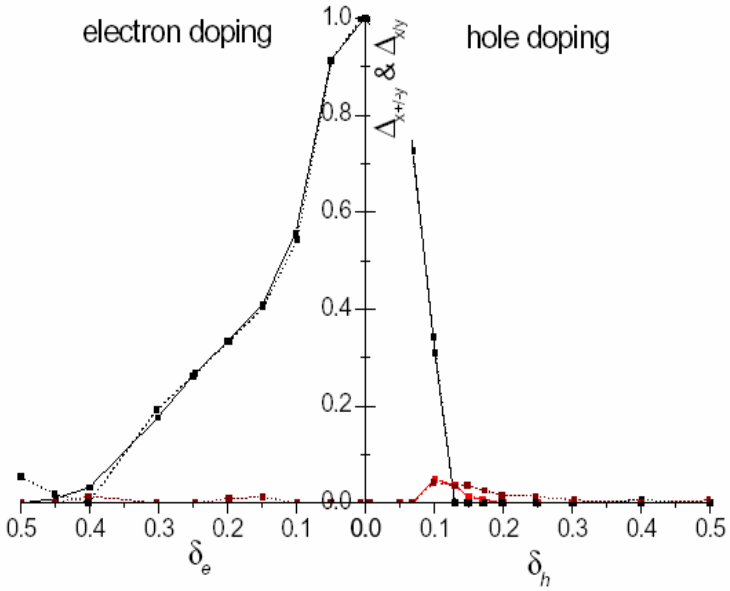

Figure 4.13 Results from the slave-boson mean field calculation are shown in this plot to check the existence of a plaquette d-wave pairing pattern for both doping cases. The solid curves are extracted from ref (61) with the plaquette phase turned off, while the dotted curves are results from the current simulation with the option turned on. The differences on several doping values between the calculation and the reference are checked to be due to either the finite size effect or existence of multiple local minima.

CHAPTER 5. Summary

In this thesis, the question studied was how the strong electron-electron (e-e) interaction and the existence of geometric frustration affect the physical properties of two materials, $\kappa - (\mathrm{ET})_2 Cu_2 (CN)_3$ and $SrCu_2 (BO_3)_2$, by using the Resonating Valence Bond (RVB) theory.

Strong e-e interaction and its related physics have been the focus of research in condensed matter physics for quite a long time. Among them are the Mott insulating and unconventional superconducting phenomena. A Mott insulator is such a material that would otherwise be predicted as a metal by the band theory, and is described well by the Hubbard model, the simplest model to describe strong e-e interaction in narrow band materials. An unconventional superconductor would have its pairing gaps to be anisotropic in real space, and thus cannot be explained by the conventional BCS theory. The proximity between these two states revealed in different experiments leads physicists to believe that deeper understanding of a Mott insulator might shed light on better interpretation on the unconventional superconductivity. Yet so far the relevant mechanisms are still under heavy debate. One major concern is whether the Mott insulator itself is relevant to the unconventional superconductivity, or the magnetic ordering which usually exists in the Mott insulating state plays the role, or both are equally important. This problem has been sharpened recently by the discovery of $\kappa - (\mathrm{ET})_2 Cu_2 (CN)_3$ with $T_c \approx 13.5$K. What is peculiar with this material is the existence of a nonmagnetic insulating ground state with gapless excitations. It can be tuned into a superconducting state with d-wave pairing under pressure. This feature prompts us to make use of the RVB picture to try to describe the physics involved because the picture contains the nonmagnetic ordering and the electron pairing in a natural way. Meanwhile, another material, $SrCu_2 (BO_3)_2$, attracts our attention because it has just been experimentally proved to have an isolated spin singlet

ground state. Under the RVB theory, the preformed pairing singlets would move upon doping and might give rise to superconductivity. This very interesting aspect of the RVB theory can thus be explicitly checked on this material. On the other hand, the material is close to quantum instability and thus rich physics are expected upon doping. Besides the strong e-e interaction, these two materials share one more thing in common that they are both of quasi-2 dimensional material.

As is mentioned above, the simplest model to describe the strong e-e interaction is the Hubbard model with nearby hopping amplitude, t, and strong on-site repulsion U. The large U limit gives the $t-J$ Hamiltonian where a virtual process takes place to exchange two electrons of opposite spins. This quick process has a bound doublon (doubly occupied site) -holon (empty site) state as its intermediate state and develops an energy gain of the order of t^2/U. Both of these two Hamiltonians are relevant in this work. A Hubbard model describes $\kappa-(\mathrm{ET})_2 Cu_2 (CN)_3$ with intermediate onsite repulsion U and strong diagonal hopping t', while a $t-J$ Hamiltonian describes $SrCu_2 (BO_3)_2$ with the existence of specific next nearest neighbor exchange interactions.

The trial wavefunction is generically a RVB state,

$$|\Psi_{RVB}\rangle = \hat{P}\,|\Phi_{BCS}\rangle \tag{5.1}$$

where $\hat{P}$ introduces into the system effects resulting from specific e-e interaction relevant to different problems, and $|\Phi_{BCS}\rangle$ is the specific underlying wavefunction to contain singlet pairing and nonmagnetic ordering. To $\kappa-(\mathrm{ET})_2 Cu_2 (CN)_3$, $\hat{P}$ includes a Gutzwiller projection, with parameter g, to account for the single occupation effects due to the large U and a Kaplan projection, with parameter h, to include the intermediate doublon-holon binding effects responsible for the $t-J$ physics. The underlying wavefunction is the usual single band BCS wavefunction. Explicitly, they are

$$\hat{P} = \prod_i g^{\hat{D}_i} h^{\hat{\Theta}_i} \tag{5.2}$$

$$|\Phi_{BCS}\rangle \propto \left(\sum_{\mathbf{k}} \phi_{\mathbf{k}} c^{\dagger}_{\mathbf{k},\uparrow} c^{\dagger}_{-\mathbf{k},\downarrow}\right)^N |0\rangle\,. \tag{5.3}$$

In case of $SrCu_2(BO_3)_2$, $\hat{P}$ is the full Gutzwiller projection to exclude electronic configurations with any doublons on them. The underlying wavefunction is now the multiband BCS wavefunction. Explicitly,

$$\hat{P} = \prod_i \left(1 - \hat{D}_i\right) \tag{5.4}$$

$$|\Phi_{BCS}\rangle \propto \left(\sum_{n,n',\mathbf{k}} h_{n,n'}(\mathbf{k})\, c^{\dagger}_{n,\mathbf{k},\uparrow} c^{\dagger}_{n',-\mathbf{k},\downarrow}\right)^N |0\rangle . \tag{5.5}$$

The necessary explanation of the notations can be found in chapter 2.

The variational parameters are contained in both $\hat{P}$ and $|\Phi_{BCS}\rangle$. The quantity to optimize the wavefunction is the energy expectation

$$\langle E\rangle = \frac{\langle \Psi_{RVB}|\, \hat{H}\, |\Psi_{RVB}\rangle}{\langle \Psi_{RVB}|\Psi_{RVB}\rangle} \tag{5.6}$$

which can be re-expressed in statistical language as a mean of some local energy with a specific distribution function closely related to $|\Psi_{RVB}\rangle$. The Metropolis algorithm is used to generate the distribution in the $2N$ dimensional discrete lattice space. It is also used to locate energy minimum in the variational phase space. A simple yet very efficient algorithm is introduced to help generate the distribution and improve the simulated annealing algorithm.

For the organic superconductor, $\kappa - (ET)_2 Cu_2 (CN)_3$, here is the summary of the major results.

- The overall phase diagram was determined as a function of the onsite repulsion U. Around $U_{c_1} \approx 8.5$, there exists a strong d-wave superconducting state sandwiched between a metallic state and a spin liquid state. The transition is sharp from the superconducting state to the metallic state, but is smooth to the spin liquid state. This is in qualitative agreement with experiments yet the trend is opposite. The difference has been identified to be due to the same treatment to doublon holon binding in all directions in real space.

- A d-wave pairing state quickly develops as U increases beyond U_{c_1}. As U passes over $U_{c_2} \approx 9.0$, the system enters a spin liquid state where the $t-J$ physics plays a more and

more important role. The tiny yet finite ODLRO there is believed to be an artifact of the trial wavefunction itself.

- At $U \approx U_{c_1}$, the excitation spectrum begins to deviate from the bare dispersion. This is thought to be caused by absorbing the strong onsite repulsion into quasiparticles. The resulting deviation becomes more serious as U increases even further. The excitation spectrum is reformed to be more symmetric in momentum space, which is also supported by the charge density $n_{\mathbf{k}}$. This effect is thought to partially contribute to the unconventional superconducting behavior.

- The spacial dependence of the magnetic correlation is dramatically different between the metallic state and the spin liquid state. This difference can be explained by the strong deformation on the excitation spectrum of the quasiparticles. Especially, the reduced effective diagonal hoppings in the spin liquid state readily give very similar magnetic correlation along the two diagonal directions.

For $SrCu_2\left(BO_3\right)_2$, here is the summary of the major conclusions.

- The trial RVB wavefunction constructed from the multiband BCS wavefunction is able to give the exact ground state energy for the undoped system. This shows that the wavefunction is able to capture the physics coming from the specific lattice structure. It implies that the current approach is particularly well controlled for small doping.

- By fitting a tight binding model to a first principle calculation of the band structure coming out of the actual material, the signs of the bare hoppings are identified: $t' > 0$, yet the sign of t is irrelevant.

- Because the $t - J$ Hamiltonian for this material suppresses completely doubly occupied sites, electron doping cannot be trivially treated by adding more electrons into the system. A specific particle-hole transformation is introduced to show that the electron doped case can be equivalently mapped to a hole doped problem whose t' is opposite to that of the actual lattice.

- Nearly homogeneous charge distribution is found on the lattice for both doping cases. This is supported by a charge inhomogeneity of 0.1%. This is also reassuring and allows one to ignore the Coulomb interaction between nearby sites out of the model Hamiltonian. However for the hole doped case, the variational chemical potentials are significantly different within a unit cell. Together with the similar trend expected for a true chemical potential as doping increases, this shows that the variational chemical potentials are not the true chemical potential but are related to it.

- Dramatically different physics are found between both doping cases. This is understandable by noticing that t' is the dominant energy scale in the problem. The electron or hole doping literally corresponds to results with different sign in t'.

- In the hole doped system, many physical quantities support a possible existence of a phase transition around $\delta_h^c = 2.5\%$. For $\delta > \delta_h^c$, they support the existence of the plaquette d-wave pairing state where the strongest pairings are around unit cells with reduced effective diagonal hoppings inside. This strongly supports the idea that the electrons totally re-organize themselves to delocalize along the lateral directions. This is totally different from the observed behavior in the parent compound.

- In the hole doped system, the ODLRO is strongly enhanced due to the plaquette pairing pattern as compared to the state with homogeneous d-wave pairing. This is partially understood by the efficient tunnelling of electron pairs between nearby enhanced superconducting islands when the coherence length is comparable to the inhomogeneity distance, which is the case here.

- In the hole doped system, the magnetic correlation is very similar to that of the parent compound for small amounts of doping, then it dramatically changes to be antiferromagnetic to all the nearest and next nearest neighboring sites as doping increases. Among those neighboring sites, the nearest ones along the x and y axes are stronger. This magnetic correlation pattern is readily understood from the plaquette d-wave pairing pattern.

- The existence of multiple local energy minima affects the analysis for both doping cases. But it affects more in the case of electron doped systems because these minima are close in energy. However, very strangely, these minima all give very similar physical observables.

- In the electron doped system, effective diagonal hoppings are strongly enhanced as compared to the bare hopping parameters. This is understood to show that electrons still have the tendency to be localized along the diagonal bonds. But it is not as strong as the undoped material.

- In the electron doped system, the pairing strengths are different for different local minima. Nonetheless, they all give a vanishing ODLRO within an error of 10^{-4}. Meanwhile, the low frequency Drude weight, D_{low}, is calculated and shows that the electron doped system is conducting. Together with the significant magnetic correlations along specific diagonal directions, this shows that the electron doped material is a strange metal if not due to an artifact of the wavefunction.

- In the electron doped system, the magnetic correlation is very much like that of the parent compound. This, together with the doping dependence of $\chi_{0,x}$, implies that the singlets along specific diagonal directions are still responsible in majority for the electron doped material. The doublons are scattered around the system, isolated from each other.

- Slave Boson mean field treatment is carried out on this system with the option of plaquette pairing being enabled. The optimization automatically gives the diagonal pairings as the most significant pairings for both doping cases. This is totally inconsistent with the current simulation. Another contradiction between both approaches is the existence of the π flux phase in the electron doped case. The mean field study predicted it while the current study disapproves it. Considering that the current RVB state treats the strong e-e interaction physics correctly, and reproduces the exact ground state in the parent compound, the current simulation is believed to be more reliable than the slave boson mean field treatment. This implies that the quantum fluctuation ignored in the mean field treatment is very important in capturing the correct physics of $SrCu_2\left(BO_3\right)_2$.

APPENDIX A. Multiband BCS pairing amplitude in momentum space

In this appendix, it contains a detailed derivation of the multiband BCS pairing amplitude in momentum space. The validity of the obtained result can be seen by collapsing to the standard BCS pairing amplitude when each unit cell becomes simple. The derivation is not confined to specific unit cell structure. Different unit cells would only change the matrices for T and D to be explained shortly. The Hamiltonian to start with is the standard $t-J$ Hamiltonian, which contains singlet pairing in a natural way.

The major steps are outlined here. First, mean field decoupling is applied to the interacting $t-J$ Hamiltonian in real space. Then diagonalization of the mean field decoupled Hamiltonian gives the annihilation operators for the problem. Next, an explicit expression is guessed for the ground state wavefunction and the annihilation operators are required to make it vanishing. This finally gives the expression for the pairing amplitude in momentum space. The following is a detailed account of the derivation on the SS lattice, yet the extension to other lattice is straightforward.

$t-J$ Hamiltonian and its mean field decomposition On the SS lattice, $t-J$ Hamiltonian can be written as, with all indices written out explicitly,

$$\begin{aligned}\hat{H}^{t-J} &= \hat{H}_k + \hat{H}' \\ &= -\sum_{\mathbf{R}_i,\mathbf{R}_j;r_\alpha,r_\beta} t^{r_\alpha,r_\beta}_{\mathbf{R}_i,\mathbf{R}_j}\tilde{c}^\dagger_{\mathbf{R}_i,r_\alpha;\sigma}\tilde{c}_{\mathbf{R}_j,r_\beta;\sigma} \\ &+ \sum_{\mathbf{R}_i,\mathbf{R}_j;r_\alpha,r_\beta} J^{r_\alpha,r_\beta}_{\mathbf{R}_i,\mathbf{R}_j}\left(\hat{\mathbf{S}}^{r_\alpha}_{\mathbf{R}_i}\cdot\hat{\mathbf{S}}^{r_\beta}_{\mathbf{R}_j} - \frac{n_{\mathbf{R}_i,r_\alpha}n_{\mathbf{R}_j,r_\beta}}{4}\right) \end{aligned} \tag{A.1}$$

where $\tilde{c}_{i,\sigma} = c_{i,\sigma}\left(1 - n_{i,\bar{\sigma}}\right)$ and $t^{r_\alpha, r_\beta}_{\mathbf{R}_i,\mathbf{R}_j}, J^{r_\alpha, r_\beta}_{\mathbf{R}_i,\mathbf{R}_j}$ are defined along specific links between two sites. Specifically,

$$t^{r_\alpha, r_\beta}_{\mathbf{R}_i,\mathbf{R}_j} = t \text{ and } J^{r_\alpha, r_\beta}_{\mathbf{R}_i,\mathbf{R}_j} = J$$

if $(\mathbf{R}_i, r_\alpha), (\mathbf{R}_j, r_\beta)$ are nearest neighbor sites and

$$t^{r_\alpha, r_\beta}_{\mathbf{R}_i,\mathbf{R}_j} = t' = \alpha t \text{ and } J^{r_\alpha, r_\beta}_{\mathbf{R}_i,\mathbf{R}_j} = J' = \alpha^2 J$$

if $(\mathbf{R}_i, r_\alpha), (\mathbf{R}_j, r_\beta)$ are next nearest neighbor sites. The $\hat{\mathbf{S}}$ is the spin operator in the fermionic representation and is defined as

$$\hat{\mathbf{S}}_i = \frac{1}{2}\sum_{\sigma,\sigma'} c^\dagger_{i\sigma}\tau_{\sigma,\sigma'}c_{i\sigma'} \tag{A.2}$$

where τ are the Pauli matrices. Other related spin operators are defined as

$$S^\dagger_i = S_{i,x} + iS_{i,y} = c^\dagger_{i,\uparrow}c_{i,\downarrow} = \left(S^-_i\right)^\dagger \tag{A.3}$$

$$S_{i,z} = \frac{1}{2}\left(n_{i,\uparrow} - n_{i,\downarrow}\right) \tag{A.4}$$

Before the Fourier transformation is carried out on particle operators, some notations are listed below if only brief.

- Unit lattice constant, a, is assumed to be 1, thus unit length of the corresponding Bravais lattice is $A = 2a = 2$.
- Unit vectors of the lattice are denoted as $\hat{x}, \hat{y}$ and $|\hat{x}| = |\hat{y}| = a = 1$. Vectors between the nearest neighbors on the Bravais lattice are denoted as $\hat{X}, \hat{Y}$ with $\left|\hat{X}\right| = \left|\hat{Y}\right| = 2a = 2$.
- The x and y components of quasimomenta are defined as $k_{X/Y} = \dfrac{2n\pi}{NA} = \dfrac{n\pi}{Na}$ for $n = 0, 1, 2, ...N-1$.Thus $\mathbf{k}\cdot\hat{x} = k_x$ while $\mathbf{k}\cdot\vec{X} = 2k_x$.
- Atomic indices in the unit cell is labeled by $0, 1, 2, 3$ with 0 at the left lower corner, 1 at the right lower corner, 2 at the left upper corner and 3 at the right upper corner. The existing diagonal hopping is from site 0 of the current unit cell to site 3 of the unit cell to the right.

The Fourier transformation is defined as

$$a_{\mathbf{k},r;\sigma} = \frac{1}{\sqrt{N}} \sum_{\mathbf{R}_i} c_{\mathbf{R}_i,r;\sigma} e^{i\mathbf{k}\cdot(\mathbf{R}_i+\delta_r)} \Leftrightarrow c_{\mathbf{R}_i,r;\sigma} = \frac{1}{\sqrt{N}} \sum_{\mathbf{k}} a_{\mathbf{k},r;\sigma} e^{-i\mathbf{k}\cdot(\mathbf{R}_i+\delta_r)}. \tag{A.5}$$

Here $r \in \{0,1,2,3\}$ as site label, N denotes number of unit cells on the Bravais lattice and δ_r is any additional phase factor to each site, which is introduced for convenience. The kinetic term of $\hat{H}^{t-J}$, $\hat{H}_k$, can be re-expressed as

$$\hat{H}_k = -\sum_{\mathbf{k},\sigma} \Psi_\sigma^\dagger(\mathbf{k})\, T(\mathbf{k},\delta)\, \Psi_\sigma(\mathbf{k}) \tag{A.6}$$

with

$$\Psi_\sigma(\mathbf{k}) = \begin{pmatrix} a_{0,\sigma}(\mathbf{k}) \\ a_{1,\sigma}(\mathbf{k}) \\ a_{2,\sigma}(\mathbf{k}) \\ a_{3,\sigma}(\mathbf{k}) \end{pmatrix} \tag{A.7}$$

and

$$\begin{aligned} &T(\mathbf{k},\delta) \\ &= t \begin{pmatrix} 0 & \varpi_{01}\left(1+e^{i\mathbf{k}\cdot X}\right) & \varpi_{02}\left(1+e^{i\mathbf{k}\cdot Y}\right) & \alpha\varpi_{03}e^{i\mathbf{k}\cdot X} \\ \varpi_{10}\left(1+e^{-i\mathbf{k}\cdot X}\right) & 0 & \alpha\varpi_{12}e^{i\mathbf{k}\cdot Y} & \varpi_{13}\left(1+e^{i\mathbf{k}\cdot Y}\right) \\ \varpi_{20}\left(1+e^{-i\mathbf{k}\cdot Y}\right) & \alpha\varpi_{21}e^{-i\mathbf{k}\cdot Y} & 0 & \varpi_{23}\left(1+e^{i\mathbf{k}\cdot X}\right) \\ \alpha\varpi_{30}e^{-i\mathbf{k}\cdot X} & \varpi_{31}\left(1+e^{-i\mathbf{k}\cdot Y}\right) & \varpi_{32}\left(1+e^{-i\mathbf{k}\cdot X}\right) & 0 \end{pmatrix} \end{aligned} \tag{A.8}$$

where $\varpi_{ij} = e^{ik\cdot(\delta_i-\delta_j)}$ is introduced to shorten the expression. By choosing zero phase convention

$$\delta_0 = \delta_1 = \delta_2 = \delta_3 = 0,$$

$T(\mathbf{k},\delta)$ would be

$$T(\mathbf{k}) = t \begin{pmatrix} 0 & 1+e^{i\mathbf{k}\cdot X} & 1+e^{i\mathbf{k}\cdot Y} & \alpha e^{i\mathbf{k}\cdot X} \\ 1+e^{-i\mathbf{k}\cdot X} & 0 & \alpha e^{i\mathbf{k}\cdot Y} & 1+e^{i\mathbf{k}\cdot Y} \\ 1+e^{-i\mathbf{k}\cdot Y} & \alpha e^{-i\mathbf{k}\cdot Y} & 0 & 1+e^{i\mathbf{k}\cdot X} \\ \alpha e^{-i\mathbf{k}\cdot X} & 1+e^{-i\mathbf{k}\cdot Y} & 1+e^{-i\mathbf{k}\cdot X} & 0 \end{pmatrix} \tag{A.9}$$

and by choosing symmetric phase convention

$$\delta_0 = 0,\ \delta_1 = \hat{x},\ \delta_2 = \hat{y},\ \delta_3 = \hat{x} + \hat{y},$$

$T(\mathbf{k}, \delta)$ would be

$$T(\mathbf{k}) = \begin{pmatrix} 0 & 2t\cos k_x & 2t\cos k_y & t'e^{i(k_x - k_y)} \\ 2t\cos k_x & 0 & t'e^{i(k_x + k_y)} & 2t\cos k_y \\ 2t\cos k_y & t'e^{-i(k_x + k_y)} & 0 & 2t\cos k_x \\ t'e^{-i(k_x - k_y)} & 2t\cos k_y & 2t\cos k_x & 0 \end{pmatrix} \tag{A.10}$$

The interacting term, $\hat{H}'$, is chosen to be decomposed in the pairing channel in the mean field treatment. By making use of the fermionic representation for spin operators in Eq. A.2, it is not hard to check that $\hat{H}'$ can be re-expressed as a direct product of two singlet operators

$$\begin{aligned} \hat{H}' &= \sum_{\mathbf{R}_i, \mathbf{R}_j; r_\alpha, r_\beta} J^{r_\alpha, r_\beta}_{\mathbf{R}_i, \mathbf{R}_j} \left(\hat{\mathbf{S}}^{r_\alpha}_{\mathbf{R}_i} \cdot \hat{\mathbf{S}}^{r_\beta}_{\mathbf{R}_j} - \frac{n_{\mathbf{R}_i, r_\alpha} n_{\mathbf{R}_j, r_\beta}}{4} \right) \\ &= \sum_{\mathbf{R}_i, \mathbf{R}_j; r_\alpha, r_\beta} J^{r_\alpha, r_\beta}_{\mathbf{R}_i, \mathbf{R}_j} \left(-\frac{1}{2} \mathcal{B}^\dagger_{(\mathbf{R}_i, r_\alpha), (\mathbf{R}_j, r_\beta)} \mathcal{B}_{(\mathbf{R}_i, r_\alpha), (\mathbf{R}_j, r_\beta)} \right) \end{aligned} \tag{A.11}$$

with

$$\mathcal{B}_{(\mathbf{R}_i, r_\alpha), (\mathbf{R}_j, r_\beta)} = \tilde{c}_{\mathbf{R}_i, r_\alpha; \downarrow} \tilde{c}_{\mathbf{R}_j, r_\beta; \uparrow} - \tilde{c}_{\mathbf{R}_i, r_\alpha; \uparrow} \tilde{c}_{\mathbf{R}_j, r_\beta; \downarrow} \tag{A.12}$$

$$\mathcal{B}^\dagger_{(\mathbf{R}_i, r_\alpha), (\mathbf{R}_j, r_\beta)} = \tilde{c}^\dagger_{\mathbf{R}_j, r_\beta; \uparrow} \tilde{c}^\dagger_{\mathbf{R}_i, r_\alpha; \downarrow} - \tilde{c}^\dagger_{\mathbf{R}_j, r_\beta; \downarrow} \tilde{c}^\dagger_{\mathbf{R}_i, r_\alpha; \uparrow} = \left(\mathcal{B}_{(\mathbf{R}_i, r_\alpha), (\mathbf{R}_j, r_\beta)} \right)^\dagger . \tag{A.13}$$

where $(\mathbf{R}_i, r_\alpha) \neq (\mathbf{R}_j, r_\beta)$ is assumed. Now introduce mean field pairing as

$$\left\langle \mathcal{B}_{(\mathbf{R}_i, r_\alpha), (\mathbf{R}_j, r_\beta)} \right\rangle = \begin{cases} \Delta_x \text{ if } (\mathbf{R}_i, r_\alpha) - (\mathbf{R}_j, r_\beta) = \hat{x} \\ \Delta_y \text{ if } (\mathbf{R}_i, r_\alpha) - (\mathbf{R}_j, r_\beta) = \hat{y} \\ \Delta_{x+y} \text{ if } (\mathbf{R}_i, r_\alpha) - (\mathbf{R}_j, r_\beta) = \hat{x} + \hat{y} \\ \Delta_{x-y} \text{ if } (\mathbf{R}_i, r_\alpha) - (\mathbf{R}_j, r_\beta) = \hat{x} - \hat{y} \end{cases} , \tag{A.14}$$

and drop the single occupation restriction on each site and possible constant energy term, and I get

$$\hat{H}' = -\sum_{\mathbf{R}_i, \mathbf{R}_j; r_\alpha, r_\beta} \frac{J^{r_\alpha, r_\beta}_{\mathbf{R}_i, \mathbf{R}_j}}{2} \left\langle \mathcal{B}_{(\mathbf{R}_i, r_\alpha), (\mathbf{R}_j, r_\beta)} \right\rangle^* \left(c_{\mathbf{R}_i, r_\alpha; \downarrow} c_{\mathbf{R}_j, r_\beta; \uparrow} - c_{\mathbf{R}_i, r_\alpha; \uparrow} c_{\mathbf{R}_j, r_\beta; \downarrow} \right) + h.c., \tag{A.15}$$

the Hamiltonian decomposed in the singlet pairing channel. The Fourier transformation in Eq. A.5 can be further applied onto the above expression and gives, in the matrix notation,

$$\hat{H}' = -\sum_{\mathbf{k}} \left(\Psi_{\downarrow}^{T}(-\mathbf{k})\, D^{\dagger}(\mathbf{k})\, \Psi_{\uparrow}(\mathbf{k}) + h.c. \right) \tag{A.16}$$

with

$$D(\mathbf{k},\delta) = \frac{J}{2} \begin{pmatrix} 0 & \Delta_x \varpi_{01} \Theta_X & \Delta_y \varpi_{02} \Theta_Y & \alpha^2 \Delta_{x-y} \varpi_{03} e^{i\mathbf{k}\cdot X} \\ \Delta_x \varpi_{10} \Theta_X^* & 0 & \alpha^2 \varpi_{12} \Delta_{x+y} e^{i\mathbf{k}\cdot Y} & \Delta_y \varpi_{13} \Theta_Y \\ \Delta_y \varpi_{20} \Theta_Y^* & \alpha^2 \Delta_{x+y} \varpi_{21} e^{-i\mathbf{k}\cdot Y} & 0 & \Delta_x \varpi_{23} \Theta_X \\ \alpha^2 \Delta_{x-y} \varpi_{30} e^{-i\mathbf{k}\cdot X} & \Delta_y \varpi_{31} \Theta_Y^* & \Delta_x \varpi_{32} \Theta_X^* & 0 \end{pmatrix}$$

where $\Theta_{\delta\mathbf{r}} = 1 + e^{i\mathbf{k}\cdot\delta\mathbf{r}}$ with the same ϖ_{ij} used here. By choosing zero phase convention

$$\delta_0 = \delta_1 = \delta_2 = \delta_3 = 0,$$

$D(\mathbf{k},\delta)$ would be

$$D(\mathbf{k}) = \frac{J}{2} \begin{pmatrix} 0 & \Delta_x \left(1 + e^{i\mathbf{k}\cdot X}\right) & \Delta_y \left(1 + e^{i\mathbf{k}\cdot Y}\right) & \alpha^2 \Delta_{x-y} e^{i\mathbf{k}\cdot X} \\ \Delta_x \left(1 + e^{-i\mathbf{k}\cdot X}\right) & 0 & \alpha^2 \Delta_{x+y} e^{i\mathbf{k}\cdot Y} & \Delta_y \left(1 + e^{i\mathbf{k}\cdot Y}\right) \\ \Delta_y \left(1 + e^{-i\mathbf{k}\cdot Y}\right) & \alpha^2 \Delta_{x+y} e^{-i\mathbf{k}\cdot Y} & 0 & \Delta_x \left(1 + e^{i\mathbf{k}\cdot X}\right) \\ \alpha^2 \Delta_{x-y} e^{-i\mathbf{k}\cdot X} & \Delta_y \left(1 + e^{-i\mathbf{k}\cdot Y}\right) & \Delta_x \left(1 + e^{-i\mathbf{k}\cdot X}\right) & 0 \end{pmatrix} \tag{A.17}$$

and by choosing symmetric phase convention

$$\delta_0 = 0,\ \delta_1 = \hat{x},\ \delta_2 = \hat{y},\ \delta_3 = \hat{x} + \hat{y},$$

$D(\mathbf{k},\delta)$ would be

$$D(\mathbf{k}) = J \begin{pmatrix} 0 & \Delta_x \cos k_x & \Delta_y \cos k_y & \frac{\alpha^2}{2} \Delta_{x-y} e^{i\theta_-} \\ \Delta_x \cos k_x & 0 & \frac{\alpha^2}{2} \Delta_{x+y} e^{i\theta_+} & \Delta_y \cos k_y \\ \Delta_y \cos k_y & \frac{\alpha^2}{2} \Delta_{x+y} e^{-i\theta_+} & 0 & \Delta_x \cos k_x \\ \frac{\alpha^2}{2} \Delta_{x-y} e^{-i\theta_-} & \Delta_y \cos k_y & \Delta_x \cos k_x & 0 \end{pmatrix} \tag{A.18}$$

with $\theta_{\pm} = k_x \pm k_y$.

When both $\hat{H}_k$ and $\hat{H}'$ are summarized here together with the chemical potential to each site, the final mean field Hamiltonian is obtained in matrix notation,

$$\begin{aligned}\hat{H}^{mf} &= -\sum_{\mathbf{k}} \begin{pmatrix} \Psi_{\uparrow}^{\dagger}(\mathbf{k}) & \Psi_{\downarrow}^{T}(-\mathbf{k}) \end{pmatrix} \begin{pmatrix} T_{\mu}(\mathbf{k}) & D(\mathbf{k}) \\ D^{\dagger}(\mathbf{k}) & -T_{\mu}^{T}(-\mathbf{k}) \end{pmatrix} \begin{pmatrix} \Psi_{\uparrow}(\mathbf{k}) \\ \left(\Psi_{\downarrow}^{T}(-\mathbf{k})\right)^{\dagger} \end{pmatrix} \\ &= -\sum_{\mathbf{k}}^{\dagger} \ominus^{\dagger}(\mathbf{k}) H_m \ominus(\mathbf{k}) \end{aligned} \tag{A.19}$$

where

$$\ominus(\mathbf{k}) = \begin{pmatrix} \Psi_{\uparrow}(\mathbf{k}) \\ \left(\Psi_{\downarrow}^{T}(-\mathbf{k})\right)^{\dagger} \end{pmatrix} \tag{A.20}$$

and

$$T_{\mu}(\mathbf{k}) = T(\mathbf{k}) + \begin{pmatrix} \mu_0 & 0 & 0 & 0 \\ 0 & \mu_1 & 0 & 0 \\ 0 & 0 & \mu_2 & 0 \\ 0 & 0 & 0 & \mu_3 \end{pmatrix} \tag{A.21}$$

Quasiparticle creation/annihilation operators from H^{mf} and guessed ground state wavefunction To be physically transparent for inter- and intra-band pairing, it is preferred to transform $\hat{H}^{mf}$ into the band⊕momentum representation. The band representation is obtained by diagonalizing $T(\mathbf{k})$ with a unitary matrix $W(\mathbf{k})$

$$W^{\dagger}(\mathbf{k}) T(\mathbf{k}) W(\mathbf{k}) = \begin{pmatrix} \epsilon_0 & 0 & 0 & 0 \\ 0 & \epsilon_1 & 0 & 0 \\ 0 & 0 & \epsilon_2 & 0 \\ 0 & 0 & 0 & \epsilon_3 \end{pmatrix} = E(\mathbf{k}) \tag{A.22}$$

with

$$W^{\dagger}(\mathbf{k}) W(\mathbf{k}) = I_{4\times 4}. \tag{A.23}$$

By defining the band representation to be

$$b_{\mathbf{k},n;\sigma} = \sum_{r=0}^{m-1} w_{r,n}^{*}(\mathbf{k}) a_{\mathbf{k},r;\sigma} = \frac{1}{\sqrt{N}} \sum_{r=0}^{m-1} \sum_{\mathbf{R}_i} w_{r,n}^{*}(\mathbf{k}) c_{\mathbf{R}_i,r;\sigma} e^{i\mathbf{k}\cdot(\mathbf{R}_i+\delta_r)} \tag{A.24}$$

for $n = 0, ..., m-1$ with $m = 4$, four atoms in each unit cell, $\hat{H}^{mf}$ can be written in the band⊕momentum representation as

$$\hat{H}^{mf} = -\sum_{\mathbf{k}} \begin{pmatrix} Y_{\uparrow}^{\dagger}(\mathbf{k}) & Y_{\downarrow}^{T}(-\mathbf{k}) \end{pmatrix} \begin{pmatrix} T_{W,\mu}(\mathbf{k}) & D_W(\mathbf{k}) \\ D_W^{\dagger}(\mathbf{k}) & -T_{W,\mu}(-\mathbf{k}) \end{pmatrix} \begin{pmatrix} Y_{\uparrow}(\mathbf{k}) \\ \left(Y_{\downarrow}^{T}(-\mathbf{k})\right)^{\dagger} \end{pmatrix} \quad (A.25)$$

with $Y_{\sigma}(\mathbf{k})$ defined similarly as

$$Y_{\sigma}(\mathbf{k}) = \begin{pmatrix} b_{0,\sigma}(\mathbf{k}) \\ b_{1,\sigma}(\mathbf{k}) \\ b_{2,\sigma}(\mathbf{k}) \\ b_{3,\sigma}(\mathbf{k}) \end{pmatrix} = W^{\dagger}(\mathbf{k}) \Psi_{\sigma}(\mathbf{k}) \quad (A.26)$$

and

$$T_{W,\mu}(\mathbf{k}) = W^{\dagger}(\mathbf{k}) T(\mathbf{k}) W(\mathbf{k}) \quad (A.27)$$

$$D_W(\mathbf{k}) = W^{\dagger}(\mathbf{k}) D(\mathbf{k}) W^{*}(-\mathbf{k}). \quad (A.28)$$

Let us suppose that H^{mf} can be diagonalized by a unitary matrix

$$U(\mathbf{k}) = \begin{pmatrix} \hat{u}^{\dagger} & \hat{w} \\ -\hat{v}^{\dagger} & \hat{\varkappa} \end{pmatrix} (\mathbf{k}) \quad (A.29)$$

where $\hat{u}, \hat{v}, \hat{w}, \hat{\varkappa}$ are $m \times m$ matrices, such that

$$U^{\dagger} H^{mf} U = \begin{pmatrix} E^{mf} > 0 & 0 \\ 0 & -E^{mf} < 0 \end{pmatrix}, \quad (A.30)$$

where E^{mf} is a real positive diagonal matrix. The existence of these paired eigenvalues is mentioned in Ref. (61) in terms of sympletic matrices. Then U gives quasiparticle creation/annihilation operators

$$Z(\mathbf{k}) = \begin{pmatrix} z_i(\mathbf{k}) \\ \left(z_j^{T}(-\mathbf{k})\right)^{\dagger} \end{pmatrix} = \begin{pmatrix} \hat{u} & -\hat{v} \\ \hat{w}^{\dagger} & \hat{\varkappa}^{\dagger} \end{pmatrix} \begin{pmatrix} Y_{\uparrow}(\mathbf{k}) \\ \left(Y_{\downarrow}^{T}(-\mathbf{k})\right)^{\dagger} \end{pmatrix} \quad (A.31)$$

or explicitly

$$z_{t=0,1,..,m-1}(\mathbf{k}) = \sum_{n=0}^{m-1} \left(\hat{u}_{t,n}(\mathbf{k}) b_{n;\uparrow}(\mathbf{k}) - \hat{v}_{t,n}(\mathbf{k}) b_{n;\downarrow}^{\dagger}(-\mathbf{k}) \right) \quad (A.32)$$

$$z_{t=m,m+1,...,2m-1}(-\mathbf{k}) = \sum_{n=0}^{m-1} \left(\hat{w}_{n,t-m} b_{n;\uparrow}^{\dagger}(\mathbf{k}) + \hat{\varkappa}_{n,t-m} b_{n;\downarrow}(-\mathbf{k}) \right). \quad (A.33)$$

It is noticeable that annihilation operators are related with positive eigenvalues. This is because a creation operator for quasiparticles should satisfy

$$\left[H^{mf}, z^{\dagger}\right] = \Omega z^{\dagger} \tag{A.34}$$

with $\Omega > 0$.

But applying $Z^{\dagger}(\mathbf{k})$ onto $|0\rangle$, the electron vacuum state, would not give the expected ground state for the quasiparticles although $Z^{\dagger}(\mathbf{k})$ is still fermionic. This is because it contains annihilation operators for electrons and thus the resulting state is ill-defined. In order to get the ground state for H^{mf}, an appropriate functional form needs to be guessed and then vanishes by letting $Z(\mathbf{k})$ act on it. This, following the derivation of the single band BCS wavefunction (99), is guessed to be

$$\left|\psi^{trial}\right\rangle \propto \exp\left(\sum_{n_1,n_2,\mathbf{k}} h_{n_1,n_2}(\mathbf{k})\, b^{\dagger}_{n_1,\uparrow}(\mathbf{k})\, b^{\dagger}_{n_2,\downarrow}(-\mathbf{k})\right)|0\rangle \tag{A.35}$$

$$\propto \prod_{n_1,n_2;\mathbf{k}} \left(1 + h_{n_1,n_2}(\mathbf{k})\, b^{\dagger}_{n_1,\uparrow}(\mathbf{k})\, b^{\dagger}_{n_2,\downarrow}(-\mathbf{k})\right)|0\rangle\,, \tag{A.36}$$

where $h_{n_1,n_2}(\mathbf{k})$ defines the pairing amplitude between electrons of opposite spins at $(n_1,\mathbf{k})$ and $(n_2,-\mathbf{k})$. By choosing the wavefunction this way, intra- and inter-band pairings are delt with on the same footing as long as n denotes band index. However, the nature of the pairing cannot be determined at the time although it is presumably a spin singlet.

pairing amplitude in momentum space The guessed multiband BCS wavefunction in Eq. A.35 can be written as

$$\left|\psi^{trial}\right\rangle \propto \sum_{n=0}^{\infty} \frac{\tilde{\phi}^n}{n!}\ |0\rangle \tag{A.37}$$

with

$$\tilde{\phi} = \sum_{\mathbf{k},n_1,n_2} h_{n_1,n_2}(\mathbf{k})\, b^{\dagger}_{\mathbf{k},n_1,\uparrow} b^{\dagger}_{-\mathbf{k},n_2,\downarrow}. \tag{A.38}$$

By direct calculation, it can be verified that

$$\left[b_{\mathbf{k},n,\uparrow}, \tilde{\phi}\right] = g^{\dagger}_{\mathbf{k},n,\downarrow} \tag{A.39}$$

with operator

$$g^{\dagger}_{\mathbf{k},n,\downarrow} = \sum_{n_2} h_{n,n_2}(\mathbf{k})\, b^{\dagger}_{-\mathbf{k},n_2,\downarrow} \tag{A.40}$$

which obviously obeys $\left[g^{\dagger}_{\mathbf{k},n,\downarrow}, \tilde{\phi}\right] = 0$. Apply $b_{\mathbf{k},n,\uparrow}$ to each term in the sum of Eq. A.37 and I can get

$$b_{\mathbf{k},n,\uparrow}\tilde{\phi}\,|0\rangle = g^{\dagger}_{\mathbf{k},n,\downarrow}\,|0\rangle \tag{A.41}$$

$$b_{\mathbf{k},n,\uparrow}\tilde{\phi}^2\,|0\rangle = g^{\dagger}_{\mathbf{k},n,\downarrow}\tilde{\phi}\,|0\rangle + \tilde{\phi} b_{\mathbf{k},n,\uparrow}\tilde{\phi}\,|0\rangle = 2\tilde{\phi} g^{\dagger}_{\mathbf{k},n,\downarrow}\,|0\rangle \tag{A.42}$$

$$\vdots$$

$$b_{\mathbf{k},n,\uparrow}\tilde{\phi}^n\,|0\rangle = n\tilde{\phi}^{n-1} g^{\dagger}_{\mathbf{k},n,\downarrow}\,|0\rangle\,. \tag{A.43}$$

This result allows to resum the series Eq. A.37 and it gives

$$b_{\mathbf{k},n,\uparrow}\left|\psi^{trial}\right\rangle = g^{\dagger}_{\mathbf{k},n,\downarrow}\left|\psi^{trial}\right\rangle. \tag{A.44}$$

The condition $z_t(\mathbf{k})\left|\psi^{trial}\right\rangle = 0$, $t = 0, 1, ..., m-1$, can then be written as

$$\sum_{n=0}^{m-1}\sum_{n'=0}^{m-1} \hat{u}_{t,n'}(\mathbf{k})\, h_{n',n}(\mathbf{k})\left(b^{\dagger}_{-\mathbf{k},n,\downarrow}\left|\psi^{trial}\right\rangle\right) - \sum_{n=0}^{m-1}\hat{v}_{t,n}(\mathbf{k})\left(b^{\dagger}_{-\mathbf{k},n;\downarrow}\left|\psi^{trial}\right\rangle\right) = 0 \tag{A.45}$$

or equivalently

$$\sum_{n'=0}^{m-1}\hat{u}_{t,n'}(\mathbf{k})\, h_{n',n}(\mathbf{k}) = \hat{v}_{t,n}(\mathbf{k})\,. \tag{A.46}$$

In matrix notation this implies immediately

$$\varrho = \hat{u}^{-1}\cdot\hat{v}. \tag{A.47}$$

Similarly I can introduce

$$j^{\dagger}_{-\mathbf{k},n;\uparrow} = -\sum_{n_1} h_{n_1,n}(\mathbf{k})\, b^{\dagger}_{\mathbf{k},n_1,\uparrow} \tag{A.48}$$

which satisfies

$$\left[b_{-\mathbf{k},n;\downarrow}, \tilde{\phi}\right] = j^{\dagger}_{-\mathbf{k},n;\uparrow} \tag{A.49}$$

$$\left[j^{\dagger}_{-\mathbf{k},n;\uparrow}, \tilde{\phi}\right] = 0. \tag{A.50}$$

Apply $b_{-\mathbf{k},n;\downarrow}$ to each term in the sum of Eq. A.37 and I can get

$$b_{-\mathbf{k},n;\downarrow}\tilde{\phi}\left|0\right\rangle = j^{\dagger}_{-\mathbf{k},n;\uparrow}\left|0\right\rangle \tag{A.51}$$

$$b_{-\mathbf{k},n;\downarrow}\tilde{\phi}^{2}\left|0\right\rangle = 2j^{\dagger}_{-\mathbf{k},n;\uparrow}\tilde{\phi}\left|0\right\rangle \tag{A.52}$$

$$\vdots \tag{A.53}$$

$$b_{-\mathbf{k},n;\downarrow}\tilde{\phi}^{n}\left|0\right\rangle = nj^{\dagger}_{-\mathbf{k},n;\uparrow}\tilde{\phi}^{n-1}\left|0\right\rangle, \tag{A.54}$$

or equivalently

$$b_{-\mathbf{k},n;\downarrow}\left|\psi^{trial}\right\rangle = j^{\dagger}_{-\mathbf{k},n;\uparrow}\left|\psi^{trial}\right\rangle. \tag{A.55}$$

The condition $z_{t}\left(\mathbf{k}\right)\left|\psi^{trial}\right\rangle = 0, t = m, m+1, ...2m-1$ can then be written as

$$z_{t=m,...,2m-1}\left(-\mathbf{k}\right)\left|\psi^{trial}\right\rangle = \sum_{n=0}^{m-1}\left(\hat{w}_{n,t-m}b^{\dagger}_{n;\uparrow}\left(\mathbf{k}\right)\left|\psi^{trial}\right\rangle + \hat{\varkappa}_{n,t-m}b_{n;\downarrow}\left(-\mathbf{k}\right)\left|\psi^{trial}\right\rangle\right) \tag{A.56}$$

$$= 0 \tag{A.57}$$

and it results in

$$\sum_{n=0}^{m-1}\hat{w}_{n,t-m}b^{\dagger}_{\mathbf{k},n;\uparrow}\left|\psi^{trial}\right\rangle + \sum_{n=0}^{m-1}\hat{\varkappa}_{n,t-m}j^{\dagger}_{-\mathbf{k},n;\uparrow}\left|\psi^{trial}\right\rangle = 0, \tag{A.58}$$

or

$$\sum_{n=0}^{m-1}\left(\hat{w}_{n,t-m} - \sum_{n'=0}^{m-1}\hat{\varkappa}_{n',t-m}h_{n,n'}\left(\mathbf{k}\right)\right)b^{\dagger}_{\mathbf{k},n,\uparrow}\left|\psi^{trial}\right\rangle = 0. \tag{A.59}$$

This gives

$$\hat{w}_{n,t-m} = \sum_{n'=0}^{m-1}\hat{\varkappa}_{n',t-m}h_{n,n'}\left(\mathbf{k}\right), \tag{A.60}$$

or in matrix notation

$$\varrho = \hat{w}\cdot\hat{\varkappa}^{-1} \tag{A.61}$$

To have an existing pairing between two electrons, it is required that Eq. A.47 equals Eq. A.61, or

$$\hat{v}\cdot\hat{\varkappa} = \hat{u}\cdot\hat{w}. \tag{A.62}$$

This is numerically verified to be the case on the SS lattice.

Discussion

- $\hat{w} \cdot \hat{\varkappa}^{-1}$ type structure of the pairing amplitude ϱ removes freedom coming from the choices of the unitary transformation to diagonalize H_k. This feature is conceptually very important since physics should not depend on specific unitary transformation involved in the calculation.

- Singlet pairing nature requires

$$h_{n_1,n_2}(\mathbf{k}) = h_{n_2,n_1}(-\mathbf{k}) \tag{A.63}$$

  from the fact that spacial wavefunction of a singlet should be even by exchanging two electrons. This should be automatically satisfied since the decoupling of the interacting Hamiltonian is done in the singlet channel.

- By setting $\Delta \to 0$, $h_{n_1,n_2}(\mathbf{k})$ reaches the correct limit of infinity when both $(n_1, \mathbf{k})$ and $(n_2, \mathbf{k})$ are occupied and 0 when either of them are left empty.

- In case of single band pairing, $T(\mathbf{k})$ and $D(\mathbf{k})$ are now scalars such that H^{mf} can be simply written as

$$H^{mf}(\mathbf{k}) = \begin{pmatrix} \epsilon(\mathbf{k}) & \Delta(\mathbf{k}) \\ \Delta^*(\mathbf{k}) & -\epsilon(\mathbf{k}) \end{pmatrix}. \tag{A.64}$$

  This is exactly the mean field Hamiltonian used to treat single band BCS theory. This implies the current multiband BCS wavefunction is able to reach the correct single band limit.

APPENDIX B. Real space projection of the multiband BCS wavefunction

The real space projection of the multiband BCS wavefunction is useful in applying Monte Carlo method to evaluate different physical observables. Meanwhile it also enables the extraction of the spacial pairing wavefunction between two electrons of opposite spins and momenta. However, the calculation is tedious and cumbersome, and is complicated by the involvement of big unit cells. Thus it is better to first fully analyze the procedure on the single band BCS wavefunction to gain necessary insights. It is realized that two crucial conditions are needed in expressing the real space projection as a single Slater determinant. When the real space projection is applied to the multiband BCS wavefunction, it is found that the steps from the single band case can be closely mapped here and the corresponding two conditions are also satisfied. This proves that the real space projection on the multiband BCS wavefunction is also a Slater determinant and the spacial pairing wavefunction between electrons easily follows up. Here is the detailed account of the analysis.

Implication from canonically projected single band BCS wavefunction The single band BCS wavefunction takes the form of

$$\left|\Phi_{BCS}^{S}\right\rangle \propto \prod_{\mathbf{k}} \left(1 + h_{\mathbf{k}} c_{\mathbf{k};\uparrow}^{\dagger} c_{-\mathbf{k};\downarrow}^{\dagger}\right) |0\rangle \,. \tag{B.1}$$

The basis for $2N$ particle projection with equal number of spin up and down is written as

$$|\mathbf{r}_1, \uparrow; \mathbf{r}_2, \uparrow; ...; \mathbf{r}_{2N}, \downarrow\rangle = \prod_i c_{\mathbf{r}_i,\uparrow}^{\dagger} c_{\mathbf{r}_{N+i},\downarrow}^{\dagger} |0\rangle \,, \tag{B.2}$$

or in momentum space

$$|\mathbf{r}_1, \uparrow; \mathbf{r}_2, \uparrow; ...; \mathbf{r}_{2N}, \downarrow\rangle \propto \sum_{\mathbf{q}_1, \mathbf{q}_2, ... \mathbf{q}_{2N}} e^{i \sum_{j=1}^{2N} \mathbf{q}_j \cdot \mathbf{r}_j} c_{\mathbf{q}_1,\uparrow}^{\dagger} c_{\mathbf{q}_2,\uparrow}^{\dagger} ... c_{\mathbf{q}_{2N},\downarrow}^{\dagger} |0\rangle \tag{B.3}$$

with the Fourier transformation defined as

$$c_{\mathbf{r}_i;\sigma} = \frac{1}{\sqrt{N}} \sum_{\mathbf{k}} c_{\mathbf{k};\sigma} e^{-i\mathbf{k}\cdot\mathbf{r}_i}. \tag{B.4}$$

Thus the $2N$ particle projection onto the single band BCS wavefunction gives

$$\begin{aligned}
&\left\langle \mathbf{r}_1, \uparrow; ...; \mathbf{r}_{2N}, \downarrow \right| \left. \Phi^S_{BCS} \right\rangle \\
&\propto \sum_{\{\mathcal{K}^N\}} \left(\prod_{\mathbf{k}\in\mathcal{K}^N} h_{\mathbf{k}} \right) \sum_{\mathbf{q}_1,\mathbf{q}_2,...\mathbf{q}_{2N}} e^{i\sum_{j=1}^{2N} \mathbf{q}_j\cdot\mathbf{r}_j} \left\langle 0 \right| c_{\mathbf{q}_1,\uparrow} c_{\mathbf{q}_2,\uparrow} ... c_{\mathbf{q}_{2N},\downarrow} \left(\prod_{\mathbf{k}\in\mathcal{K}^N} c^\dagger_{\mathbf{k},\uparrow} c^\dagger_{-\mathbf{k},\downarrow} \right) \left| 0 \right\rangle
\end{aligned} \tag{B.5}$$

where $\mathcal{K}^N$ denotes a set having in it N unrepeated momenta from the 1st Brillioun Zone, and $\left\{\mathcal{K}^N\right\}$ denotes the collection of all possible $\mathcal{K}^N$ sets.

By considering that

$$\begin{aligned}
&\sum_{\mathbf{q}_1,\mathbf{q}_2,...\mathbf{q}_N} e^{i\sum_{j=1}^{N} \mathbf{q}_j\cdot\mathbf{r}_j} \left\langle 0 \right| \prod_{\mathbf{q}_i} c_{\mathbf{q}_i,\uparrow} \left(\prod_{\{\mathbf{k}_1,\mathbf{k}_2,...\mathbf{k}_N\}} c^\dagger_{\mathbf{k},\uparrow} \right) \left| 0 \right\rangle \\
&= -\sum_{P_{\{\mathbf{k}_i\}}} (-1)^{P(\{\mathbf{k}_i\})} e^{i\left(\mathbf{k}_{P_1}\cdot\mathbf{r}_1 + \mathbf{k}_{P_2}\cdot\mathbf{r}_2 + ... + \mathbf{k}_{P_N}\cdot\mathbf{r}_N\right)} \qquad \text{(B.6)} \\
&= -\begin{vmatrix}
e^{i\mathbf{k}_1\cdot\mathbf{r}_1} & e^{i\mathbf{k}_2\cdot\mathbf{r}_1} & & \\
e^{i\mathbf{k}_1\cdot\mathbf{r}_2} & e^{i\mathbf{k}_2\cdot\mathbf{r}_2} & & \\
 & & ... & \\
 & & & e^{i\mathbf{k}_N\cdot\mathbf{r}_N}
\end{vmatrix} \qquad \text{(B.7)}
\end{aligned}$$

where $P(\{\mathbf{k}_i\})$ denotes a permutation for N momenta, I can get

$$\begin{aligned}
&\left\langle \mathbf{r}_1,\uparrow;...;\mathbf{r}_{2N},\downarrow|\Phi^S_{BCS}\right\rangle_{\text{calc}} \\
&\propto \sum_{\{\mathcal{K}^N\}}\left(\prod_{\mathbf{k}\in\mathcal{K}^N} h_{\mathbf{k}}\right)\underbrace{\left(\sum_{\mathbf{q}_1,...\mathbf{q}_N} e^{i\sum_\tau \mathbf{q}_\tau\cdot\mathbf{r}_\tau}\left\langle 0\right|\prod_{\mathbf{q}_i} c_{\mathbf{q}_i,\uparrow}\prod_{\mathbf{k}\in\mathcal{K}^N} c^\dagger_{\mathbf{k},\uparrow}\left|0\right\rangle\right)}_{\text{spin up}}\times \\
&\underbrace{\left(\sum_{\mathbf{q}_{N+1},...\mathbf{q}_{2N}} e^{i\sum_\tau \mathbf{q}_\tau\cdot\mathbf{r}_\tau}\left\langle 0\right|\prod_{\mathbf{q}_i} c_{\mathbf{q}_i,\downarrow}\prod_{\mathbf{k}\in\mathcal{K}^N} c^\dagger_{-\mathbf{k},\downarrow}\left|0\right\rangle\right)}_{\text{spin down}} \qquad \text{(B.8)}
\end{aligned}$$

$$\begin{aligned}
&\propto \sum_{\{\mathcal{K}^N\}}\left(\prod_{\mathbf{k}\in\mathcal{K}^N} h_{\mathbf{k}}\right)\times \\
&\begin{vmatrix} e^{i\mathbf{k}_1\cdot\mathbf{r}_1} & e^{i\mathbf{k}_2\cdot\mathbf{r}_1} & & \\ e^{i\mathbf{k}_1\cdot\mathbf{r}_2} & e^{i\mathbf{k}_2\cdot\mathbf{r}_2} & & \\ & & ... & \\ & & & e^{i\mathbf{k}_N\cdot\mathbf{r}_N}\end{vmatrix}\begin{vmatrix} e^{-i\mathbf{k}_1\cdot\mathbf{r}_{N+1}} & e^{-i\mathbf{k}_1\cdot\mathbf{r}_{N+2}} & & \\ e^{-i\mathbf{k}_2\cdot\mathbf{r}_{N+1}} & e^{-i\mathbf{k}_2\cdot\mathbf{r}_{N+2}} & & \\ & & ... & \\ & & & e^{-i\mathbf{k}_N\cdot\mathbf{r}_{2N}}\end{vmatrix} \qquad \text{(B.9)}
\end{aligned}$$

$$= \sum_{\{\mathcal{K}^N\}}\begin{vmatrix} \tilde\varphi(\mathbf{r}_1-\mathbf{r}_{N+1}) & \tilde\varphi(\mathbf{r}_1-\mathbf{r}_{N+2}) & & \\ \tilde\varphi(\mathbf{r}_2-\mathbf{r}_{N+1}) & \tilde\varphi(\mathbf{r}_2-\mathbf{r}_{N+2}) & & \\ & & ... & \\ & & & \tilde\varphi(\mathbf{r}_N-\mathbf{r}_{2N})\end{vmatrix} \qquad \text{(B.10)}$$

$$= \sum_{\{\mathcal{K}^N\}}\sum_P (-1)^{P(1,2,...N)}\prod_{j=1}^N \tilde\varphi\left(\mathbf{r}_{P_j}-\mathbf{r}_{N+j}\right) \qquad \text{(B.11)}$$

Here $\tilde\varphi(\mathbf{r}_i-\mathbf{r}_j)$ is a shortcut for the expression

$$\tilde\varphi(\mathbf{r}_i-\mathbf{r}_j) = \sum_{\mathbf{k}\in\mathcal{K}^N} h_{\mathbf{k}} e^{i\mathbf{k}\cdot(\mathbf{r}_i-\mathbf{r}_j)} \qquad \text{(B.12)}$$

On the other hand, I know the expected form for the spacial projection of the BCS wave-function from (99)

$$\left\langle \mathbf{r}_1,\uparrow;...;\mathbf{r}_{2N},\downarrow|\Phi_{BCS}\right\rangle_{\text{ideal}} \propto \begin{vmatrix} \varphi(\mathbf{r}_1-\mathbf{r}_{N+1}) & \varphi(\mathbf{r}_1-\mathbf{r}_{N+2}) & & \\ \varphi(\mathbf{r}_2-\mathbf{r}_{N+1}) & \varphi(\mathbf{r}_2-\mathbf{r}_{N+2}) & & \\ & & ... & \\ & & & \varphi(\mathbf{r}_N-\mathbf{r}_{2N})\end{vmatrix} \qquad \text{(B.13)}$$

Here $\varphi(\mathbf{r}_i - \mathbf{r}_j)$ is a shortcut for the expression

$$\varphi(\mathbf{r}_i - \mathbf{r}_j) = \sum_{\mathbf{k}\in\mathcal{K}} h_{\mathbf{k}} e^{i\mathbf{k}\cdot(\mathbf{r}_i - \mathbf{r}_j)} \tag{B.14}$$

with $\mathcal{K}$ denoting all momenta in 1st Brillioun Zone. Obviously it is expected that

$$\langle \mathbf{r}_1, \uparrow; ...; \mathbf{r}_{2N}, \downarrow | \Phi_{BCS} \rangle_{\text{calc}} = \langle \mathbf{r}_1, \uparrow; ...; \mathbf{r}_{2N}, \downarrow | \Phi_{BCS} \rangle_{\text{ideal}} . \tag{B.15}$$

However, the comparison between Eq. B.10 and Eq. B.13 shows that the major differences between both sides of Eq. B.15 are the lack of summation over $\left\{\mathcal{K}^N\right\}$ and the elements in the matrix expression of two determinants. There must be something special which absorb the big summation over $\left\{\mathcal{K}^N\right\}$ in the left-hand side of Eq. B.15 to give the correct matrix element on the right-hand side. I would start the analysis from the right-hand side of the equation in order to find it out. To simplify notation, $a_{i,j}(\mathbf{k})$ is used to stand for $h_{\mathbf{k}} e^{i\mathbf{k}\cdot(\mathbf{r}_i - \mathbf{r}_j)}$ and thus $\varphi(\mathbf{r}_i - \mathbf{r}_j) = \sum_{\mathbf{k}\in\mathcal{K}} a_{i,j}(\mathbf{k})$.

The right hand side of the equation can be expanded as

$$\begin{aligned}
&\langle \mathbf{r}_1, \uparrow; ...; \mathbf{r}_{2N}, \downarrow | \Phi_{BCS} \rangle_{\text{ideal}} \\
&\propto \sum_P (-1)^{P(1,2,...N)} \prod_{i=1}^{N} \left(\sum_{\mathbf{k}\in\mathcal{K}} a_{\mathbf{r}_{P_i}, \mathbf{r}_{N+i}}(\mathbf{k}) \right) && \text{(B.16)} \\
&= \sum_P (-1)^{P(1,2,...N)} \sum_{\{\mathcal{K}^{N*}\}} \left(\sum_{O\mathcal{K}^{N*}} \prod_{j=1}^{N} a_{\mathbf{r}_{P_j}, \mathbf{r}_{N+j}} \left(\mathbf{k}_{O\mathcal{K}_j^{N*}} \right) \right) && \text{(B.17)} \\
&= \sum_{\{\mathcal{K}^{N*}\}} \sum_{O\mathcal{K}^{N*}} \left(\sum_P (-1)^{P(1,2,...N)} \prod_{j=1}^{N} a_{\mathbf{r}_{P_j}, \mathbf{r}_{N+j}} \left(\mathbf{k}_{O\mathcal{K}_j^{N*}} \right) \right) && \text{(B.18)} \\
&= \sum_{\{\mathcal{K}^{N*}\}} \sum_{O\mathcal{K}^{N*}} \begin{vmatrix} a_{\mathbf{r}_1, \mathbf{r}_{N+1}} \left(\mathbf{k}_{O\mathcal{K}_1^{N*}} \right) & a_{\mathbf{r}_1, \mathbf{r}_{N+2}} \left(\mathbf{k}_{O\mathcal{K}_2^{N*}} \right) & & \\ a_{\mathbf{r}_2, \mathbf{r}_{N+1}} \left(\mathbf{k}_{O\mathcal{K}_1^{N*}} \right) & a_{\mathbf{r}_2, \mathbf{r}_{N+2}} \left(\mathbf{k}_{O\mathcal{K}_2^{N*}} \right) & & \\ & & ... & \\ & & & a_{\mathbf{r}_N, \mathbf{r}_{2N}} \left(\mathbf{k}_{O\mathcal{K}_N^{N*}} \right) \end{vmatrix} && \text{(B.19)}
\end{aligned}$$

where $P(1,2,...)$ denotes permutation over $\{1,2,3,...\}$, $\mathcal{K}^{N*}$ denotes momentum set containing N repeatable momenta from the 1st Brillioun Zone, $O\mathcal{K}^{N*}$ is any ordered version to $\mathcal{K}^{N*}$ and $O\mathcal{K}_i^{N*}$ denotes the ith element in $O\mathcal{K}^{N*}$. Now let us notice that $a_{i,j}(\mathbf{k})$ is decomposable which

means

$$a_{i,j}\left(\mathbf{k}\right)=f_{i}\left(\mathbf{k}\right)g_{j}\left(\mathbf{k}\right) \tag{B.20}$$

with

$$f_{i}\left(\mathbf{k}\right)=h_{\mathbf{k}}e^{i\mathbf{k}\cdot\mathbf{r}_{i}} \tag{B.21}$$

$$g_{j}\left(\mathbf{k}\right)=e^{-i\mathbf{k}\cdot\mathbf{r}_{j}}. \tag{B.22}$$

This kills all the terms in Eq. B.19 with repeated momenta in $O\mathcal{K}^{N*}$, and the big sum over $\mathcal{K}^{N*}$ is reduced to contain collections of momenta without replacement $,\mathcal{K}^{N}$. Now the final expression to the ideal expression can be written as

$$\begin{aligned}
\left\langle \mathbf{r}_{1},\uparrow;...;\mathbf{r}_{2N},\downarrow\left|\Phi_{BCS}\right.\right\rangle _{\text{ideal}} &= \sum_{\{\mathcal{K}^{N}\}}\sum_{O\mathcal{K}^{N}}\left(\sum_{P}\left(-1\right)^{P(1,2,...N)}\prod_{j=1}^{N}a_{\mathbf{r}_{P_{j}},\mathbf{r}_{N+j}}\left(\mathbf{k}_{O\mathcal{K}_{j}^{N}}\right)\right) && \text{(B.23)}\\
&= \sum_{\{\mathcal{K}^{N}\}}\left[\sum_{P}\left(-1\right)^{P(1,2,...N)}\sum_{O\mathcal{K}^{N}}\left(\prod_{j=1}^{N}a_{\mathbf{r}_{P_{j}},\mathbf{r}_{N+j}}\left(\mathbf{k}_{O\mathcal{K}_{j}^{N}}\right)\right)\right] && \text{(B.24)}\\
&= \sum_{\{\mathcal{K}^{N}\}}\sum_{P}\left(-1\right)^{P(1,2,...N)}\prod_{j=1}^{N}\left(\sum_{\mathbf{k}\in\mathcal{K}^{N}}a_{\mathbf{r}_{P_{j}},\mathbf{r}_{N+j}}\left(\mathbf{k}\right)\right) && \text{(B.25)}\\
&\propto \left\langle \mathbf{r}_{1},\uparrow;\mathbf{r}_{2},\uparrow;...;\mathbf{r}_{2N},\downarrow\left|\Phi_{BCS}\right.\right\rangle _{\text{calc}},
\end{aligned}$$

To reach the last step, null terms are inserted to make up for the full factorization.

From the above analysis, it is worth noticing that the ability for a fermionic projection on the BCS wavefunction to result in a single determinant form is due to two things: the condition that $a_{i,j}\left(\mathbf{k}\right)$ is factorizable in the indices of two sites, and the fact that a determinant would vanish if two columns are the same.

Determinant form for real space projected multiband BCS wavefunction By introducing a combo momentum

$$\mathbf{k}|n=\left(\mathbf{k},n\right);-\mathbf{k}|n=\left(-\mathbf{k},n\right)$$

and a combo location

$$\mathbf{R}|r=\left(\mathbf{R},r\right),$$

the multiband BCS wavefunction can be rewritten as

$$\left|\psi^{trial}\right\rangle \propto \prod_{(\mathbf{k}|n,\mathbf{k}'|n')} \left(1 + h_{(\mathbf{k}|n,\mathbf{k}'|n\prime)} b^{+}_{\mathbf{k}|n,\uparrow} b^{+}_{\mathbf{k}'|n\prime,\downarrow} \delta_{\mathbf{k},-\mathbf{k}'}\right) |0\rangle \tag{B.26}$$

where opposite momenta are reinforced by $\delta_{\mathbf{k},-\mathbf{k}'}$. The generalized Fourier transformation can also be written as

$$c_{\mathbf{R}|r,\sigma} = \frac{1}{\sqrt{L}} \sum_{\mathbf{q}|v} \Omega_{\mathbf{R}|r}\left(\mathbf{q}|v\right) b_{\mathbf{q}|v,\sigma} \tag{B.27}$$

with

$$\Omega_{\mathbf{R}|r}\left(\mathbf{q}|v\right) = e^{-i\mathbf{q}\cdot\mathbf{R}} w_{r,v}\left(\mathbf{q}\right). \tag{B.28}$$

The notations are standard: n, v denotes band index, $\mathbf{k}, \mathbf{q}$ denotes momentum in the 1st Brillioun Zone, r denotes the specific site in a unit cell, $\mathbf{R}$ denotes the position of the given unit cell and L denotes total number of unit cells on the lattice.

The $2N$ particle projection of multiband BCS wavefunction can be written as the following,

$$\begin{aligned}
&\left\langle \mathbf{R}_1|r_1,\uparrow;...;\mathbf{R}_N|r_N,\uparrow;\mathbf{R}_{N+1}|r_{N+1},\downarrow;...;\mathbf{R}_{2N}|r_{2N},\downarrow \left|\psi^{trial}\right\rangle\right\rangle_{\text{calc}} \\
&\propto \sum_{\mathbf{q}_1|v_1,\mathbf{q}_2|v_2,...,\mathbf{q}_{2N}|v_{2N}} \left(\prod_{j=1}^{2N} \Omega_{\mathbf{R}_j|r_j}\left(\mathbf{q}_j|v_j\right)\right) \times \\
&\langle 0| \prod_{j=1}^{N} b_{\mathbf{q}_j|v_j,\uparrow} \prod_{j=N+1}^{2N} b_{\mathbf{q}_j|v_j,\downarrow} \sum_{\{\mathcal{K}\}} \left(\prod_{(\mathbf{k}|n,\mathbf{k}\prime|n\prime)\in\mathcal{K}} h_{(\mathbf{k}|n,\mathbf{k}\prime|n\prime)} b^{+}_{\mathbf{k}|n;\uparrow} b^{+}_{\mathbf{k}\prime|n\prime;\downarrow} \delta_{\mathbf{k},-\mathbf{k}'}\right) |0\rangle \qquad \text{(B.29)} \\
&\propto \sum_{\{\mathcal{K}\}} \left(\prod_{(\mathbf{k}|n,\mathbf{k}\prime|n\prime)\in\mathcal{K}} h_{(\mathbf{k}|n,\mathbf{k}\prime|n\prime)}\right) \left(\prod_{(\mathbf{k}|n,\mathbf{k}\prime|n\prime)\in\mathcal{K}} \delta_{\mathbf{k},-\mathbf{k}'}\right) \times \\
&\quad \left(\sum_{\substack{\mathbf{q}_1|v_1, \\ ..., \\ \mathbf{q}_N|v_N}} \langle 0| \prod_{j=1}^{N} \left(\Omega_{\mathbf{R}_j|r_j}\left(\mathbf{q}_j|v_j\right) b_{\mathbf{q}_j|v_j,\uparrow}\right) \prod_{(\mathbf{k}|n,-)\in\mathcal{K}} b^{+}_{\mathbf{k}|n;\uparrow} |0\rangle\right) \times \\
&\quad \left(\sum_{\substack{\mathbf{q}_{N+1}|v_{N+1}, \\ ..., \\ \mathbf{q}_{2N}|v_{2N}}} \langle 0| \prod_{j=N+1}^{2N} \Omega_{\mathbf{R}_j|r_j}\left(\mathbf{q}_j|v_j\right) b_{\mathbf{q}_j|v_j,\downarrow} \prod_{(-,\mathbf{k}\prime|n\prime)\in\mathcal{K}} b^{+}_{\mathbf{k}\prime|n\prime;\downarrow} |0\rangle\right) \qquad \text{(B.30)}
\end{aligned}$$

where $\mathcal{K}$ denotes a set containing N pairs of $(\mathbf{k}|n, \mathbf{k}'|n')$, and $(\mathbf{k}|n, -)$ denotes that only $\mathbf{k}|n$ is under consideration. Similarly due to the fermionic nature of electrons, the two expectations

over vacuum can be evaluated generically as

$$\sum_{\mathbf{q}_1|v_1,...,\mathbf{q}_N|v_N} \langle 0| \prod_{j=1}^{N} \left(\Omega_{\mathbf{R}_j|r_j} \left(\mathbf{q}_j|v_j \right) b_{\mathbf{q}_j|v_j,\sigma} \right) \prod_{(\mathbf{k}|n,-)\in\mathcal{K}} b^{+}_{\mathbf{k}|n;\sigma} |0\rangle$$

$$\propto \begin{vmatrix} \Omega_{\mathbf{R}_1|r_1} \left(\mathbf{k}_1|n_1 \right) & \Omega_{\mathbf{R}_1|r_1} \left(\mathbf{k}_2|n_2 \right) & & \\ \Omega_{\mathbf{R}_2|r_2} \left(\mathbf{k}_1|n_1 \right) & \Omega_{\mathbf{R}_2|r_2} \left(\mathbf{k}_2|n_2 \right) & & \\ & & ... & \\ & & & \Omega_{\mathbf{R}_N|r_N} \left(\mathbf{k}_N|n_N \right) \end{vmatrix} \tag{B.31}$$

where $\{\mathbf{k}_1, \mathbf{k}_2, ..., \mathbf{k}_N\}$ and $\{n_1, n_2, ..., n_N\}$ are momenta and bands contained in $\{(\mathbf{k}|n,-)\}$. Plug it back to Eq. B.30 and notice that the values of n, n' to specific $(\mathbf{k}, \mathbf{k}')$ in $(\mathbf{k}|n, \mathbf{k}'|n')$ are fixed as soon as $\mathcal{K}$ is chosen, and I can get

$$\left\langle \mathbf{R}_1|r_1,\uparrow;...;\mathbf{R}_N|r_N,\uparrow;\mathbf{R}_{N+1}|r_{N+1},\downarrow;...;\mathbf{R}_{2N}|r_{2N},\downarrow \right| \left. \psi^{trial} \right\rangle_{\text{calc}}$$

$$\propto \sum_{\{\mathcal{K}'\}} \left(\prod_{(\mathbf{k}|n,-\mathbf{k}|n')\in\mathcal{K}'} h_{(\mathbf{k}|n,-\mathbf{k}|n')} \right) \begin{vmatrix} \Omega_{\mathbf{R}_1|r_1} \left(\mathbf{k}_1|n_1 \right) & \Omega_{\mathbf{R}_1|r_1} \left(\mathbf{k}_2|n_2 \right) & & \\ \Omega_{\mathbf{R}_2|r_2} \left(\mathbf{k}_1|n_1 \right) & \Omega_{\mathbf{R}_2|r_2} \left(\mathbf{k}_2|n_2 \right) & & \\ & & ... & \\ & & & \Omega_{\mathbf{R}_N|r_N} \left(\mathbf{k}_N|n_N \right) \end{vmatrix} \times$$

$$\begin{vmatrix} \Omega_{\mathbf{R}_{N+1}|r_{N+1}} \left(-\mathbf{k}_1|n'_1 \right) & \Omega_{\mathbf{R}_{N+1}|r_{N+1}} \left(-\mathbf{k}_2|n'_2 \right) & & \\ \Omega_{\mathbf{R}_{N+2}|r_{N+2}} \left(-\mathbf{k}_1|n'_1 \right) & \Omega_{\mathbf{R}_{N+2}|r_{N+2}} \left(-\mathbf{k}_2|n'_2 \right) & & \\ & & ... & \\ & & & \Omega_{\mathbf{R}_{2N}|r_{2N}} \left(-\mathbf{k}_N|n'_N \right) \end{vmatrix} \tag{B.32}$$

$$= \sum_{\{\mathcal{K}'\}} \begin{vmatrix} \tilde{\varphi}^{r_1}_{r_{N+1}} \left(\mathbf{R}_1 - \mathbf{R}_{N+1} \right) & \tilde{\varphi}^{r_1}_{r_{N+2}} \left(\mathbf{R}_1 - \mathbf{R}_{N+2} \right) & & \\ \tilde{\varphi}^{r_2}_{r_{N+1}} \left(\mathbf{R}_2 - \mathbf{R}_{N+1} \right) & \tilde{\varphi}^{r_2}_{r_{N+1}} \left(\mathbf{R}_2 - \mathbf{R}_{N+2} \right) & & \\ & & ... & \\ & & & \tilde{\varphi}^{r_N}_{r_{2N}} \left(\mathbf{R}_N - \mathbf{R}_{2N} \right) \end{vmatrix} \tag{B.33}$$

where $\mathcal{K}'$ denotes collection of N pairs of $(\mathbf{k}|n, \mathbf{k}'|n')\, \delta_{\mathbf{k},-\mathbf{k}'}$, $\tilde{\varphi}^{r_i}_{r_j} \left(\mathbf{R}_i - \mathbf{R}_j \right)$ is defined as

$$\tilde{\varphi}^{r_i}_{r_j} \left(\mathbf{R}_i - \mathbf{R}_j \right) = \sum_{(\mathbf{k}|n,-\mathbf{k}|n')\in\mathcal{K}'} \Omega_{\mathbf{R}_i|r_i} \left(\mathbf{k}|n \right) h_{(\mathbf{k}|n,-\mathbf{k}|n')} \Omega_{\mathbf{R}_j|r_j} \left(-\mathbf{k}|n' \right).$$

There is one thing I might have to clarify in the above simplification. The delta functions $\prod_{(\mathbf{k}|n,\mathbf{k}'|n')\in\mathcal{K}} \delta_{\mathbf{k},-\mathbf{k}'}$ have been applied to reduce $\mathcal{K}$ to $\mathcal{K}'$. Please keep in mind that these delta

functions applies to all the terms in the expression. It remembers where it comes from and where it acts back.

If I still guess that

$$\begin{aligned}&\left\langle \mathbf{R}_1|r_1,\uparrow;...;\mathbf{R}_N|r_N,\uparrow;\mathbf{R}_{N+1}|r_{N+1},\downarrow;...;\mathbf{R}_{2N}|r_{2N},\downarrow\left|\psi^{trial}\right.\right\rangle_{\text{ideal}}\\ &\propto\begin{vmatrix}\varphi_{r_{N+1}}^{r_1}\left(\mathbf{R}_1-\mathbf{R}_{N+1}\right) & \varphi_{r_{N+2}}^{r_1}\left(\mathbf{R}_1-\mathbf{R}_{N+2}\right) & & \\ \varphi_{r_{N+1}}^{r_2}\left(\mathbf{R}_2-\mathbf{R}_{N+1}\right) & \varphi_{r_{N+1}}^{r_2}\left(\mathbf{R}_2-\mathbf{R}_{N+2}\right) & & \\ & & ... & \\ & & & \varphi_{r_{2N}}^{r_N}\left(\mathbf{R}_N-\mathbf{R}_{2N}\right)\end{vmatrix}\end{aligned} \tag{B.34}$$

with

$$\varphi_{r_j}^{r_i}\left(\mathbf{R}_i-\mathbf{R}_j\right)=\sum_{\mathbf{k},n,n'}\Omega_{\mathbf{R}_i|r_i}\left(\mathbf{k}|n\right)h_{(\mathbf{k}|n,-\mathbf{k}|n\prime)}\Omega_{\mathbf{R}_j|r_j}\left(-\mathbf{k}|n'\right), \tag{B.35}$$

I would like to know whether there is similarly

$$\begin{aligned}&\left\langle \mathbf{R}_1|r_1,\uparrow;...;\mathbf{R}_N|r_N,\uparrow;\mathbf{R}_{N+1}|r_{N+1},\downarrow;...;\mathbf{R}_{2N}|r_{2N},\downarrow\left|\psi^{trial}\right.\right\rangle_{\text{calc}}\\ &=\left\langle \mathbf{R}_1|r_1,\uparrow;...;\mathbf{R}_N|r_N,\uparrow;\mathbf{R}_{N+1}|r_{N+1},\downarrow;...;\mathbf{R}_{2N}|r_{2N},\downarrow\left|\psi^{trial}\right.\right\rangle_{\text{ideal}}.\end{aligned} \tag{B.36}$$

To answer this question, I actually don't need to go through the similar calculation done for the single band case. Let us recall in the single band case how the two expressions in Eq. B.15 finally equal each other. It requires that $a_{i,j}\left(\mathbf{k}\right)$ can be decomposed in coordinates i and j so that

$$\begin{vmatrix}a_{r_1,r_{N+1}}\left(\mathbf{k}_1\right) & a_{r_1,r_{N+2}}\left(\mathbf{k}_2\right) & & \\ a_{r_2,r_{N+1}}\left(\mathbf{k}_1\right) & a_{r_2,r_{N+2}}\left(\mathbf{k}_2\right) & & \\ & & ... & \\ & & & a_{r_N,r_{2N}}\left(\mathbf{k}_N\right)\end{vmatrix}\overset{\mathbf{k}_1=\mathbf{k}_2}{=}0, \tag{B.37}$$

this then gives freedom in adding necessary determinants composed by $a_{i,j}\left(\mathbf{k}\right)$ to make up for a complete factorization. In the multiband case, the situation is very similar to that of the single band case. The only difference is that now $(\mathbf{k}|n,-\mathbf{k}|n')$ in the multiband case takes the place of $(\mathbf{k},-\mathbf{k})$ in the single band case. By defining

$$a_{i,j}\left(\mathbf{k}|n,n'\right)=h_{(\mathbf{k}|n,-\mathbf{k}|n\prime)}\Omega_{\mathbf{R}_i|r_i}\left(\mathbf{k}|n\right)\Omega_{\mathbf{R}_j|r_j}\left(-\mathbf{k}|n'\right), \tag{B.38}$$

I similarly have

$$\begin{vmatrix} a_{1,N+1}\left(\mathbf{k}_1|n_1,n_1'\right) & a_{1,N+2}\left(\mathbf{k}_2|n_2,n_2'\right) & & \\ a_{2,N+1}\left(\mathbf{k}_1|n_1,n_1'\right) & a_{2,N+2}\left(\mathbf{k}_2|n_2,n_2'\right) & & \\ & & \ldots & \\ & & & a_{N,2N}\left(\mathbf{k}_N|n_N,n_N'\right) \end{vmatrix} \overset{(\mathbf{k}_1,n_1)=(\mathbf{k}_2,n_2)}{=} 0 \tag{B.39}$$

and this would help to construct a complete factorization in the multiband case as is in the single band case. Thus Eq. B.36 holds.

The expression given for $\varphi_{r_j}^{r_i}\left(\mathbf{R}_i-\mathbf{R}_j\right)$ is identified to be the real space pairing wavefunction for two electrons of opposite spins and can be written as

$$\begin{aligned} \varphi_{r_j}^{r_i}\left(\mathbf{R}_i-\mathbf{R}_j\right) &= \sum_{\mathbf{k},n,n'} \Omega_{\mathbf{R}_i|r_i}\left(\mathbf{k}|n\right) h_{(\mathbf{k}|n,-\mathbf{k}|n\prime)} \Omega_{\mathbf{R}_j|r_j}\left(-\mathbf{k}|n'\right) \\ &= \sum_{\mathbf{k},n,n'} h_{n,n'}\left(\mathbf{k}\right) e^{-i\mathbf{k}\cdot\left(\mathbf{R}_i-\mathbf{R}_j\right)} w_{r_i,n}\left(\mathbf{k}\right) w_{r_j,n'}\left(-\mathbf{k}\right), \end{aligned} \tag{B.40}$$

or in matrix notation,

$$\varphi\left(\mathbf{R}_i-\mathbf{R}_j\right) = \sum_{\mathbf{k}} W\left(\mathbf{k}\right) \varrho\left(\mathbf{k}\right) W^T\left(-\mathbf{k}\right) e^{-i\mathbf{k}\cdot\left(\mathbf{R}_i-\mathbf{R}_j\right)} \tag{B.41}$$

where $W\left(\mathbf{k}\right)$ diagonalizes the kinetic matrix $T\left(\mathbf{k}\right)$, and $\varrho\left(\mathbf{k}\right)=\hat{u}^{-1}\cdot\hat{v}$ is the pairing amplitude in band$\oplus$momentum representation.

Discussion

- The expression of $\varphi\left(\mathbf{R}_i-\mathbf{R}_j\right)$ can be further simplified to be

$$\varphi\left(\mathbf{R}_i-\mathbf{R}_j\right) = \sum_{\mathbf{k}} \varrho^0\left(\mathbf{k}\right) e^{-i\mathbf{k}\cdot\left(\mathbf{R}_i-\mathbf{R}_j\right)} \tag{B.42}$$

  where $\varrho^0\left(\mathbf{k}\right)$ is now the pairing amplitude in site$\oplus$momentum representation.

- Both $\varrho\left(\mathbf{k}\right)$ and $\varrho^0\left(\mathbf{k}\right)$ are independent of arbitrary phases to the eigenvectors forming the unitary transformation.

- It is now obvious to get the nature of spin pairing by looking into $\varphi_{r_j}^{r_i}(\mathbf{R}_i - \mathbf{R}_j)$. When two electrons are switched location, the pairing wavefunction would then be defined as

$$\varphi_{r_j}^{r_i}(\mathbf{R}_j - \mathbf{R}_i) = \sum_{(r_i, r_j; \mathbf{k})} h_{r_j, r_i}(\mathbf{k})\, e^{-i\mathbf{k}\cdot(\mathbf{R}_j - \mathbf{R}_i)} \tag{B.43}$$

$$= \sum_{(r_i, r_j; \mathbf{k})} h_{r_j, r_i}(-\mathbf{k})\, e^{-i\mathbf{k}\cdot(\mathbf{R}_i - \mathbf{R}_j)} \tag{B.44}$$

We require

$$\varphi_{r_j, r_i}(\mathbf{R}_j - \mathbf{R}_i) = \pm\varphi_{r_i, r_j}(\mathbf{R}_i - \mathbf{R}_j) \tag{B.45}$$

if the pairing is known to have good quantum number in spin angular momentum. This is equivalent to

$$h_{r_j, r_i}(-\mathbf{k}) = \pm h_{r_i, r_j}(\mathbf{k}) \implies \varrho^0(\mathbf{k}) = \pm\left(\varrho^0(-\mathbf{k})\right)^T \tag{B.46}$$

APPENDIX C. An example of a Markov Chain

The concept of the Markov chain is of fundamental importance in generating the required distribution function using Metropolis algorithm. The Markov Chain is a stochastic process and is made up of a sequence of random variables, which can either be numbers or arrays. The basic feature of the Markov Chain is that the appearance of the current random variable depends statistically only on the random variable one time step before; or in another word, the Markov Chain has memorylessness property. The random variable at each time step can be just a random number, or can also be an n-dimensional random vector. Here is an example relevant to the Metropolis algorithm used in this thesis.

The Markov Chain is a collection of k dimensional vectors, illustrated as

$$x_n = (r_1, r_2, ...r_k)\,.$$

Let us suppose the update is done dimension by dimension, and is guided by

$$r_i' = r_i + \epsilon\delta_i \tag{C.1}$$

where $\epsilon \sim Unif\,[-1, 1]$ and δ_i is some fixed step for the ith coordinate. That is to say, the ith dimensional coordinate r_i is updated and results in

$$x_n^i = \left(r_1', r_2', ...r_i', r_{i+1}, r_{i+2}, ...r_k\right) \tag{C.2}$$

and then r_{i+1} is updated resulting in

$$x_n^{i+1} = \left(r_1', r_2', ...r_i', r_{i+1}', r_{i+2}, ...r_k\right), \tag{C.3}$$

etc. When all dimensions are updated, one get

$$x_{n+1} = \left(r_1', r_2', ...r_i', r_{i+1}', r_{i+2}', ...r_k'\right). \tag{C.4}$$

Then the Markov Chain is obtained by update through all dimensions. To be specific, it is not $x_n, x_n^1, x_n^2, ...x_n^k, x_{n+1}, ...$ that form the Markov Chain, but $x_n, x_{n+1}, ...$ does. The reason is easy since x_n^i and x_n are still correlated for $i > 1$ due to the fact that they must share many similar components in the vector which violates Markov Chain's condition.

APPENDIX D. More on Metropolis-Hastings algorithm

The Metropolis algorithm gives the idea on why a Markov chain is able to generate asymptotically a required distribution, but it doesn't suggest explicitly how to construct the chain for the problem. This is answered by Hastings improvement on the algorithm. The improved algorithm gives alternative transitional probability from the old state to a new one if one has a preference on how to choose it. This would improve greatly the sampling efficiency if one has already had some knowledge about the distribution function, and thus would prefer to choose a new state using that knowledge. Some details are given below.

The Metropolis-Hastings algorithm defines the transitional probability, $W(x_2|x_1)$, as

$$W(x_2|x_1) = \min\left(\frac{p(x_2)\,Q(x_1|x_2)}{p(x_1)\,Q(x_2|x_1)}, 1\right) \tag{D.1}$$

where $p(x)$ is the intended distribution function in the phase space, $Q(x_i|x_j)$ is called a proposal density and is a conditional probability on x_i given x_j. $Q(x_i|x_j)$ is introduced by user and is legitimate to be totally irrelevant to $p(x)$. How the improved algorithm would be contrasted to the original one can be illustrated in several specific ways.

- The original Metropolis algorithm comes from the Metropolis-Hastings algorithm by choosing a symmetric $Q(x_i|x_j)$ such that $Q(x_i|x_j) = Q(x_j|x_i)$. Specifically, it would reduce to the scheme used in this thesis when

$$Q(x_i|x_j) = \begin{cases} 1 & \text{for } |x_i - x_j| < 2A \\ 0 & \text{o.w.} \end{cases} \tag{D.2}$$

  with $A > 0$ as the step size.

- The algorithm would become a self-avoiding one if $\lim_{\delta\to 0} \frac{1}{\delta}\int_{x_1-\delta}^{x_1+\delta} Q(x_2|x_1)\,dx_2 = 0$.

- The algorithm would function most efficiently in generating the distribution function $p(x)$ if $Q(x_i|x_j) = p(x_i)$, which results in $W(x_2|x_1) \equiv 1$. This means that all tentative trials are accepted and the algorithm is the most efficient.

In the last example, the high efficiency is not a surprise because the tentative samples are specifically chosen according to the proposed density $Q(x_i|x_j) = p(x_i)$. It is in this sense that the Metropolis-Hastings algorithm is most easily seen to be an importance sampling scheme.

APPENDIX E. Recursive relationships for two specially related matrices

Usually calculating a determinant of an $N \times N$ matrix requires number of floating point operations of the order of N^3. But it might be reduced to be of the order of N^2 if the matrix differs from a known matrix by a row or a column. This would be a great improvement in the performance if one needs to evaluate a lot of determinants. The reduction will be shown with the real space projected BCS wavefunction where each electron update causes a change of either one row or one column in the matrix used to calculate the determinant.

The real space projected BCS wavefunction can be expressed as a Slater determinant

$$\langle \mathbf{r}_1, ...\mathbf{r}_N; \mathbf{R}_1, ...\mathbf{R}_N | \Psi_{\mathrm{BCS}} \rangle = \det \begin{pmatrix} \phi(\mathbf{r}_1 - \mathbf{R}_1) & \phi(\mathbf{r}_1 - \mathbf{R}_2) & ... & \phi(\mathbf{r}_1 - \mathbf{R}_N) \\ \phi(\mathbf{r}_2 - \mathbf{R}_1) & \phi(\mathbf{r}_2 - \mathbf{R}_2) & & \\ & & ... & \\ & & & \phi(\mathbf{r}_N - \mathbf{R}_N) \end{pmatrix} \tag{E.1}$$

where all the rows correspond to spin down electrons while all the columns correspond to spin up electrons. For convenience, the above matrix is denoted as A, and the inverse can be derived from its accompanying matrix A^*, defined as

$$A^*_{i,j} = (-1)^{i+j} \det \begin{pmatrix} A_{1,1} & ... & A_{1,j-1} & A_{1,j+1} & & \\ & ... & & & & \\ A_{i-1,0} & & A_{i-1,j-1} & & & \\ A_{i+1,0} & & & A_{i+1,j+1} & & \\ & & & & ... & \\ & & & & & A_{N,N} \end{pmatrix}. \tag{E.2}$$

They satisfy the following relationship

$$A^* A^T = \det A \tag{E.3}$$

or equivalently

$$A^* = \left(A^T\right)^{-1} \det A. \tag{E.4}$$

Now let us suppose that the ith spin down electron moves to a new position. Thus the ith column of A is to be replaced by new elements and the new matrix is denoted as B

$$B = \begin{pmatrix} A_{1,1} & ... & A_{1,i-1} & B_{1,i} & A_{1,i+1} & & \\ A_{2,1} & ... & A_{2,i-1} & B_{2,i} & A_{2,i+1} & & \\ & & & & & ... & \\ & & & & & & A_{N,N} \end{pmatrix}. \tag{E.5}$$

From the matrix algebra, the determinant of matrix B can be calculated out in terms of the accompanying matrices of the original matrix A,

$$\det B = \sum_k B_{k,i} A^*_{k,i}. \tag{E.6}$$

By feeding Eq. E.4 here and rearranging the expression, I get the determinant ratio of matrices B and A as

$$\frac{\det B}{\det A} = \sum_k B_{k,i} \left(A^T\right)^{-1}_{k,i}. \tag{E.7}$$

Similarly when the ith spin up electron is updated, the determinant ratio would be

$$\frac{\det B}{\det A} = \sum_k B_{i,k} \left(A^T\right)^{-1}_{i,k}. \tag{E.8}$$

The derivation is not completed yet because $\left(B^T\right)^{-1}$ is not determined based on $\left(A^T\right)^{-1}$. To get the updated matrix inversion of B from A, please notice that B can be written as

$$B = A + C = A\left(I + A^{-1}C\right) \tag{E.9}$$

where the auxiliary matrix C is basically zero except for the ith column

$$C_{mn} = \begin{cases} 0 & \text{if } n \neq i \\ B_{m,i} - A_{m,i} & \text{if } n = i \end{cases}. \tag{E.10}$$

This gives

$$\left(B^T\right)^{-1} = \left(A^T\right)^{-1} \left[\left(I + A^{-1}C\right)^{-1}\right]^T \tag{E.11}$$

and at the same time

$$\det\left(I + A^{-1}C\right) = \frac{\det B}{\det A} \tag{E.12}$$

Usually $\left(I + A^{-1}C\right)^{-1}$ is not easy to evaluate. However this is not the case here because of the specific structure of C. As is proven below, $A^{-1}C$ is also of the same type as C

$$\left(A^{-1}C\right)_{mn} = \sum_k A^{-1}_{mk}C_{kn} = \begin{cases} 0 & \text{if } n \neq i \\ \sum_k A^{-1}_{mk}C_{ki} & \text{if } n = i \end{cases} \tag{E.13}$$

and thus

$$I + A^{-1}C = \begin{pmatrix} 1 & & \sum_k A^{-1}_{1k}C_{ki} & & \\ & 1 & \sum_k A^{-1}_{2k}C_{ki} & & \\ & & \cdots & \cdots & \\ & & & 1 + \sum_k A^{-1}_{ik}C_{ki} & \\ & & & \cdots & \cdots \\ & & & \sum_k A^{-1}_{nk}C_{ki} & 1 \end{pmatrix}, \tag{E.14}$$

which gives

$$\det\left(I + A^{-1}C\right) = 1 + \sum_k A^{-1}_{ik}C_{ki}. \tag{E.15}$$

The matrix inverse of this specific type can be easily calculated

$$\left(I + A^{-1}C\right)^{-1} = \begin{pmatrix} 1 & & -\dfrac{\sum_k A^{-1}_{1k}C_{ki}}{1 + \sum_k A^{-1}_{ik}C_{ki}} & & \\ & 1 & -\dfrac{\sum_k A^{-1}_{2k}C_{ki}}{1 + \sum_k A^{-1}_{ik}C_{ki}} & & \\ & \cdots & \cdots & & \\ & & 1 - \dfrac{\sum_k A^{-1}_{ik}C_{ki}}{1 + \sum_k A^{-1}_{ik}C_{ki}} & & \\ & & \cdots & \cdots & \\ & & -\dfrac{\sum_k A^{-1}_{nk}C_{ki}}{1 + \sum_k A^{-1}_{ik}C_{ki}} & & 1 \end{pmatrix} = I - \frac{A^{-1}C}{1 + \sum_k A^{-1}_{ik}C_{ki}}. \tag{E.16}$$

Feed the above expression into Eq E.11 and one can get

$$\begin{aligned} \left(B^T\right)^{-1}_{m,n} &= \left(A^T\right)^{-1}\left[\left(I + A^{-1}C\right)^{-1}\right]^T \\ &= \left(A^T\right)^{-1}_{mn} - \frac{\delta_{n,i}}{1 + \sum_{k'}\left(A^T\right)^{-1}_{k'i}C_{k'i}} \sum_{k,k^*}\left(A^T\right)^{-1}_{mk}\left(A^T\right)^{-1}_{k^*,k}C_{k^*,i}. \end{aligned} \tag{E.17}$$

This can be further simplified to be

$$\left(B^T\right)^{-1}_{m,n} = \left(A^T\right)^{-1}_{mn} - \delta_{n,i}\frac{\det A}{\det B}\sum_{k,k^*}\left(A^T\right)^{-1}_{mk}\left(A^T\right)^{-1}_{k^*,k}C_{k^*,i} \tag{E.18}$$

by making use of Eq. E.15 and Eq. E.12.

Eq. E.18 and Eq. E.7, E.8 form the set of equations to update $\det(A)$ and $\left(A^T\right)^{-1}$ when only one row or one column is modified in A. This conclusion is used in calculating the transition rate in the Metropolis algorithm used to generate a distribution function in the discrete lattice space, and it is also used in evaluating different physical observables at local positions.

APPENDIX F. Issues in calculating physical observables in the code

Sign change of hopping amplitude, t There are two kinds of boundary conditions used in this research, the periodic and antiperiodic ones defined by whether the single particle creation (annihilation) operator would change sign or not when it is shifted by the whole lattice size. This is best shown by a 1D chain of N sites with both ends connected. Each site is described by $c_{i,\sigma}$ whose Fourier transformation is defined as

$$c_{i,\sigma} = \sum_n c_{\mathbf{k}_n,\sigma} e^{i\mathbf{k}_n \cdot \mathbf{R}_i} \tag{F.1}$$

where

$$k_n = \frac{2n\pi}{N} \Longrightarrow c_{i,\sigma} = c_{i+N,\sigma} \tag{F.2}$$

for periodic boundary condition, and

$$k_n = \frac{(2n+1)\,\pi}{N} \Longrightarrow c_{i,\sigma} = -c_{i+N,\sigma} \tag{F.3}$$

for antiperiodic boundary condition. Here $n = 0, 1, 2, ..., N-1$. The Hamiltonian to describe this system is

$$H = \sum_{i=1}^{N-1} t c^+_{i,\sigma} c_{i+1,\sigma} + t c^+_{N,\sigma} c_{1,\sigma} + h.c. \tag{F.4}$$

with $h.c.$ denoting the Hermitian Conjugate of the previous terms. It is expected that the different choices of boundary conditions would not change the fact that crystal momentum is a good quantum number for this translational invariant system.

By plugging in Eq. F.1 into the Hamiltonian, H can be written in terms of $c_{\mathbf{k},\sigma}$ as

$$H = \sum_{\mathbf{k}} t c^\dagger_{\mathbf{k},\sigma} c_{\mathbf{k},\sigma} e^{i\mathbf{k}} - \sum_{\mathbf{k},\mathbf{k}'} c^\dagger_{\mathbf{k},\sigma} c_{\mathbf{k}',\sigma} e^{-i\mathbf{k}\cdot\mathbf{R}_N} e^{i\mathbf{k}'\cdot\mathbf{R}_1} \left(t e^{i\mathbf{k}'\cdot\mathbf{R}_N} - t_{N1} \right) + h.c. \tag{F.5}$$

where t_{N1} denotes the hopping to go from the Nth site to the $1st$ site. From the above

expression, it is clear that

$$t_{N1} = \begin{cases} t & \text{for periodic boundary condition} \\ -t & \text{for antiperiodic boundary condition} \end{cases} \tag{F.6}$$

in order to let H be diagonal in momentum space.

Choice of boundary conditions Boundary condition poses concerns in the finite size effect in two ways: it defines discrete momenta used in the wavefunction, it also introduces artificial asymmetry between x and y axes which might obscure the actual correlations among variational parameters. Generally speaking, the use of the periodic boundary condition on both axes is preferred because it usually gives lower energy than other options, which, in my point of view, defines a better class of trial wavefunctions. This is illustrated in Fig. F.1 relevant to $SrCu_2\left(BO_3\right)_2$. The energy calculated under distinct boundary conditions on both axes has much higher energy than the case with periodic boundary conditions. As lattice size increases, these two energies become approaching to each other and presumably agree with each other on the infinite lattice. However, how seriously the finite size effect would affect other physical observables is not merely represented by the energy discrepancy.

Negative momentum as a matrix index In defining a multiband BCS wavefunction, $\mathbf{k}$ and $-\mathbf{k}$ are both used in defining the decoupled Hamiltonian H^{mf}. However, $-\mathbf{k}$ is not readily contained in the momentum set defined in Eq. F.2. One can directly insert $-\mathbf{k}$ into where it is needed in H^{mf}, but this is dangerous in practice especially when additional phase factors are introduce into the Fourier transformation. The most reliable way is to map the negative momenta into the valid momentum definition by

$$-ka + 2\pi \in [-\pi, \pi)\,. \tag{F.7}$$

This gives

$$k_{n'} = -\frac{2\left(n-1\right)\pi}{N} + 2\pi = \frac{2\left[N-(n-1)\right]\pi}{N} \tag{F.8}$$

$$\Rightarrow n' = \begin{cases} 1 & \text{for } n = 1 \\ N - n + 2 & \text{for } n = 2, 3, ...N \end{cases} \tag{F.9}$$

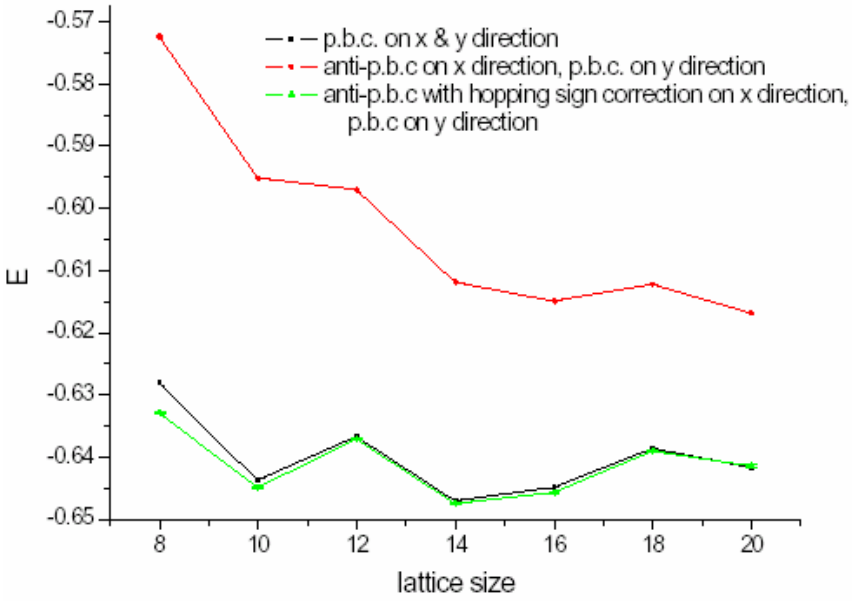

Figure F.1 Energy for different boundary conditions at 10% doping on 8×8 to 20×20 lattice. The evaluation is related to the trial wavefunction for $SrCu_2(BO_3)_2$. Curves with different colors show lattice size dependence of energies under different boundary conditions. What is special about the green curve is the energy involves the hopping amplitude whose sign is taken care of according to the antiperiodic boundary condition on the x axis. The resulting energy curve is then very close to that from periodic boundary condition. The variability in energy in black is due to the finite size effect as well as the failure to have an exact 10% doping on a finite lattice.

for periodic boundary condition, and

$$k_{n'} = -\frac{(2n-1)\,\pi}{N} + 2\pi = \frac{[2\,(N-n+1)-1]\,\pi}{N} \tag{F.10}$$

$$\Rightarrow n' = N - n + 1 \text{ for } n = 1, 2, ...N \tag{F.11}$$

for antiperiodic boundary condition.

APPENDIX G. Issues in automating the minimization procedure

To have a hassle-free simulation, one would hope the code to have intelligence to guide itself throughout the simulation and give out most reliable global minimum. If using a simulated annealing algorithm and a data set with error, several issues need to be taken care of, including, how to control data error at specific virtual temperature; how to adjust the step to each dimension as the Markov chain wanders around the phase space, etc. The solutions are provided here. Before proceding, I just want to remind that the major concept and notations of the annealing algorithm are provided in chapter 2 in the thesis.

How much to reduce $\Delta\bar{E}$, the energy error, to adapt to a given k_T? Obviously $\Delta\bar{E} \gg k_T$ is not allowed. But $\Delta\bar{E} \ll k_T$ would make the algorithm inefficient because $\Delta\bar{E}$ is reduced as square root of number of samples. The most appropriate choice is

$$\frac{\left\langle \Delta\bar{E} \right\rangle}{k_T} \simeq 0.8, \tag{G.1}$$

whose reasoning is given below by checking how the distribution function, $p\left(\vec{u}\right)$, is affected by energy errors. Here and after, $\langle \ldots \rangle$ denotes a statistical average.

The actual distribution function for the energies with error would be

$$p'\left(\vec{u}\right) = C\left(\frac{\Delta\bar{E}}{k_T}\right) e^{-\frac{\bar{E}(\vec{u})+\Delta\bar{E}}{k_T}} \tag{G.2}$$

$$= p\left(u\right) + \gamma\frac{\Delta\bar{E}}{k_T} + O\left(\frac{\Delta\bar{E}}{k_T}\right)^2 \tag{G.3}$$

where γ is the coefficient collected for linear terms in $\Delta\bar{E}$. If the deviation from the true energies is randomly signed and mutually uncorrelated, or

$$\left\langle \Delta\bar{E} \right\rangle = 0, \tag{G.4}$$

then $p'(\vec{u})$ differs from $p(u)$ to the second order in $\frac{\Delta\bar{E}}{k_T}$. Practically, it can be close yet smaller than 1.

How to control $\Delta\bar{E}$, the energy error, during the simulation? The phase space can be totally different at different locations, reflected in totally different energy landscape and different energy error with a fixed number of iterations. It is hoped that energy error is controlled to be homogeneous everywhere. This can be done by adjusting number of iterations, and increasing number of bins if the conjectured number of iterations is still too few. Please remember, the overall energy error satisfies asymptotically

$$\Delta\bar{E} \propto \frac{f(\vec{u})}{\sqrt{N}} \tag{G.5}$$

where N is the totally number of iterations used to obtain the energy estimate and $f(\vec{u})$ explicitly show that the error itself varies in phase space.

How to tolerate failed energy evaluation? It is possible energy evaluation fails. One case is that the chemical potential is set too low so that the system is unable to accommodate as many pre-given electrons. Another instance would be that the samples for a given energy deviate too much from a normal distribution. If this happens, just reject the failed point and try a new one because the Metropolis algorithm tolerates mistakes pretty well.

Optimal steps to be adjusted in situ The scheme to adjust the step to each dimension is presented in chapter 2. The formula is given in Eq. 2.61 and is repeated here

$$\frac{A_{new}}{A} = \frac{g^{-1}(\kappa_f)}{g^{-1}(\kappa_a)} \tag{G.6}$$

where

$$g(A) = \frac{\int_0^A e^{-x^2} dx}{A} = \kappa. \tag{G.7}$$

Here A is the current step size, κ_a is the actual acceptance ratio coming out of the simulation and κ_f is some fixed acceptance ratio expected to be maintained. In this section, only discussions are provided to clarify some details.

The scheme gives identical formulae for different quadratic dispersions and different values of k_T. This is good news for it to be applied everywhere on the variational phase space because details of the local region are usually hard to obtain. The formula is used iteratively during the simulation. The steps would be adjusted consecutively when the Markov chain wanders around the phase space. When the process is confined within any local energy minimum, the convergence to the optimal step size is guaranteed.

One might raise concerns on the validity of applying Eq. G.6. One concern is about the assumption of a quadratic energy dispersion, which is, however, most often not the case. Then this formula can still be interpreted as a fitting scheme by mapping an irregular energy landscape onto a quadratic curve. One might also suppose that the fact the process changes its location all the time is different from what the scheme assumes to calculate the theoretical κ. The idea to treat these two cases equivalent is supported by the success of the scheme in practice. Another concern might come from the fact that the running κ_a is complicated by its statistical uncertainty together with varying step size during the simulation. The answer to it is the consecutive update on the steps to maintain a fixed κ_f. They might be wrong at some instances, but they give reasonable step size in the long run. Another thing worth mentioning is that some negative feedback must be applied to the new step size.

The scheme is derived for one dimensional update. But sometimes two or more dimensions are expected to be updated together. Then it would be a challenge to define κ_a appropriately. Even if this can be done, Eq. G.6 might perform badly in giving a reasonable step size. However, it seems it still works reasonably well when only two dimensions are updated together.

How to avoid getting trapped in a fake energy minimum? Energies come with error, as is inevitable from the Monte Carlo evaluation. It can thus lead to a fake energy minimum which might trap the Markov chain there forever. With the current step update scheme, this can be delt with easily.

As the process has been trapping somewhere, the step sizes are constantly reduced to zero. Thus the Markov chain must move around if it is a true minimum. However, this criterion would be too strong in deciding a fake one since there is no a prior knowledge on how sharp the

local minimum should be. On the other hand, it is perfectly legitimate to stay at the global minimum for limited time and then switch to higher energies as simulation continues. This gives the idea to improve the algorithm by artificially giving finite correction, chosen to be

$$\delta E = \min\left(\Delta\bar{E}, k_T\right), \tag{G.8}$$

to an energy each time the Markov chain repeats itself. The correction is not there if $\Delta\bar{E} = 0$, otherwise, it would facilitate the transition by a maximum factor of e each time the energy is repeated.

Improved scheme to adjust k_T in situ It is crucial to choose an appropriate way to reduce k_T in searching for the global energy minimum with the simulated annealing algorithm. The original scheme is the simple exponential decay (89), where k_T is guided by a constant reduction, or

$$k_T^{(n)} = \alpha^{n-1} k_T, \tag{G.9}$$

disregarding any specific problem. This is obviously not the best scheme because the Markov chain is biased locally by a reduced k_T, besides the natural trend to favor lower energy region. Although it is impossible to propose the correct scheme to adjust k_T, some improvements might still be possible on this problem. Here are some thoughts.

The trapping at lower energy region is related to the fact that it is harder to jump out of the valley as compared to falling into it. This feature is required to generate the distribution $p\left(\vec{u}\right) \propto e^{-E(\vec{u})/k_T}$, but leads to low efficiency in locating the global minimum. A plausible way to makeup for it is to increase k_T as long as a sudden drop in energy is detected. However, the increase in k_T should be cautious since it might prevent the algorithm from getting converged. Similarly, a reduction in k_T might also be required to avoid escaping the local minimum when an increase in energy is detected. This idea is explicitly carried out by answering the following questions,

- How to detect a change in an energy sequence?
- How much to increase (decrease) k_T when a decrease (increase) in energy is detected?

- Can the process converge and give decent results in reasonable sample size?

Due to the statistical nature of the sampled sequence of fixed size, the trend can be answered by looking at its time correlation. Let us suppose the sequence of energy samples to be

$$y_1, y_2, ...y_N$$

where N is the sample size. The time correlation estimator is defined as

$$\rho = \frac{\sum_n (n - \bar{n})(y_n - \bar{y})}{\delta_n \delta_y} \tag{G.10}$$

where $\bar{y} = \frac{1}{N}\sum_i y_i$, $\bar{n} = \frac{N+1}{2}$ and

$$\delta_y = \sqrt{\frac{\sum_i (y_i - \bar{y})^2}{N-1}}; \delta_n = \sqrt{\frac{\sum_i (n - \bar{n})^2}{N-1}}. \tag{G.11}$$

It is usually assumed that $\{y_i\}$ are independently and identically distributed (iid) and thus $\langle \rho \rangle = 0$. But the distribution function of ρ is still hard to determine and thus a new variable is introduced with a known asymptotic distribution function

$$z = \frac{1}{2}\ln\left(\frac{1+\rho}{1-\rho}\right) \Longrightarrow \left(\sqrt{N-3}\right) z \sim n(0,1). \tag{G.12}$$

Here $n(0,1)$ denotes the standard normal distribution and $\sim$ means "is distributed as". The upper and lower bounds for ρ are defined as

$$\rho_\pm = \pm\frac{e^{2z^0} - 1}{e^{2z^0} + 1} \tag{G.13}$$

beyond which the energy sequence has definite trend. Here $z^0 = 1.96/\sqrt{N-3}$ is the 95% confidence interval for z.

The way to adjust k_T in situ is a generalization of the original scheme where an empirical function W is introduced in place of a fixed ratio in Eq. G.9,

$$k_T^{new} = W(\rho)\, k_T^{old}. \tag{G.14}$$

The functional form for $W(\rho)$ is defined as

$$W(\rho) = \begin{cases} 1 + \alpha_1 (\rho - \rho_-)^2 & \text{for } \rho < \rho_- \\ 1 + \alpha_5 (\rho - \rho_-) & \text{for } |\rho| < \rho_+ \\ \alpha_2 \rho^2 + \alpha_3 \rho + \alpha_4 & \text{for } \rho > \rho_+ \end{cases} \tag{G.15}$$

with the parameters taking expressions, for example, as

$$\alpha_1 = \frac{u_0 - 1}{(1-\rho_+)^2}, \tag{G.16}$$

$$\alpha_2 = \frac{1 - \alpha - \rho_+ (1 - 2v_0 + \alpha)}{2\rho_+ (1-\rho_+)^2}, \tag{G.17}$$

$$\alpha_3 = \frac{\alpha - 1 + (\rho_+)^2 (1 - 4v_0 + 3\delta)}{2\rho_+ (1-\rho_+)^2}, \tag{G.18}$$

$$\alpha_4 = \frac{1 + \alpha - \rho_+ (1 + 3\delta) + 2v_0 (\rho_+)^2}{2(1-\rho_+)^2}, \tag{G.19}$$

$$\alpha_5 = \frac{\alpha - 1}{2\rho_+}. \tag{G.20}$$

Here u_0 defines the maximum increment in k_T and is directly related to v_0 by $u_0 v_0 = 1$. α has the physical meaning of $\alpha = W(\rho^+)$ and plays the role of the fixed ratio in Eq. G.9. The logic behind this complicated $W(\rho)$ is to increase k_T parabolically when significant decrease in energy is detected; to reduce k_T mildly to ensure convergence by following the well-established annealing algorithm when energy change is insignificant; to reduce k_T a bit more when the energy sequence is detected to climb out of the valley.

The generalized annealing scheme defined through Eq. G.15 makes it very easy to control the simulation. The efficiency is mainly controlled by α while the stability by u_0. Although their optimal values cannot be rigorously determined, u_0 might be guided by avoiding too much oscillation in k_T, which is caused by lack of detailed information of the energy valley so that k_T can not be adjusted correctly. The quantitative measure for the oscillation is the energy increment ratio, η, defined to be

$$\eta = \frac{\pi_-}{\pi_+}$$

where π_- (π_+) are called the relative(absolute) energy increment and are defined as

$$\pi_- = \sum_{n=1}^{\infty} \Delta_n (\beta_\pi)^{n-1} \tag{G.21}$$

$$\pi_+ = \sum_{n=1}^{\infty} |\Delta_n| (\beta_\pi)^{n-1} \tag{G.22}$$

with $\Delta_n = y_{n,N} - y_{n,1}$ and $\beta_\pi \in (0,1)$ acting as a soft cutoff. When the energy sequence is monotone, $\pi_- \simeq \pi_+$; while it oscillates or is basically unchanged, $|\pi_-| \ll \pi_+$. Thus by

monitoring η one would have a clear clue on how the energy sequence changes and thus u_0 can be changed accordingly.

BIBLIOGRAPHY

[1] P. A. Lee, N. Nagaosa, X. G. Wen, Rev. Mod. Phys. 78, 17 (2006)

[2] Ross H. McKenzie, Science, 278, 820, (1997)

[3] G. R. Stewart, Rev. Mod. Phys. 56,755 (1984)

[4] Y Shimizu, K Miyagawa, K Kanoda, et al, Phys. Rev. Lett., 91, 107001 (2003)

[5] Neil W. Ashcroft, N. David Mermin, "Solid State Physics" by Brooks Cole in 1976

[6] Patrik Fazekas, "Lecture notes on electron correlation and magnetism" by World Scientific Publishing Co. in 2003

[7] A. C. Hewson, "The Kondo Problem to Heavy Fermions", by Cambridge University Press, 1993

[8] H. K. Onnes, Comm. Phys. Lab. Univ. Leiden, Nos. 122 and 124, 1911

[9] J. Bardeen, L. N. Cooper, and J. R. Schrieffer, Phys. Rev. 108, 1175 (1957)

[10] J. G. Bednorz, and K. A. Muller, Z. Phys. B 64, 189 (1986)

[11] A. Kawamoto, K. Miyagawa, Y. Nakazawa, and K. Kanoda, Phys. Rev. Lett. 74, 3455 (1995)

[12] F. Steglich, J. Aarts, C.D. Bredl, et al, Phys. Rev. Lett. 43, 1892 (1979)

[13] J. Schmalian, M. Langer, S. Grabowski, et al, Phys. Rev. B 54, 4336 (1996)

[14] P.W. Anderson, Science 235, 1196 (1987)

[15] S Liang, B Doucot, PW Anderson, Phys. Rev. Lett. 61, 365, (1988)

[16] S. A. Kivelson, D. S. Rokhsar, and J. P. Sethna, Phys. Rev. B 35, 8865 (1987)

[17] A. Paramekanti, M. Randeria, and N. Trivedi, Phys. Rev. Lett. 87, 217002 (2001); Phys. Rev. B, 70, 054504 (2004)

[18] A Damascelli, Z Hussain, ZX Shen, Rev. Mod. Phys. 75, 473 (2003)

[19] T. Ogawa, K. Kanda and T. Matsubara, Progr. Theor. Phys., 53, 614 (1975)

[20] M. C. Gutzwiller, Phys. Rev. 137, A1726 (1965)

[21] J. Hubbard, Proc. Roy. Soc. (London) A276, 238 (1963); 277, 238 (1964)

[22] J. Kanamori, Progr. Theoret. Phys. (Kyoto) 30, 275 (1963)

[23] A. Fortunelli, A. Painelli, J. Chem. Phys. 106, 8041 (1997); 106, 8051 (1997); Phys. Rev. B. 55, 16088 (1997); G. Freebairn, "Phonons and the Isotopically induced Mott Transition", University of Queensland (2005)

[24] A. P. Balachandran, E. Ercolessi, G. Morandi, et al, "Hubbard Model and Anyon Superconductivity" by World Scientific, 1990

[25] S. Sachdev, "Quantum phase transition", by Cambridge University Press, 1999

[26] P. Coleman, Phys. Rev. B 29, 3035 (1984)

[27] A. Georges, G. Kotliar, W. Krauth et. al. Rev. Mod. Phys. 68, 13 (1996)

[28] Th. Maier, M. Jarrell, Th. Pruschke, et al, Rev. Mod. Phys. 77, 1027 (2005)

[29] J. W. Orland, H. Negele, Quantum many particle system, by Perseus Books, 1988

[30] H. Yokoyama and H. Shiba, J. Phys. Soc. Jpn, 56, 1490 (1987)

[31] Michael Lang, Superconductivity Review, 1996, Vol. 2, pp.1-115

[32] J. Singleton and C. Mielke, Contemp. Phys. 43, 63 (2002)

[33] B. J. Powell and R. H. Mckenzie, J. Phys.: Condens. Matter 18 R827 (2006)

[34] H. Urayama, H. Yamochi, H. Saito, et al, Chem. Lett., 1988, 463 (1988)

[35] J. Singleton, P. A. Goddard, N. Harrison, et al, Phys. Rev. Lett., 88, 037001 (2002)

[36] D. Chasseau, J. Gaultier, M. Rahal, et al, Synth. Met., 41-43, 2039 (1991)

[37] K Miyagawa, A Kawamoto, Y Nakazawa, et al, Phys. Rev. Lett., 75, 1174 (1995)

[38] T. Komatsu, N. Matsukawa, T Inoue, and G. Saito, J. Phys. Soc. Japan 65, 1340 (1996)

[39] J. E. Shirber, E. L. Venturini, A. M. Kini, et al, Physica C 152, 157 (1988)

[40] K. Kornelsen, J. E. Eldridge, C. C. Homes, et al, Solid State Comm., 72, 475 (1989)

[41] K. Kornelsen et al., Solid State Commun. 72, 475 (1989)

[42] T. Arai, K. Ichimura, K. Nomura, et al, Phys. Rev. B, 63, 104518 (2001)

[43] U. Geiser, H. H. Wang, K. D. Carlson, et. al, Inorg. Chem. 30, 2586 (1991)

[44] J Liu, J Schmalian, N Trivedi, Phys. Rev. Lett., 94, 127003 (2005)

[45] Y Kurosaki, Y Shimizu, K Miyagawa, et al, Phys. Rev. Lett., 95, 177001 (2005)

[46] H. Kino and H. Fukuyama, J. Phys. Soc. Jpn. 64, 2726 (1995)

[47] V. P. Antropov, O. Gunnarsson, and O. Jepsen, Phys. Rev. B, 46, 13647 (1992)

[48] Ross H. McKenzie, Comments Cond. Matt. Phys. 18, 309 (1998)

[49] Joeg Schmalian, Phys. Rev. Lett. 81, 4232 (1998)

[50] T Watanabe, H Yokoyama, Y Tanaka, J Inoue, J. Phys. Soc. Jpn. 75, 074707 (2006)

[51] B. Powell and R. McKenzie, Phys. Rev. Letters 94, 047004 (2005)

[52] J.Y. Gan, Y. Chen, Z. B. Su, and F. C. Zhang, Phys. Rev. Lett. 94, 067005 (2005)

[53] B. Kyung, A.M.S. Tremblay, Phys. Rev. Lett. 97, 046402 (2006)

[54] R. W. Smith and D. A. Keszler, J. Solid State Chem. 93, 430 (1991)

[55] H. Kageyama, K. Yoshimura, et al, Phys. Rev. Lett. 82, 3168 (1999)

[56] S. Miyahara and K. Ueda, J. Phys.: Condens. Matter 15 R327 (2003)

[57] H. Kageyama, M. Nishi, et al, Phys. Rev. Lett. 84, 5876 (2000)

[58] K. Onizuka, H. Kageyama, et al, J. Phys. Soc. Japan 69 1016 (2000)

[59] O Cepas, K Kakurai, L P Regnault, et al, Phys. Rev. Lett. 87 167205 (2001)

[60] H. Nojiri, H. Kageyama, K. Onizuka, et. al, J. Phys. Soc. Japan 68 2906 (1999)

[61] B.S. Shastry and B. Kumar, Prog. Theor. Phys. Suppl. 145, 1 (2002)

[62] B S Shastry and B. Sutherland, Physica B 108, 1069 (1981)

[63] P. W. Anderson, Phys. Rev. 102, 1008 (1956)

[64] E. Manousakis, Rev. Mod. Phys., 63, 1, (1991)

[65] S Miyahara and K Ueda, Phys. Rev. Lett. 82 3701 (1999)

[66] C H Chung, J B Marston and S Sachdev, Phys. Rev. B 64 134407 (2001)

[67] C.-H. Chung and Y. B. Kim, Phys. Rev. Lett. 93, 207004 (2004)

[68] P. W. Leung and Y. F. Cheng, Phys. Rev. B 69, 180403 (2004)

[69] S. El Shawish and J. Bonca, Phys. Rev. B 74, 174420 (2006)

[70] G.T. Liu, J.L. Luo, N.L. Wang, et al. Phys. Rev. B 71, 014441 (2005)

[71] Y. Kohsaka, M. Azuma, I. Yamada, et. al, Journ. of the Amer. Chem. Soc. 124, 12275 (2002)

[72] M. C. Gutzwiller, Phys. Rev. 137, A1726 (1965)

[73] T. A. Kaplan, P. Horsch, and P. Fulde, Phys. Rev. Lett. 49, 889 (1982)

[74] H. Morita, S. Watanabe, and M. Imada, J. Phys. Soc. Jpn. 71, 2109 (2002)

[75] H. Suhl, B. T. Matthias and L. R. Walker, Phys. Rev. Lett. 3, 552, (1959)

[76] C.N. Yang, Rev. Mod. Phys. 34, 694 (1962)

[77] H.T.Nieh, G. Su and B.H. Zhao, Phys. Rev. B. 51, 3760 (1995)

[78] P. Jordan, Zeitschrift fur Physk 44, 473 (1927)

[79] L. Collins, An Introduction to Markov Chain Analysis, by Norwich : Geo Abstracts, 1975

[80] http://en.wikipedia.org/wiki/Markov_chain

[81] N. Metropolis, A.W. Rosenbluth, M.N. Rosenbluth, A.H. Teller, and E. Teller. Journal of Chemical Physics, 21(6):1087-1092, 1953

[82] W.K. Hastings., Biometrika, 57(1):97-109, 1970

[83] P. Hellekalek, Math. Comput. Simulat., 46, 485 (1998)

[84] http://www.nrbook.com/a/bookfpdf.php

[85] S. K. Park, K. W. Miller, Communications of the ACM, 31, 1192 (1988)

[86] http://www.nrbook.com/a/bookfpdf/f7-1.pdf

[87] M. Matsumoto & T. Nishimura, ACM Trans. Model. Comput. Simul. 8, 3 (1998)

[88] D. M. Ceperley, G. V. Chester, M. H. Kalos, Phys. Rev. B 16, 3081 (1977)

[89] http://www.nrbook.com/a/bookfpdf/f10-9.pdf

[90] R.B. Laughlin cond-mat/0209269

[91] O. Parcollet, G. Biroli, and G. Kotliar, Phys. Rev. Lett. 92, 226402 (2004)

[92] A. Himeda and M. Ogata, Phys. Rev. Lett. 85, 4345 (2000)

[93] D. J. Scalapino, S. R. White and S. C. Zhang, Phys. Rev. B 47, 7995 (1993)

[94] I. Martin D. Podolsky and S.A. Kivelson, Phys. Rev. B 72, 060502 (2005)

[95] P. W. Anderson, Phys. Rev. 109, 1492, (1958)

[96] Y. Nagaoka, Phys. Rev. 147, 392 (1966)

[97] I. Affleck, Z. Zou, T. Hsu, and P. W. Anderson, Phys. Rev. B, 38, 745 (1988)

[98] G. Kotliar and J. l. Liu, Phys. Rev. B, 38, 5142 (1988)

[99] J. R. Schrieffer, theory of superconductivity, by Westview Press (1999)

[100] S. Sachdev, Phys. Rev. B, 45, 12377 (1992)

[101] K. Kanoda, Physica C, 299, 282 (1997)